11-28-2022

Axisymmetric Soft Elastohydrodynamic Squeeze Films: Parametric Studies

Eli Heisey
exh6661@rit.edu

Axisymmetric Soft Elastohydrodynamic Squeeze Films: Parametric Studies

By

Eli Heisey

A Thesis Submitted in Partial Fulfillment of the Requirements
for the Degree of Master of Science in Mechanical Engineering

Department of Mechanical Engineering
Kate Gleason College of Engineering
Rochester Institute of Technology
November 28, 2022

Approved by

Dr. Stephen Boedo, *Thesis Advisor* Date
Department of Mechanical Engineering

Dr. Hany Ghoneim, *Committee Member* Date
Department of Mechanical Engineering

Dr. Kathleen Lamkin-Kennard, *Committee Member* Date
Department of Mechanical Engineering

Dr. Sarilyn Ivancic, *Department Representative* Date
Department of Mechanical Engineering

Abstract

Theoretical and experimental studies of hydrodynamically lubricated bearings with a soft, compliant surface have shown advantages over conventionally rigid bearings. These bearings operate in the isoviscous, elastohydrodynamic regime of thin film lubrication with low film pressures and relatively large surface deflections. They exhibit less sensitivity to misalignment, particulates in the lubricant, and low levels of lubricant, making them very attractive for bearing designers. However, there is very little published work, either experimental or theoretical, to describe the squeeze-film lubrication behavior of a bearing with a compliant layer. This thesis utilizes a Nodal Inverse Hydrodynamic computation approach to calculate the behavior of a squeeze-film between an axisymmetric rigid indenter with a paraboloid or conical profile and a thin, soft, linearly elastic layer. The computed results are compared with previously published experimental data to validate this approach. Nondimensional design charts are presented to give guidelines for bearing designers.

Table of Contents

List of Tables

List of Figures

Nomenclature

Symbol	Meaning
a	Dry contact radius
b	Elastic layer thickness
d	Relative surface displacement
E	Elastic modulus
e	Deflection of rigid indenter from initial position
F	Normal loading force
h	Film thickness
p	Pressure
R	Indenter radius (Film extent)
α	Load rate parameter
β	Indenter slope
δ	Deflection
ϵ	Nondimensional indenter displacement
κ	Indenter curvature
μ	Viscosity (Absolute)
ν	Poisson ratio
τ	Nondimensional time

Superscript

a	Elastic layer
b	Rigid Indenter

Subscript

1	Nodal partition with specified flow; state variables; interior nodes
2	Nodal partition with specified pressure; non-state variables; exterior nodes

Matrices

A	Area matrix
B	Elastic equilibrium matrix
C	Compliance matrix
G	Static equilibrium matrix
$\widetilde{K}$	Absolute stiffness matrix
K	Relative stiffness matrix
K_h	Squeeze fluidity matrix
K_p	Pressure fluidity matrix

Chapter 1

Introduction

Elastohydrodynamic lubrication (EHL) refers to elastic surfaces that transmit force and motion through a thin fluid film. “Soft” EHL refers to a class of lubrication problems where at least one surface has a relatively low elastic modulus (e.g. polymers). This is in contrast to the more typical “hard” EHL problems, where both surfaces have relatively high elastic moduli (e.g. metal gears or rollers). In a soft EHL problem, the low elastic modulus introduces larger deformations and lower film pressures than would arise in a hard EHL problem [1]. These lower film pressures allow the effects of piezoviscosity to be neglected, and thermal effects on viscosity are less significant than in hard EHL problems.

The motivating soft EHL problem for this thesis work is the axisymmetric normal approach of a rigid spherical indenter onto a thin elastic layer bonded to a rigid surface. Figure 1.1 shows a schematic of the problem with the elastic layer and rigid indenter labeled as “A” and “B” respectively. A thin lubricant film separates the two surfaces, and a normal force is applied to the sphere along the z-axis.

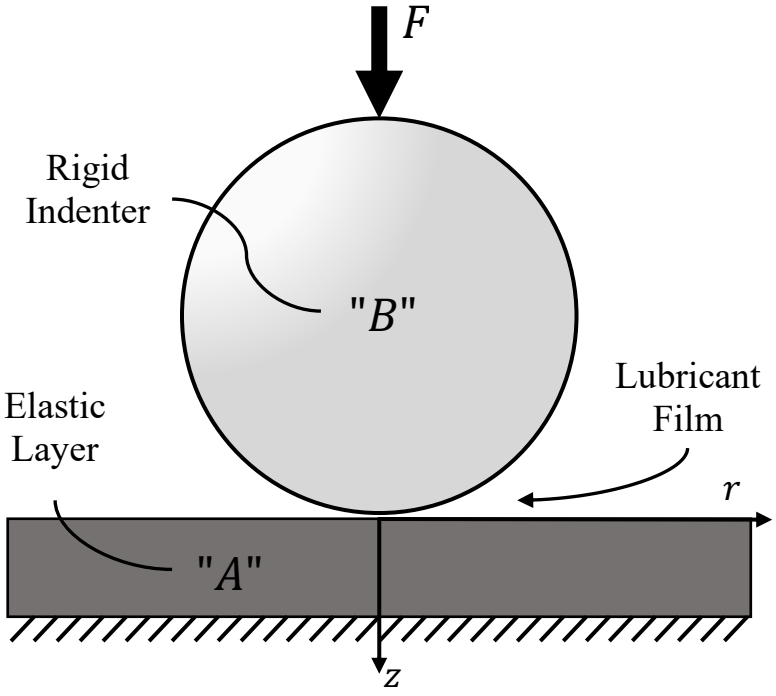

Figure 1.1 Motivating squeeze-film problem schematic

This simple model has been used to understand the complex behavior of animal joints, especially the human hip joint. In 1966, Fein published work suggesting that synovial joints are lubricated by squeeze-film action [2]. This marked the beginning of a series of experimental publications that explored the complicated mechanisms at work in a synovial joint. In a doctoral thesis [3], Norman examined how the film thickness and pressure were affected by an elastic layer, including the permeability of that layer (for so-called "weeping" lubrication) and various additives that influence the viscous properties of the lubricant. This work was done using an experimental apparatus that resembled the schematic shown in Figure 1.1. This experimental work was further expanded upon by Higginson and Norman [4] and Gaman, Higginson, and Norman [5]. In 2009, Mattei et al. reviewed the literature of EHL modeling of artificial hip joints [6]. They noted that for some configurations the "ball-in-socket" geometry of the hip joint could be approximated by an equivalent "ball-on-plane" geometry by use of an effective elastic modulus and effective indenter radius. About one-third of publications listed performed their analyses based on this "ball-on-plane" geometry.

Unrelated to their application to hip joints, bearings with a compliant layer also offer a number of advantages over traditional metal-on-metal bearings in industrial applications. Bearings with an elastomeric layer are less sensitive to misalignment or eccentric loads, low levels of lurbicant, and the presence of solid particulates in the lubricant [7]. All these characteristics make bearings with compliant surfaces a promising area for innovation. But their behavior is considerably different from rigid bearings, which necessitates new methods of analysis and design guidelines.

1.1 Literature Review

Booker and Boedo [8] applied a nodal inverse hydrodynamic (NIH) formulation, introduced by Booker [9], for solving the soft EHL problem of Figure 1.1. This NIH formulation tracks the relative nodal displacements of the elastic surface from the indenter, rather than the absolute displacements of both surfaces. This is an extension and simplification of the method introduced by Booker and Shu [10]. Their simulated results are shown in Figures 1.2 and 1.3. Simulated time histories of film thickness were compared with experimental data published by Gaman et al. [5]. Their formulation modeled the thin, elastic layer as a semi-infinite elastic halfspace. This formulation produced predictions that agreed well with

experimental data for a 6 mm thick layer. However, using a halfspace model gives no consideration for the effects of the thickness of the layer, while the experimental data shows a clear difference between the results for 6 mm and 1 mm thick layers, shown in Figures 1.4 and 1.5. Interestingly, this paper notes that as time progresses, the EHL film pressure distribution approaches the Hertzian dry contact stress distribution.

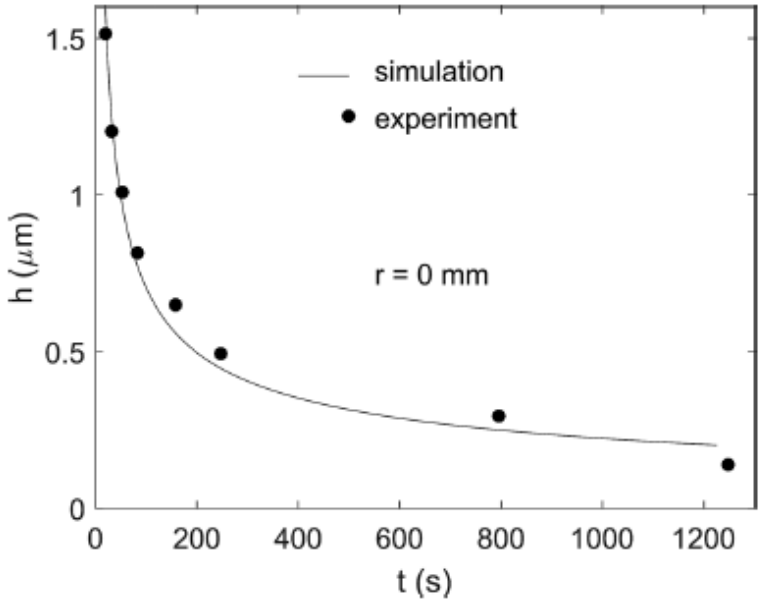

Figure 1.2 Central film thickness for 6 mm layer, 0.13N load from Booker and Boedo [8]

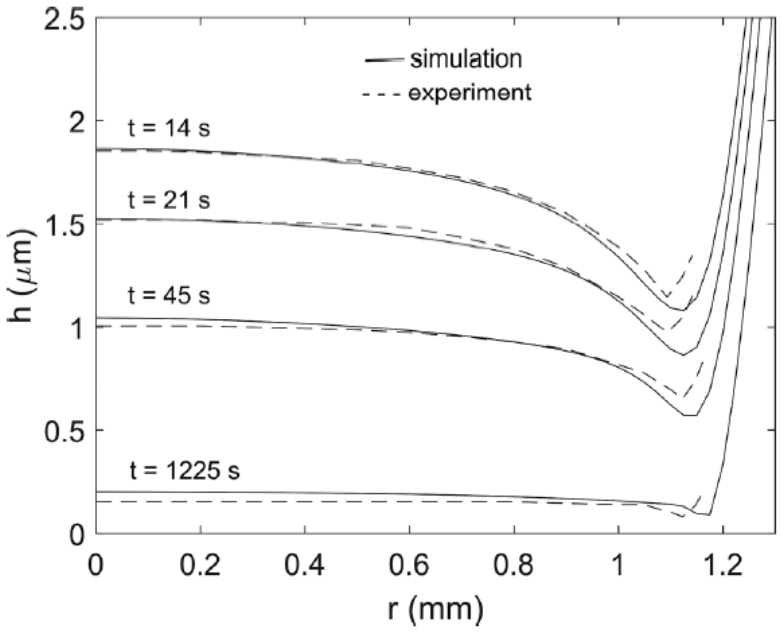

Figure 1.3 Film thickness for 6 mm layer, 0.13N load from Booker and Boedo [8]

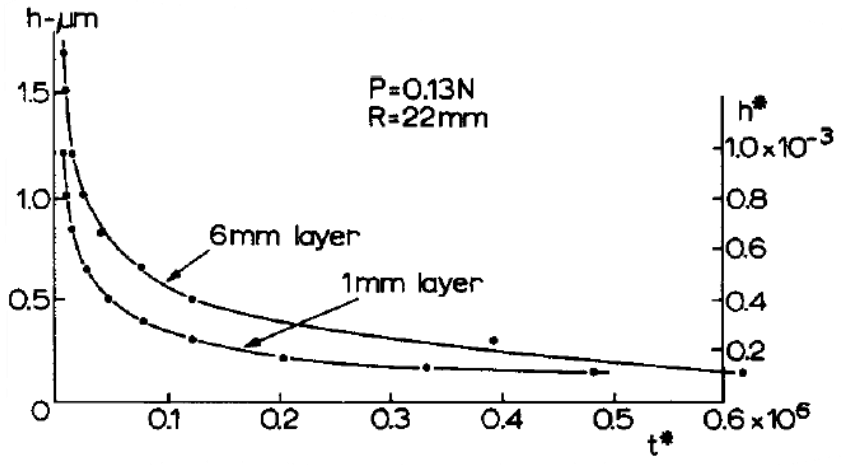

Figure 1.4 Experimental Results for central film thickness, taken from Gaman et al. [5]

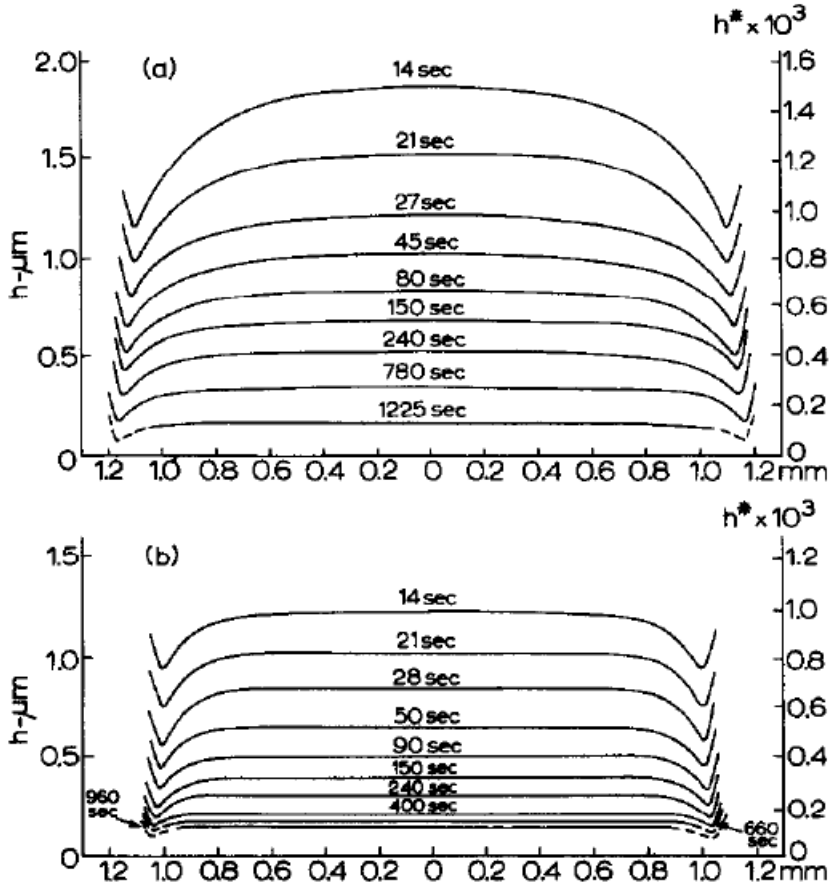

Figure 1.5 Experimental Results for film thickness, P=0.13 N, R=22 mm, (a) 6 mm layer, (b) 1 mm layer, taken from Gaman et al. [5]

Another route for generalization is to examine the assumptions typically made for hard EHL problems and the effects of relaxing them in the context of a soft EHL problem. This is the approach taken by Chen et al. [11] for the case of a line contact EHL problem for a rotating cylinder. They identify four specific assumptions of hard EHL problems that cannot necessarily be made for soft EHL problems. Relaxing these assumptions yields the four considerations:

1) Tangential surface velocities altered by curvature
2) Real indenter profile
3) Load balance must rely on deformed geometry
4) Finite (not infinitesimal) deformation of the elastic surface

The first item does not apply to normal approach EHL because squeeze-film lubrication action is absent of tangential surface velocities. However, the other three characteristics can be examined. For the second item, a circular or spherical indenter is often approximated as a paraboloid in a hard EHL problem since the contact region is very small relative to the dimensions of the bodies. But in a soft EHL problem, the contact radius can grow to be of the same magnitude as the radius of the indenter. This requires possible consideration of the real indenter profile since the error of the paraboloid approximation increases as the radius of the contact region grows. Third, the nodal forces from film pressure are often assumed to all act only in the vertical axis. However, as the contact radius and deformations become larger, the actual deformed geometry may need to be accounted for. Since the pressure results in a force along the surface normal, the curvature of the surfaces may become significant such that the surface normals and resultant nodal forces cannot be approximated as vertical. Fourth, in a soft EHL problem, the assumption of infinitesimal deformation may not be appropriate, as the deformations of the elastic surface can become large. Chen et al. accounted for this by using Green strain calculations.

Jaffar [12,13] made semi-analytic predictions of the film thickness for the normal approach EHL problem by making use of Grubin's approximation for a spherical indenter. This is the assumption that the deformation of the elastic surface under lubricated conditions is identical to the dry deformation. This is justified by the relatively small thickness of the fluid film. Applying this assumption leaves the film thickness as a function of time only. Jaffar then applies two separate boundary conditions and compares the results. The first is

Higginson's boundary condition, where the pressure is assumed to be zero at the outer edge of the contact region. The second is Fein's boundary condition, where the pressure is defined to be some definite value $p = p_0$ at $r = 0$. Non-dimensionalized results are given for both of these cases, and also compared to Hertzian contact.

Castelli et al. [14] numerically and experimentally examined a squeeze film lubrication problem for the specific case of a thrust bearing with a central hydrostatic feed. Their approach used the exact results from linear elasticity for an infinite thin elastic slab perfectly bonded to a rigid support. However, their results are limited to the case of a flat contact. But they give a good outline of the effect of the compliant surface on bearing performance. The compliance of the soft, elastic layer allows for the formation of a "puddle" of lubricant where the pressure is highest (usually centrally). When the layer is also incompressible, as is typical of the rubber liners used in bearings, this displacement in the layer would tend to cause the outer edges to swell and contribute to sealing off the film at the outer edge.

The Nodal Inverse Hydrodynamic (NIH) formulation applied in this thesis work is notable both in its generality and computational efficiency. Booker introduced this formulation in a general form applicable to a general EHL problem [15]. This can include arbitrary bearing geometry, tangential entrainment velocities, piezovicous effects, and arbitrary loading. It also has the immense computational advantage of being a non-iterative algorithm. This is a great improvement over the Newton-Raphson method previously used, which does require iteration at every time step to produce a solution to an implicit function of the displacement and pressure [1]. Despite its computational cost, a majority of EHL work has been done using a Newton-Raphson method. In a list of 20 publications on EHL models of a human hip joint, Mattei et al. report that 14 of them used a Newton-Raphson method to obtain results [6].

1.2 Thesis Objectives

The purpose of this thesis is to investigate the EHL normal approach of a rigid axisymmetric indenter onto a soft elastic structure with general geometry specifications. This will include a linearly elastic layer with finite or infinite thickness. The compliance of the finite thickness layer will be based on the work by Conway et al. [16] on thin strips and slabs. Two indenter

geometries will be examined: paraboloid and conical. In addition, the NIH method will be applied to fully investigate the experimental results from Gaman et al. [5].

An important facet of the thesis work is to examine the placement of boundary conditions. For this particular problem, the only fluid boundary condition is that the fluid pressure is zero (atmospheric) at the edge of the fluid film. For bounded films defined by the geometry of the indenter ($R = \text{constant}$), this is not a problem. For unbounded films ($R = \infty$), the question becomes, where is the edge of the film? How far from the center of the contact region does the boundary condition need to be placed to obtain reasonable results, without carrying out an undue amount of calculation for pressures and deformations far outside the "contact" region that have negligible effect on the actual results? There doesn't seem to be any work done specifically on this topic.

The problem will be cast in non-dimensional form as a means of investigating design trends tied to the curvature/slope of the indenter and the geometry of the elastic structure.

Chapter 2

Problem Formulation

2.1 Reynolds Equation

For the axisymmetric, isoviscous, squeeze film case, the relevant form of the Reynolds equation in cylindrical coordinates is given by

$$\frac{\partial}{\partial r}\left(rh^3\frac{\partial p}{\partial r}\right) = 12\mu r\frac{\partial h}{\partial t} \tag{2.1}$$

where the film thickness for a paraboloid indenter with curvature κ, as shown in Figure 2.1, is given by

$$\begin{aligned} \mathrm{h}(r,t) &= h_0 + \frac{\kappa}{2}r^2 + \delta^a(r,t) - \delta^b(t) \\ &= h_0 + \frac{\kappa}{2}r^2 + \mathcal{L}[p(r,t)] - \mathrm{e}(t) \end{aligned} \tag{2.2}$$

and for a conical indenter with slope β, as shown in Figure 2.2, is given by

$$\begin{aligned} \mathrm{h}(r,t) &= h_0 + \beta r + \delta^a(r,t) - \delta^b(t) \\ &= h_0 + \beta r + \mathcal{L}[p(r,t)] - \mathrm{e}(t) \end{aligned} \tag{2.3}$$

subject to the constraints

$$\mathrm{F} = 2\pi\int_0^R p(r,t)r\,\mathrm{d}\,\mathrm{r} \tag{2.4}$$

$$\mathrm{p}(r = R, t) = 0 \tag{2.5}$$

and initial conditions

$$\mathrm{e}(\mathrm{t} = 0) = 0 \tag{2.6}$$

$$\mathrm{p}(\mathrm{r}, \mathrm{t} = 0) = 0 \tag{2.7}$$

The linear operator $\mathcal{L}$ relating pressure and film thickness is defined by the model of the elastic layer. This thesis will investigate in detail two analytical models. The first model is the elastic halfspace, which has infinite thickness and radius, which has been studied previously [8]. The second model is an analytical representation of a thin, linearly elastic slab provided by Conway [16], which has finite thickness and infinite radius.

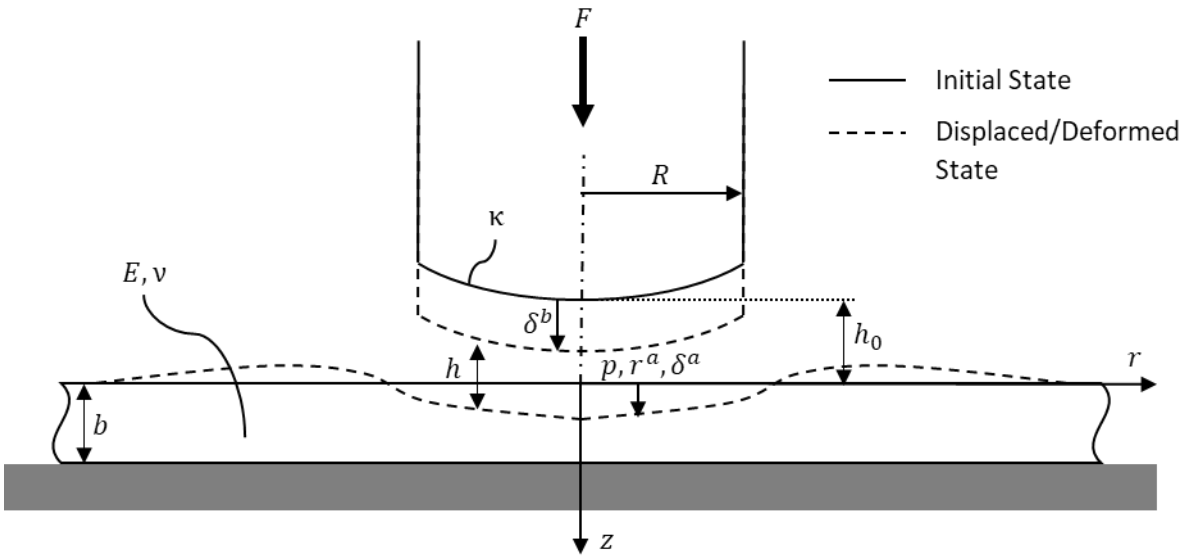

Figure 2.1 Paraboloid indenter squeeze film schematic

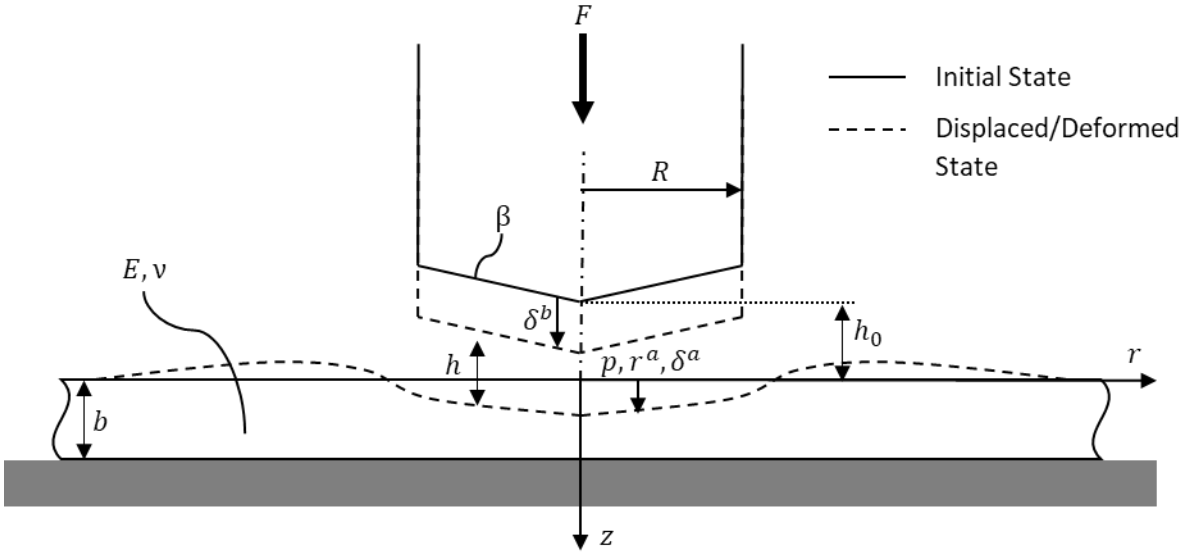

Figure 2.2 Conical indenter squeeze film schematic

2.2 Load Function

As noted by Booker and Boedo [8], the choice of loading is unidirectional but otherwise arbitrary for this squeeze-film problem. The usual loading assumption for bearing problems is a step load, often from a mass under gravity supported by the fluid film. The release of the load is implicitly assumed to be a "perfect" step, with a discontinuity between zero load and full load. However, this discontinuity implies an infinite, or undefined, derivative of the load at the time of the step. This is problematic for the NIH approach, which depends explicitly on the rate of loading. Therefore, in this work, the idealized step load is replaced by the following load function:

$$\mathrm{F}(t) = F_0[1 - \exp(-\alpha^2 t^2)] \tag{2.8}$$

This function introduces the load rate parameter α which controls the "steepness" of the step function. Increasing α increases the rate at which the load rises from zero to full loading. In fact, a load of this form approaches a step load, but this function and all its derivatives are continuous at all points. Since many experimental studies implicitly assume a step load, there is no data available to suggest what a realistic value of this parameter should be to model real loadings. However, as will be shown, simulated results are fairly insensitive to variation over a wide range of values for α, even over several orders of magnitude.

To mimic a step load, the value of α can be chosen so that the rise time of the function is negligible compared to the characteristic times of the system response. For a given fraction of the full load, $f = \frac{F}{F_0}$, the rise time to reach this fraction is given by:

$$\mathrm{t} = \frac{1}{\alpha}\sqrt{-\ln(1-f)} \tag{2.9}$$

For example, the appropriate value of α for a specified 99% rise time is given by

$$\alpha = \frac{\sqrt{\ln 100}}{t_{99\%}} \approx \frac{2.146}{t_{99\%}} \tag{2.10}$$

and this relation can easily be inverted to give the 99% rise time for a chosen value of α.

As seen from the load-pressure relation in equation (2.4) and the load function, the inertia of both the indenter and the fluid are neglected. Instead, these relations represent the

instantaneous static equilibrium of the fluid pressure and the external load. This is justified by the exceedingly small displacements, which lead to negligibly small accelerations.

2.3 Hertz Contact Radius and Pressure

The problem shown in Figure 2.1 is extremely similar to the comparatively simple problem of Hertzian dry contact. Finding the surface deflections and stresses under dry, frictionless contact between a paraboloid indenter and an elastic halfspace is classical problem in contact mechanics. As such, the results are well-known and widely published and have been used as approximations for more complex problems.

Grubin introduced the approximation of Hertzian deformation for lubricated cylindrical roller [17]. This approximation works well when the lubricated region is very small relative to the dimensions of the bodies involved. However, for the current case of a thin elastic layer, the radius of the lubricated region can be as large as the thickness of the layer, and the preceding condition is not satisfied.

Moreover, since the effect of a finite thin layer is to increase the apparent stiffness of the surface, the dry contact radius on a thin slab is necessarily smaller than for an elastic halfspace. Nevertheless, the Hertz contact radius can be useful for obtaining a sense of scale for the contact zone even for a non-Hertzian problem.

The dry contact radius a of the Hertz contact region is well known and given by [18]

$$\mathrm{a} = \left(\frac{3F_0(1-\nu^2)}{4\kappa \mathrm{E}}\right)^{1/3} \tag{2.11}$$

The Hertzian pressure distribution over this contact region is ellipsoidal in form, given by

$$\mathrm{p}(r) = p_0\left(1-\frac{r^2}{a^2}\right)^{\frac{1}{2}} \tag{2.12}$$

$$p_0 = \frac{3F_0}{2\pi a^2} \tag{2.13}$$

where p_0 is the peak central pressure, which is $\frac{3}{2}$ times greater than the average pressure over the contact region.

2.4 Sneddon Contact Radius and Pressure

The Hertz contact radius only applies to indenters that can be reasonably approximated by a paraboloid profile. Sneddon [19,20] extended this work to arbitrary (axisymmetric) indenter profiles. Particularly, for a conical indenter with a profile as shown in Figure 2.2, the dry contact radius a is given by

$$\mathrm{a} = \left(\frac{2F_0(1-\nu^2)}{\pi\beta E}\right)^{1/2} \tag{2.14}$$

and the pressure distribution is given by

$$p(r) = \frac{F_0}{\pi a^2}\cosh^{-1}\left(\frac{a}{r}\right) = \frac{\beta E}{2(1-\nu^2)}\cosh^{-1}\left(\frac{a}{r}\right) \tag{2.15}$$

This pressure distribution, shown in Figure 2.3, is entirely different from the Hertzian pressure. The peak central pressure is theoretically infinite, due to the geometric discontinuity of the indenter profile. In practice, the indenter is, of course, not perfectly sharp, and this singularity is avoided.

The squeeze film associated with a conical indenter is completely different than that of a paraboloid one. Boedo and Booker [21] showed that for a rigid conical indenter approaching a rigid surface, the squeeze film load capacity is finite. This is in contrast to the theoretically infinite load capacity of the squeeze film between a rigid paraboloid indenter and a rigid surface.

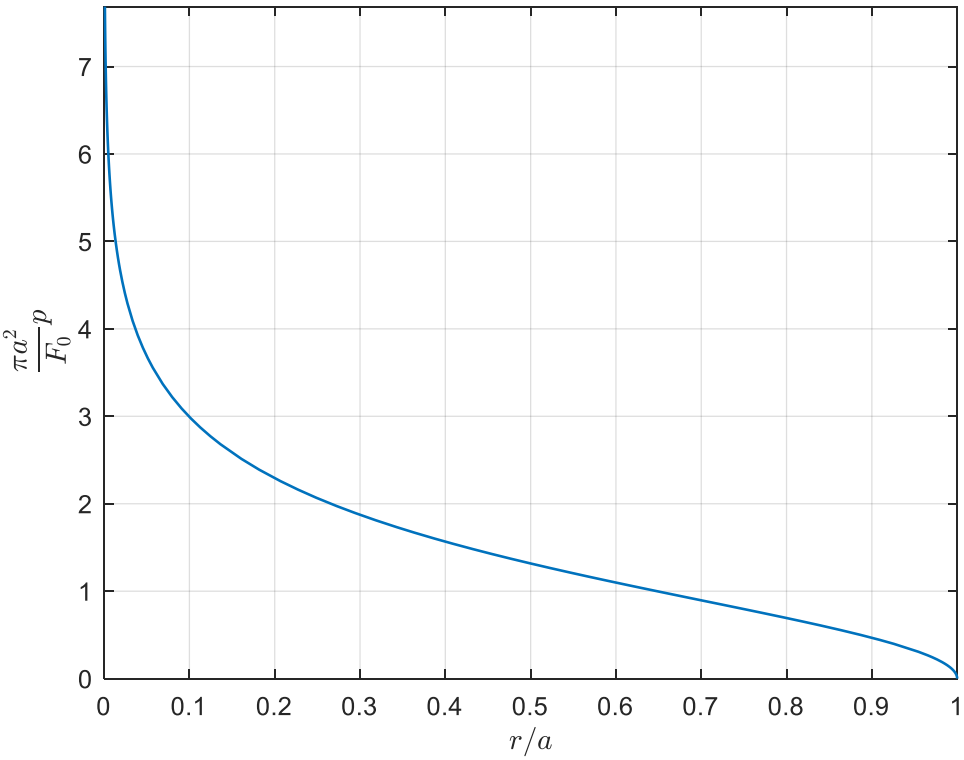

Figure 2.3 Dry contact pressure distribution for a conical indenter into an elastic halfspace

Chapter 3
Solution Method

3.1 Finite Element Discretization

The spatial dimension of the problem represented by a two-dimensional fluid film is discretized by the finite element method into concentric, axisymmetric elements with equal incremental radii. Using axisymmetric elements enforces circumferential symmetry of the solution, which is assumed due to the axisymmetry of the problem [2]. A mesh of this style also has many fewer elements and nodes than a comparably dense mesh of 2D triangles, which significantly reduces computational load. Figure 3.1 shows a schematic of the elements and nodes for this 1D mesh. In this work, finite elements with linear shape functions are used to discretize the continuous values of film thickness and pressure to nodal thickness and pressure in the film.

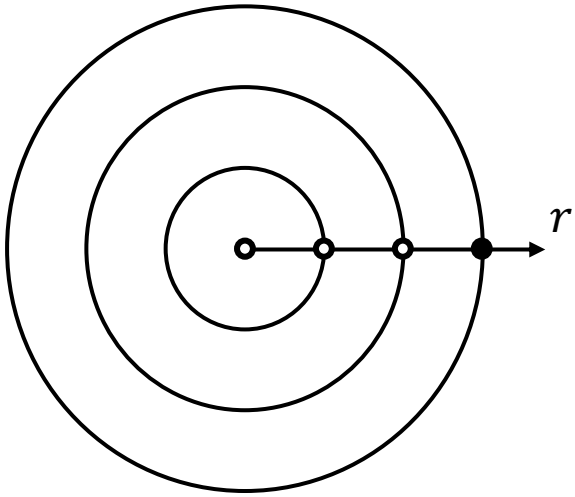

Figure 3.1 Elements and nodes of 1D axisymmetric mesh from [2]

For this specific problem, a number of simplifications can be made to the very general solution strategy laid out in [1]. The notable assumption is pure squeeze action, with no fluid entrainment from tangential surface velocities. The fluid is also assumed to be isoviscous since the film pressure does not rise significantly due to the compliance of the elastic layer. By discretizing the spatial dimension of this system, the problem can be reduced to a system of coupled ordinary differential equations (ODEs). The ODE suite built into MATLAB is designed for this type of initial value problem, and the details of their implementation are

available elsewhere [22]. For this current work, the ODE-solver *ode15s* is used to handle the stiff behavior of the system.

3.2 Nodal Inverse Hydrodynamic Approach

The Nodal Inverse Hydrodynamic (NIH) approach was initially developed by Booker and Shu [10]. It was later extended and clarified by Booker [15], Boedo [1], and Booker and Boedo [8]. Nodes are partitioned into two sets: those with fixed pressure boundary condition, and those with state variables with initial separation distance. The NIH method explicitly depends on the load rate, which is in contrast to previous approaches (e.g. Newton-Raphson).

The NIH method tracks the displacement of the elastic surface relative to the rigid indenter surface, rather than the absolute displacements of both surfaces. This approach has the highly desirable advantage of numerical stability even for large rigid body motions - such as in an engine piston rod bearing, where taking the difference of two large absolute displacements may result in loss of precision. The absolute displacements of each surface can be calculated post-simulation, along with the film thickness and pressure. This grants considerable computational advantage over approaches that track both nodal pressure and film thickness, as only half of those values need to be carried through the full simulation calculations.

The NIH method for the squeeze film case is described in detail elsewhere [1,8,15] and is summarized as follows:

Referring to Figures 2.1 and 2.2, elastic relations for the elastic layer are given by

$$\widetilde{K}\,\underline{\delta}^{a}(t) = \underline{r}^{a}(t) \tag{3.1}$$

$$C\,\underline{p}(t) = \underline{\delta}^{a}(t) \tag{3.2}$$

$$\widetilde{K} = A\,C^{-1} \tag{3.3}$$

$$A\,\underline{p}(t) = \underline{r}^{a}(t) \tag{3.4}$$

where the vectors

$$\underline{p} = \begin{Bmatrix} p_1 \\ \vdots \\ p_n \end{Bmatrix} \quad \underline{\delta}^{a} = \begin{Bmatrix} \delta_1^a \\ \vdots \\ \delta_n^a \end{Bmatrix} \quad \underline{\mathrm{r}}^{a} = \begin{Bmatrix} \mathrm{r}_1^a \\ \vdots \\ \mathrm{r}_n^a \end{Bmatrix}$$

represent the nodal pressures, nodal displacements of the elastic surface, and nodal forces on the elastic surface, respectively.

Static equilibrium of system is given by

$$-\underline{G}^T \underline{r}^a(t) = F(t) \tag{3.5}$$

$$-e(t)\underline{G} = \underline{\delta}^b(t) \tag{3.6}$$

where the vector

$$\underline{\delta}^b = \begin{Bmatrix} \delta_1^b \\ \vdots \\ \delta_n^b \end{Bmatrix}$$

represents the nodal displacements of the surface of the indenter. All entries of this vector are equal, since the indenter is rigid.

Combining relations 3.1, 3.5, and 3.6 yields

$$K\underline{d} - F(t)\underline{B} = \underline{r}^a \tag{3.7}$$

where

$$\underline{d} = \underline{\delta}^a - \underline{\delta}^b \tag{3.8}$$

$$K = \widetilde{K} - \widetilde{K}\,\underline{G}\left(\underline{G}^T \widetilde{K}\,\underline{G}\right)^{-1} \underline{G}^T \widetilde{K} \tag{3.9}$$

$$\underline{B} = \widetilde{K}\,\underline{G}\left(\underline{G}^T \widetilde{K}\,\underline{G}\right)^{-1} \tag{3.10}$$

The vector $\underline{d}$ represents the displacement of the elastic surface relative to the displaced indenter at each node.

Now all the nodes can be partitioned into two (disjoint) sets. At a given time step, nodal relative displacements in partition 1 are known, and nodal pressures in partition 2 are known. Equation 3.7 can thus be split:

$$K_{11}\underline{d}_1 + K_{12}\underline{d}_2 - F(t)\underline{B}_1 = A_{11}\underline{p}_1 + A_{12}\underline{p}_2 \tag{3.11}$$

$$K_{21}\underline{d}_1 + K_{22}\underline{d}_2 - F(t)\underline{B}_2 = A_{21}\underline{p}_1 + A_{22}\underline{p}_2 \tag{3.12}$$

The unknown displacements in partition 2 and unknown pressures in partition 1 can be found by

$$\underline{d}_2 = -(S_{22})^{-1}\left(S_{21}\underline{d}_1 - F(t)\underline{G}_2 - T_{22}\underline{p}_2\right) \tag{3.13}$$

$$\underline{p}_1 = (A_{11})^{-1}\left(K_{11}\underline{d}_1 + K_{12}\underline{d}_2 - F(t)\underline{B}_1 - A_{12}\underline{p}_2\right) \tag{3.14}$$

where

$$S_{21} = K_{21} - A_{21}(A_{11})^{-1}K_{11} \tag{3.15}$$

$$S_{22} = K_{22} - A_{21}(A_{11})^{-1}K_{12} \tag{3.16}$$

$$\underline{G}_2 = \underline{B}_2 - A_{21}(A_{11})^{-1}\underline{B}_1 \tag{3.17}$$

$$T_{22} = A_{22} - A_{21}(A_{11})^{-1}A_{12} \tag{3.18}$$

Similarly, the hydrodynamic relation for volumetric flow can be partitioned as

$$\underline{q} = K^p \underline{p} + K^h \underline{\dot{d}} \tag{3.19}$$

$$\underline{q}_1 = K_{11}^p \underline{p}_1 + K_{12}^p \underline{p}_2 + K_{11}^h \underline{\dot{d}}_1 + K_{12}^h \underline{\dot{d}}_2 \tag{3.20}$$

$$\underline{q}_2 = K_{21}^p \underline{p}_1 + K_{22}^p \underline{p}_2 + K_{21}^h \underline{\dot{d}}_1 + K_{22}^h \underline{\dot{d}}_2 \tag{3.21}$$

Differentiating 3.13 and substituting it into 3.20 yields

$$\underline{\dot{d}}_1 = {F_{11}}^{-1}[\underline{q}_1 - K_{11}^p \underline{p}_1 - K_{12}^p \underline{p}_2 - K_{12}^h (S_{22})^{-1} (\underline{G}_2 \dot{F} + T_{22} \underline{\dot{p}}_2)] \tag{3.22}$$

where

$$F_{11} = K_{11}^h - K_{12}^h (S_{22})^{-1} S_{21} \tag{3.23}$$

These equations allow the nodal relative displacements in partition 1, $\underline{d}_1$, to be tracked over time. All other results (e.g. nodal pressure, film thickness, absolute displacements) can be calculated from these relative displacements. Since these other results depend only on the relative displacements, they can be calculated as a post processing step after the time simulation is completed.

3.3 Elastic Halfspace

Booker and Boedo [8] previously published work on this problem approximating the thin elastomer layer as an infinitely wide and deep elastic halfspace. This model produced very good agreement with the experimental results of the 6mm layer trials from Gaman's experiments.

An important note is that the compliance matrix that results from this process is not symmetric, as a fully finite element model would produce.

3.4 Semi-Analytical Thin Slab

The compliance matrix for a thin, linearly elastic slab was derived from work by Conway [7]. This formulation specifically applies to a slab that is not bonded to the support surface but is allowed to displace radially along the bottom surface (i.e. frictionless support). The pressure at a node in the finite element mesh is represented as a constant pressure distribution extending half the width of each adjacent element, as shown in Figure 3.2 (node i is located at a radius of r_i, and c_j is the midpoint of element j). These incremental regions of constant pressure approximate the actual pressure distribution. With a suitably fine mesh, this series of

constant pressure increments provides a good approximation, especially in regions where the pressure gradient is small. Figure 3.3 shows an example of this stepped approximate pressure distribution overlaid on the continuous distribution it represents.

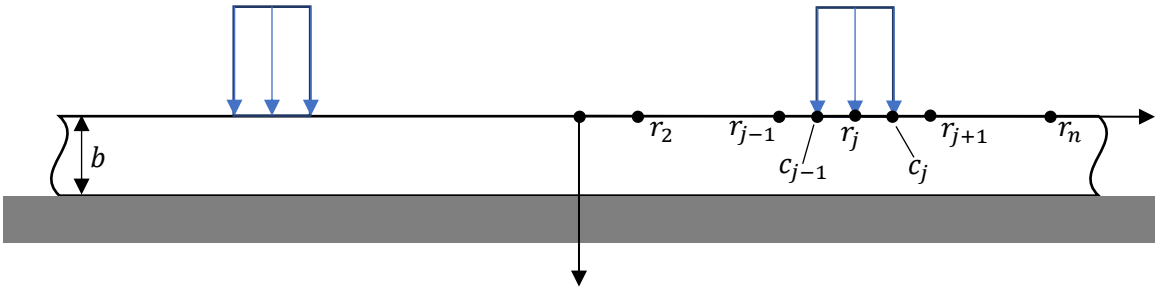

Figure 3.2 Infinite, thin elastic layer loaded with an annulus of uniform pressure

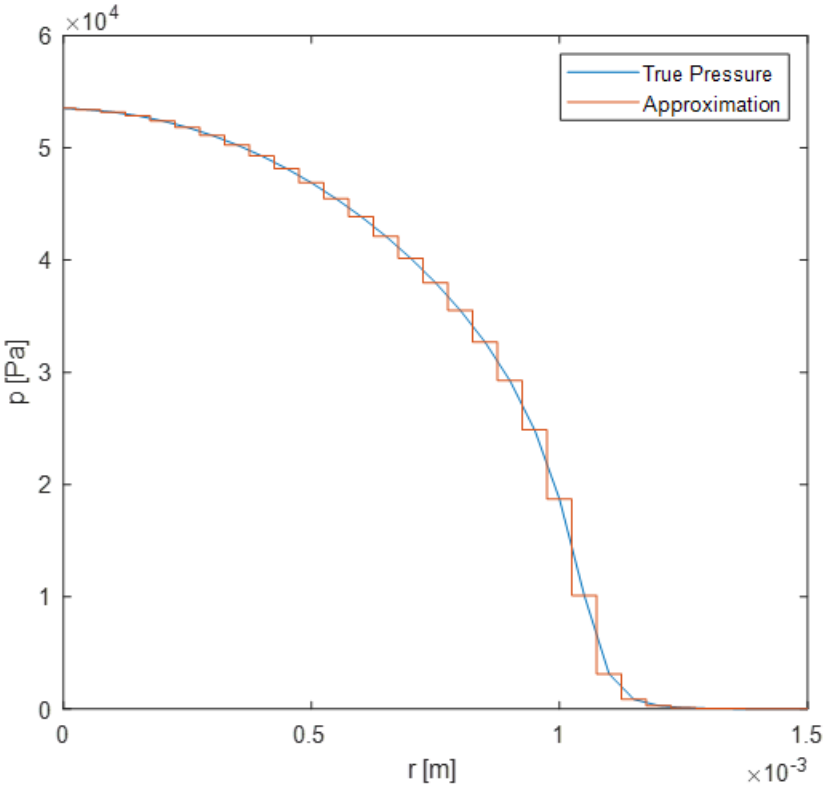

Figure 3.3 Example of the approximate pressure distribution used by the Conway thin slab analysis (40 elements)

The vertical displacement at a node located at a radius r_i due to a unit pressure at a node located at radius r_j is then given by the displacement of an annulus of pressure whose inner and outer radii are c_{j-1} and c_j, respectively. This annulus can be represented as the difference between uniform pressure distributions extending to c_{j-1} and c_j, respectively. **Error! Reference source not found.** gives the derivation, based on [16], of the vertical surface displacement due to a uniform pressure distribution. Evaluating the vertical displacement at each node due to a unit pressure at every other node yields a compliance matric C, whose entries are given by

$$\underline{\underline{C}}_{i1} = \frac{4(1-\nu^2)c_1}{E}\mathrm{I}\left(\bar{\mathrm{r}} = \frac{\mathrm{r_i}}{\mathrm{b}}, \bar{\mathrm{c}} = \frac{\mathrm{c_1}}{\mathrm{b}}\right)$$

$$\underline{\underline{C}}_{ij} = \frac{4(1-\nu^2)c_j}{E}\mathrm{I}\left(\bar{\mathrm{r}} = \frac{\mathrm{r_i}}{\mathrm{b}}, \bar{\mathrm{c}} = \frac{\mathrm{c_j}}{\mathrm{b}}\right) - \frac{4(1-\nu^2)c_{j-1}}{E}\mathrm{I}\left(\bar{\mathrm{r}} = \frac{\mathrm{r_i}}{\mathrm{b}}, \bar{\mathrm{c}} = \frac{\mathrm{c_{j-1}}}{\mathrm{b}}\right)$$

$$= \frac{4(1-\nu^2)}{E}\left[c_j\mathrm{I}\left(\bar{\mathrm{r}} = \frac{\mathrm{r_i}}{\mathrm{b}}, \bar{\mathrm{c}} = \frac{\mathrm{c_j}}{\mathrm{b}}\right) - c_{j-1}\mathrm{I}\left(\bar{\mathrm{r}} = \frac{\mathrm{r_i}}{\mathrm{b}}, \bar{\mathrm{c}} = \frac{\mathrm{c_{j-1}}}{\mathrm{b}}\right)\right] \quad 2 \le j \le n$$

where

$$1 \le i \le n$$

$$c_j = \frac{r_j + r_{j+1}}{2} \quad 1 \le j \le n-1$$

$$c_n = r_n = R$$

Again, this process produces a nonsymmetric compliance matrix, in contrast to a pure FEA approach.

This approach can be extended to use "tent functions" that provide C^0 continuity of the pressure distribution. Appendix CAppendix B shows this derivation. However, these calculations are much more computationally expensive, and several comparisons showed negligible difference in the results of EHL simulations run with compliance matrices calculated with a series of uniform pressures and calculated with a piecewise linear pressure distribution. These tests confirm that a series of uniform pressure serves as a good approximation, especially as their incremental widths become small.

3.5 Dowson & Taylor Thin Slab

Dowson and Taylor [23] give a simplified compliance matrix where elastic deflection is caused only by local pressure; namely,

$$u_z = \frac{bp}{E'} = \frac{bp}{E}\left(1 - \frac{2\nu^2}{1-\nu}\right) \tag{3.24}$$

This yields a diagonal compliance matrix since there is no interaction between pressure at one node and displacement at another. The result is a much higher apparent stiffness of the elastic layer, since only the local pressure can cause the surface to deflect.

This formulation is not suitable for incompressible materials because the effective elastic modulus E' goes to infinity and the displacement goes to zero as $\nu \to 0.5$.

Castelli and Rightmire [24] discuss this simple model of compliance, and the fact that it does not apply for materials with Poisson ratios close to 0.5. Dowson and Taylor note that the formula does give good agreement for values of the Poisson ratio up to about 0.45.

3.6 Simulation Procedure

Simulations are run until film thicknesses of zero are encountered. This condition necessarily terminates the simulation, since a film thickness of zero means that there is direct contact between the two surfaces, and full-film lubrication theory no longer applies. However, real surfaces are not perfectly smooth, as the current model assumes, and surface roughness would cause contact between the two surfaces even before the nominal film thickness reaches zero. Therefore, the results in the vicinity of extremely small minimum film thicknesses, well within the roughness of the surfaces, should be regarded with some skepticism.

Chapter 4

Dimensional Examples

4.1 Experimental Setup with Elastomer Layer

Gaman et al. [5] published experimental results for soft EHL film thicknesses obtained using the setup shown below Figure 4.1. The numerical parameters of these experiments are listed in Table 4.1. The listed applied forces are noticeably smaller than the mass of a solid steel ball with the given curvature. This is because the ball was mounted on a pivot with a counterweight on the opposite end. This setup serves to constrain the tangential movement of the ball as well as provide very fine adjustment of the applied load. There has been very little literature on this specific squeeze film problem due to the immense difficulty in measuring the transient thin films on soft surfaces. Indeed, this is the only experimental work for the case of pure squeeze film action with soft materials absent of any hydrostatic pressure feed serving to keep the bearing in a steady state. And there are no published simulation results that claim to fully predict all the experimental data presented in ref [5]. Booker and Boedo [8] used the model of an elastic halfspace to represent the thin elastic layer and were able to obtain good agreement with the case for a 6mm layer and load of 0.13N. However, no effort was made by the authors to account for the other experimental cases reported by Gaman et al. [5].

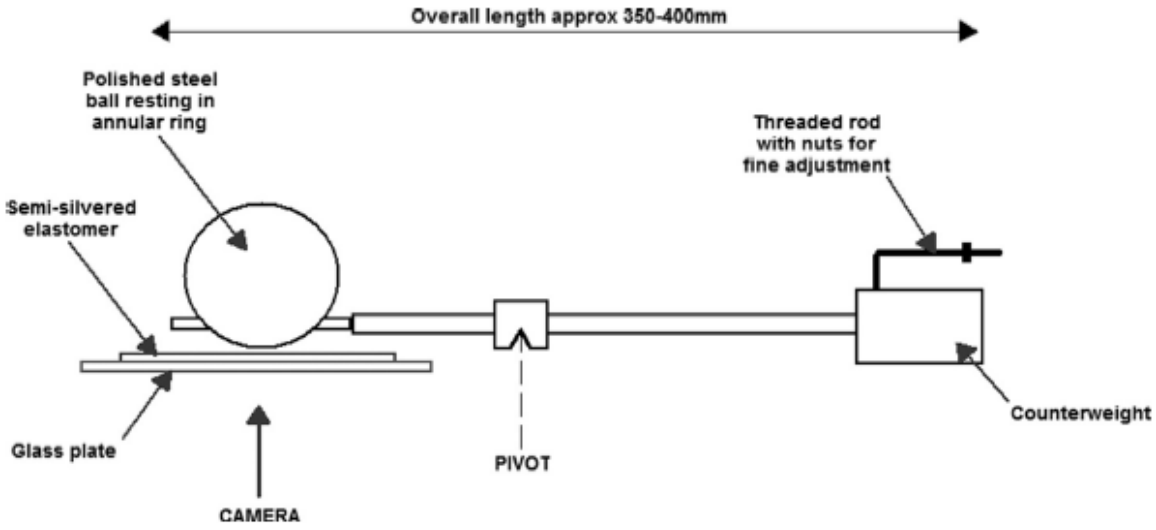

Figure 4.1 Apparatus for obtaining experimental data [25]

Since the contact region is small in comparison to the radius of the steel ball, the indenter is represented by a paraboloid profile which matches the curvature of the ball. The thin elastomer in the experimental setup is presumably bonded to the rigid support, or friction at the interface of the elastomer and glass support is sufficient to prevent radial deflection. However, the elastic slab model employed here does not include this condition and instead allows for radial deflection at the elastomer-glass interface (i.e. frictionless support), which theoretically lowers the apparent stiffness of the elastic layer.

Ignoring inertial effects, the experimental load is a perfect step function. However, as noted above, this is computationally problematic, so instead the ramped load is used with a ramp parameter of $\alpha = 1$. This corresponds to a 99% rise time of approximately 2 seconds, which is acceptably small based on the time scales of experiments with an elastomer layer. It will be shown later that the simulation results are insensitive to the value of α if it is below a certain threshold. The simulation results are obtained using a uniform mesh of 120 finite elements (121 nodes).

Gaman provides central film thickness time history for four cases under light loading: elastic layer thickness of 1mm and 6mm each loaded with 0.13N and 0.065N. For the two cases where the loading is 0.13N, the film thickness profiles are plotted at a series of time steps. Gaman also provides central film thickness time history for a 5mm elastomer layer heavily loaded with a 60N weight. This case is discussed in section 4.3 in comparision with results from experiments with rigid surfaces, since that is how it was presented in [5].

Gaman specifies the initial clearance for the rigid experimental cases as 250μm, however, he does not explicitly state the initial clearance used for the cases with an elastomer layer. Comparing the two vertical scales given in Figures 5 and 6 of [5], the initial clearance appears to have been 1.25 mm, which is five times greater than that of the rigid cases. But this difference is relatively inconsequential to the dimensional results, because the initial clearance has little to no effect on the long-term behavior of the elastomer layered bearing. It is only of importance because the majority of the data provided in [5] is scaled by the initial clearance, and therefore the correct value must be used to scale the nondimensional results back to their physical dimensions.

Table 4.1 Dimensional specifications for experiments with elastomer layer

E	1.0	MPa	Young's modulus of elastomer
ν	0.5	-	Poisson ratio of elastomer
μ	0.5	Pa-s	Lubricant viscosity
b	1, 5, 6	mm	Layer thickness
κ	1/22.5, 1/300	1/mm	Indenter curvature
F_0	0.065, 0.13, 60	N	External load
p_{atm}	0	Pa	Atmospheric pressure
h_0	1.250	mm	Initial central film thickness
α	1	1/s	Load rate parameter

4.2 Comparison with Experimental Results with Elastomer Layer

Figures 4.2 - 4.5 show the central film thickness time history, $h_c(t) = h(r, t = 0)$, for four cases of elastic layer thickness (6mm and 1mm) and applied force (0.13N and 0.065N). For both cases with a 6mm layer, the numerical results based on the elastic halfspace and the Conway thin slab are essentially identical and agree very well with the experimental data, as shown in Figures 4.2 and 4.4. Figures 4.3 and 4.5 show good agreement between the Conway thin slab EHL simulation and the experimental data for the 1mm layer cases as well, while the elastic halfspace simulation overpredicts the experimental central film thickness. Results for the case of the 6mm layer loaded with 0.13N also agree with Booker and Boedo [8], who used an initial clearance of 250μm. This helps demonstrate the system's insensitivity to the initial clearance.

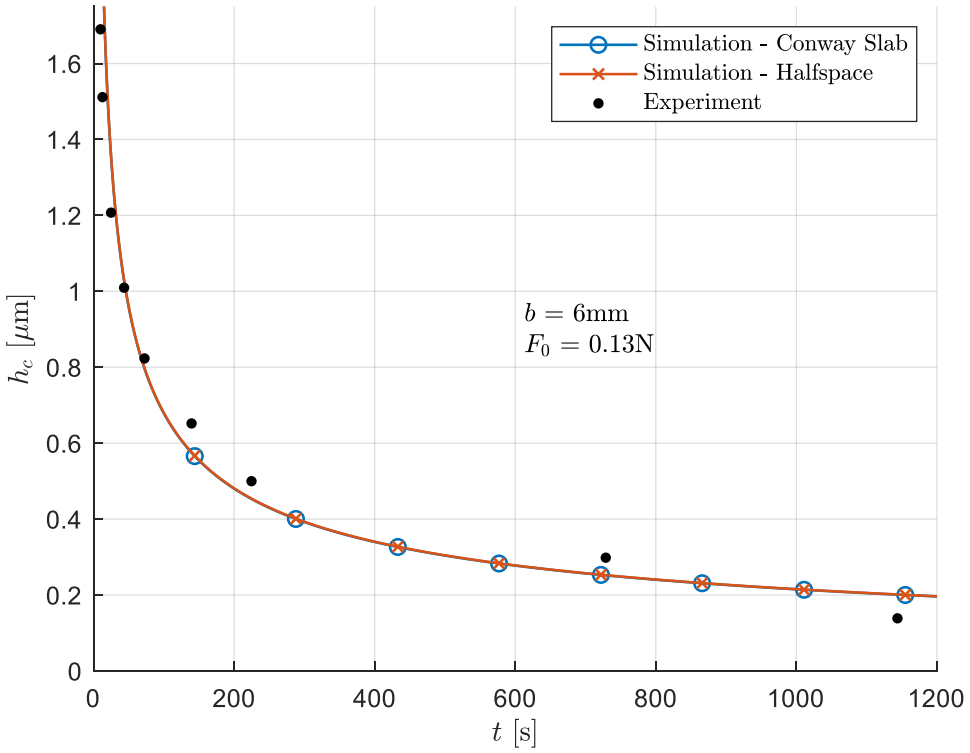

Figure 4.2 Central film thickness time history $h_c(t)$; 6mm layer, 0.13N load

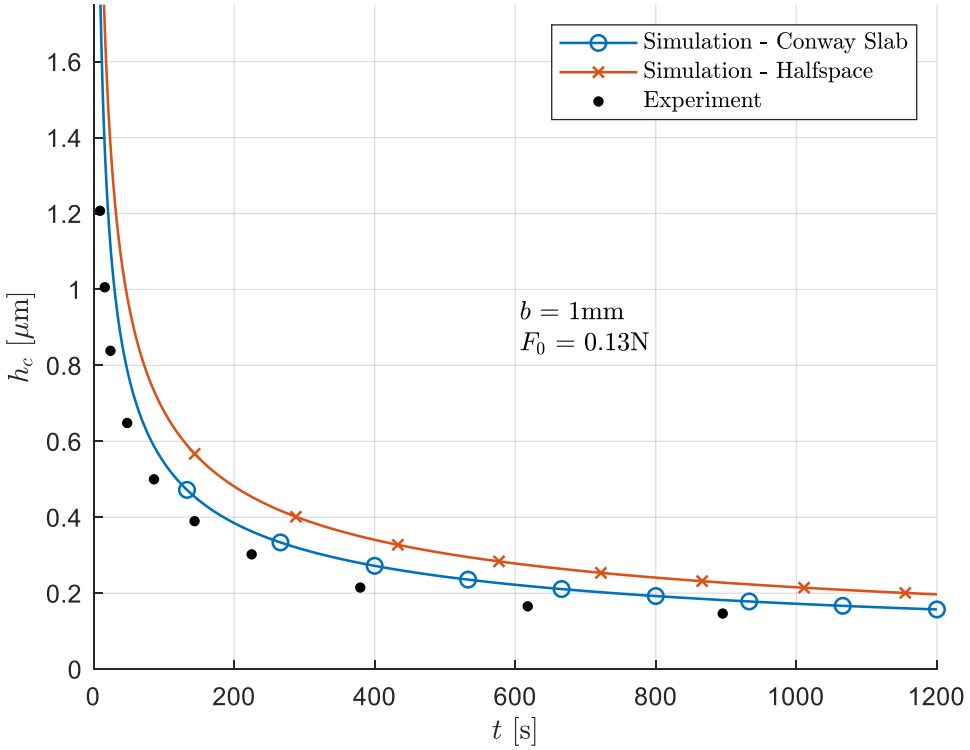

Figure 4.3 Central film thickness time history $h_c(t)$; 1mm layer, 0.13N load

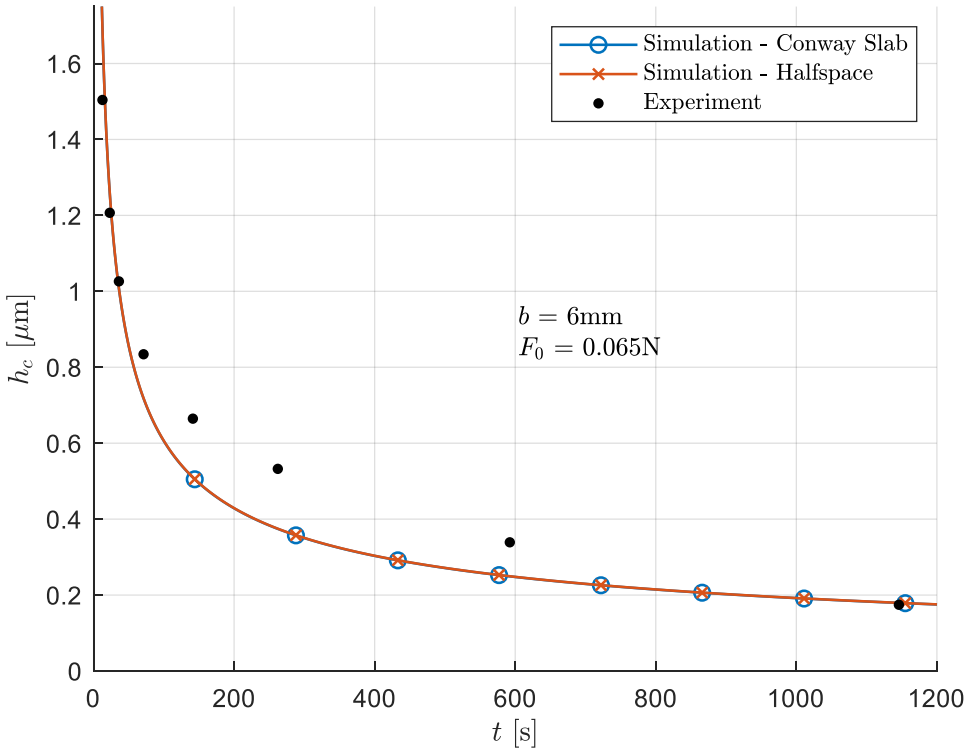

Figure 4.4 Central film thickness time history $h_c(t)$; 6mm layer, 0.065N load

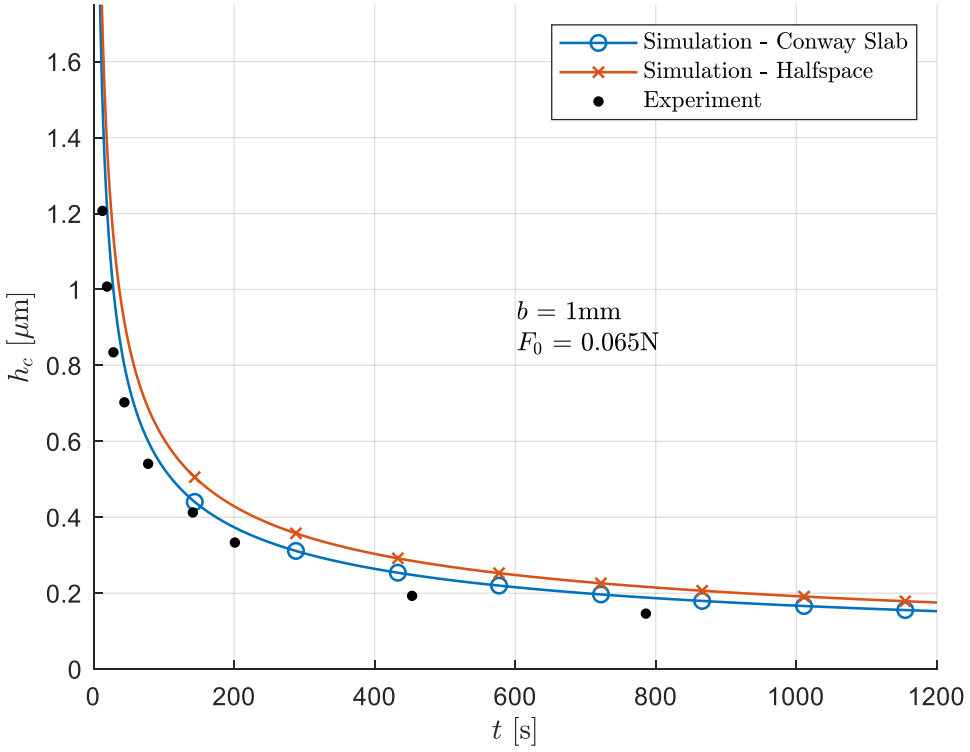

Figure 4.5 Central film thickness time history $h_c(t)$; 1mm layer, 0.065N load

Figures 4.6 - 4.9 show experimental film thickness profiles for two cases of the 6mm layer and 1mm layer loaded with 0.13N compared with simulation results. Figure 4.6 shows good agreement between the experimental data and simulation with the Conway thin slab, and Figure 4.7 shows virtually identical results obtained from the elastic halfspace. Figure 4.8 shows agreement between the data and the simulation with the Conway thin slab for the 1mm layer case, although not quite as good in the very early time steps. However, the elastic halfspace simulation significantly overpredicts the film thickness profiles for all but the very last time step, as seen in Figure 4.9.

The film thickness profiles all show several notable features. First, the development of a very flat inner “puddle” or “pocket” of lubricant. Second, the formation of a “shore” or ”ridge” on the surface of the elastomer layer. This latter effect would seem to reinforce the first, since this ridge pinches off the film from being squeeze out from underneath the indenter.

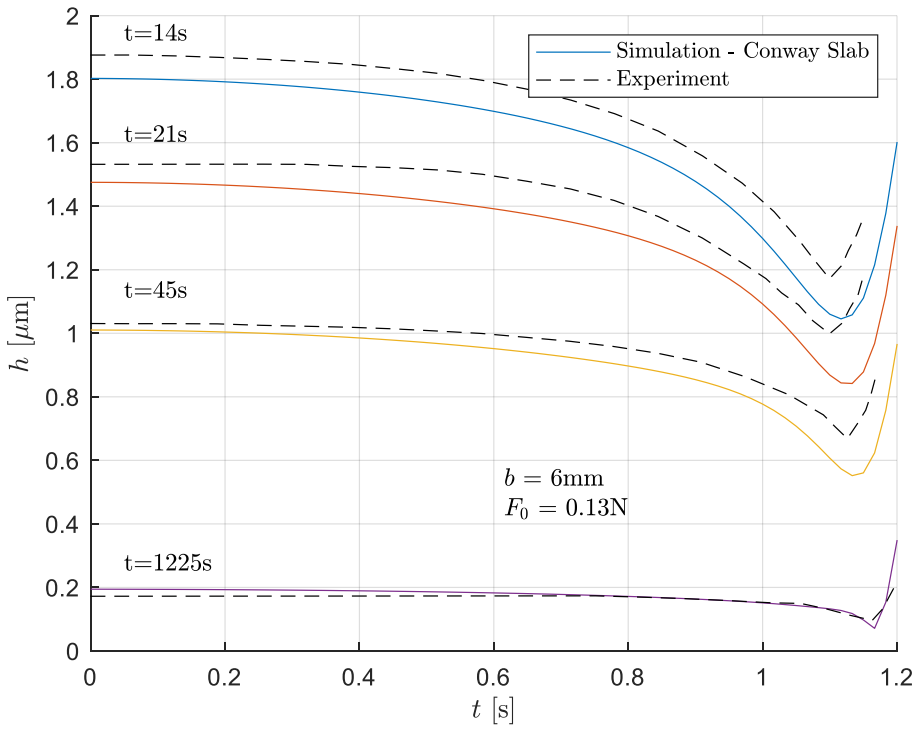

Figure 4.6 Film thickness profile $h(r,t)$; 6mm layer, 0.13N load; Conway thin slab comparison

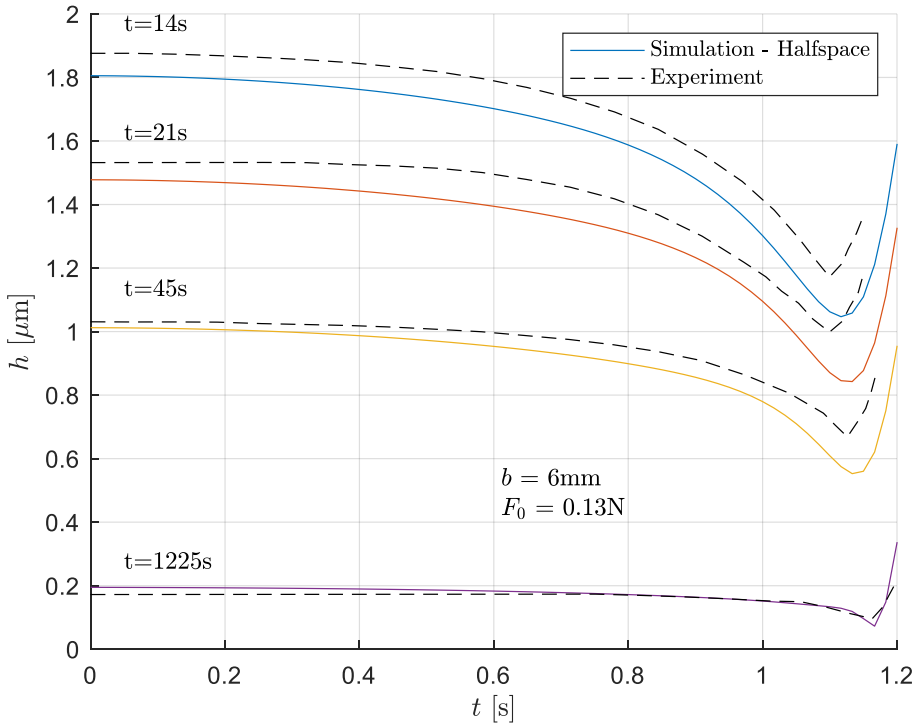

Figure 4.7 Film thickness profile $h(r,t)$; 6mm layer, 0.13N load; elastic halfspace comparison

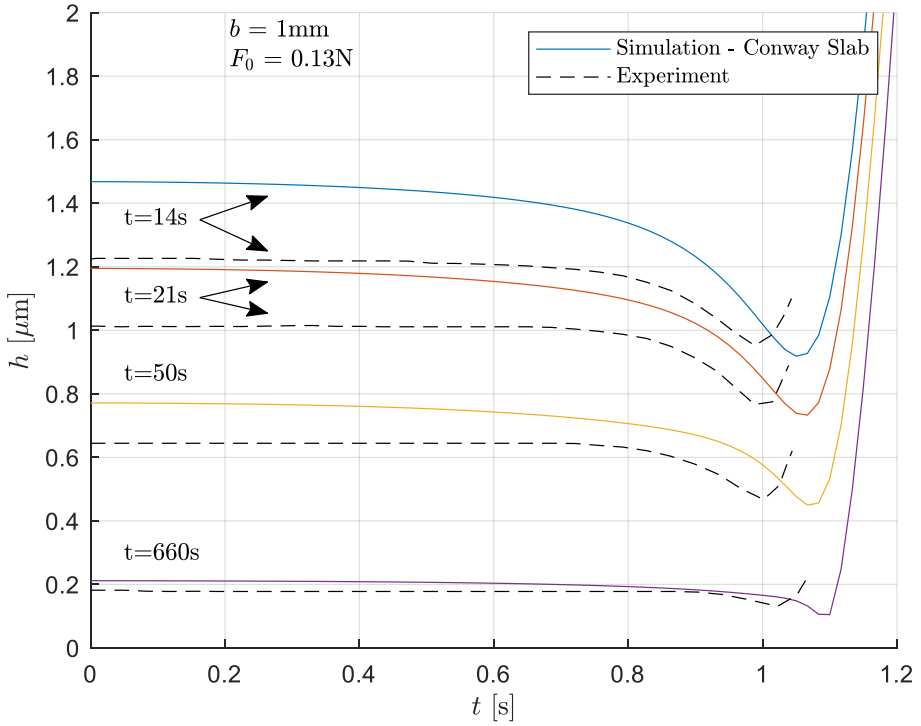

Figure 4.8 Film thickness profile $h(r,t)$; 1mm layer, 0.13N load; Conway thin slab comparison

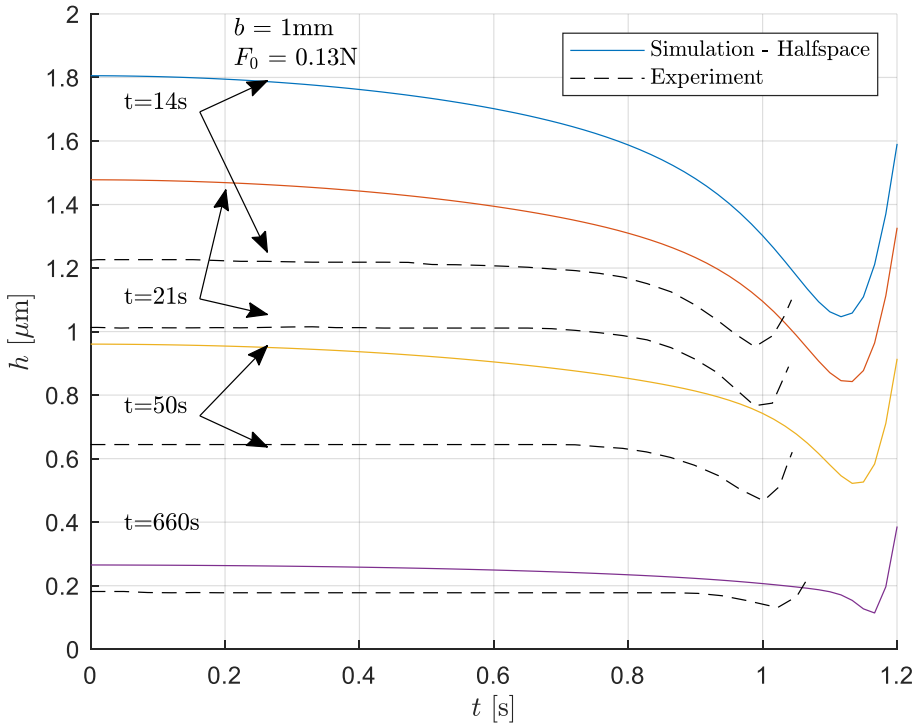

Figure 4.9 Film thickness profile $h(r,t)$; 1mm layer, 0.13N load; elastic halfspace comparison

Figures 4.10 - 4.15 show film pressure profiles at several time steps for each of the four cases above, along with the associated Hertz contact pressure for an identically loaded elastic halfspace under dry conditions. For the 6mm layer, Figures 4.10 and 4.12 show that the pressure profile quickly evolves to be nearly Hertzian in approximately 10 seconds, whereupon the system has reached a fairly steady state based on simulation with the Conway thin slab. Figures 4.14 and 4.15 show nearly identical results for simulations with an elastic halfspace

For the 1mm layer, Figures 4.11 and 4.13, the pressure settles to a near steady state distribution after about 5 seconds, however this distribution does not match the associated Hertzian pressure. As expected, the thin layer behaves much more stiffly than an elastic halfspace, so the apparent “contact radius,” where the pressure drops to essentially zero, is smaller and the peak pressure is significantly larger.

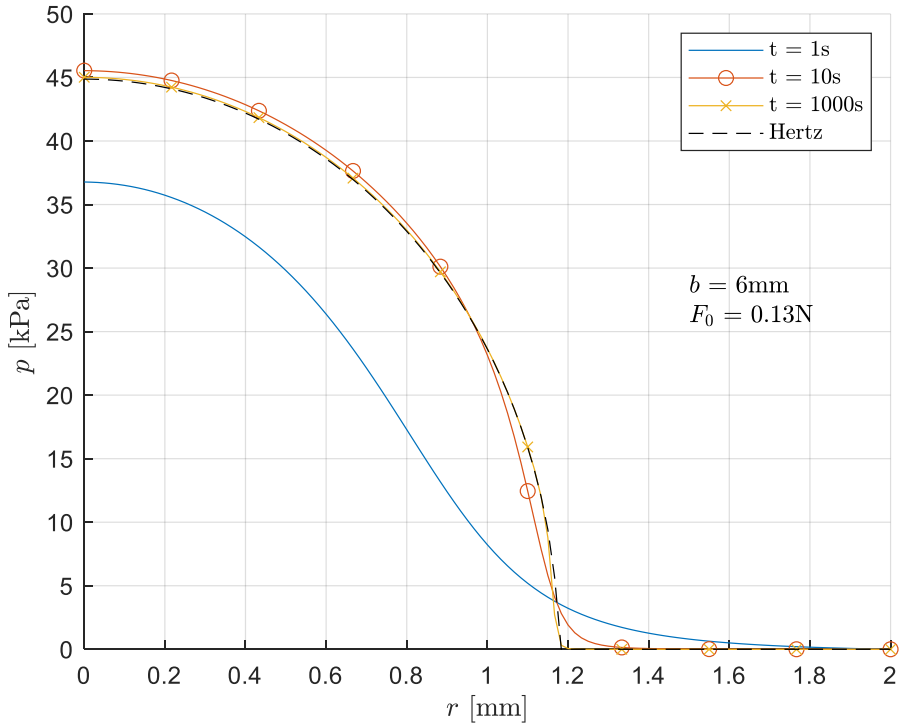

Figure 4.10 Film pressure $p(r,t)$, 0.13N Load, 6mm Conway thin slab

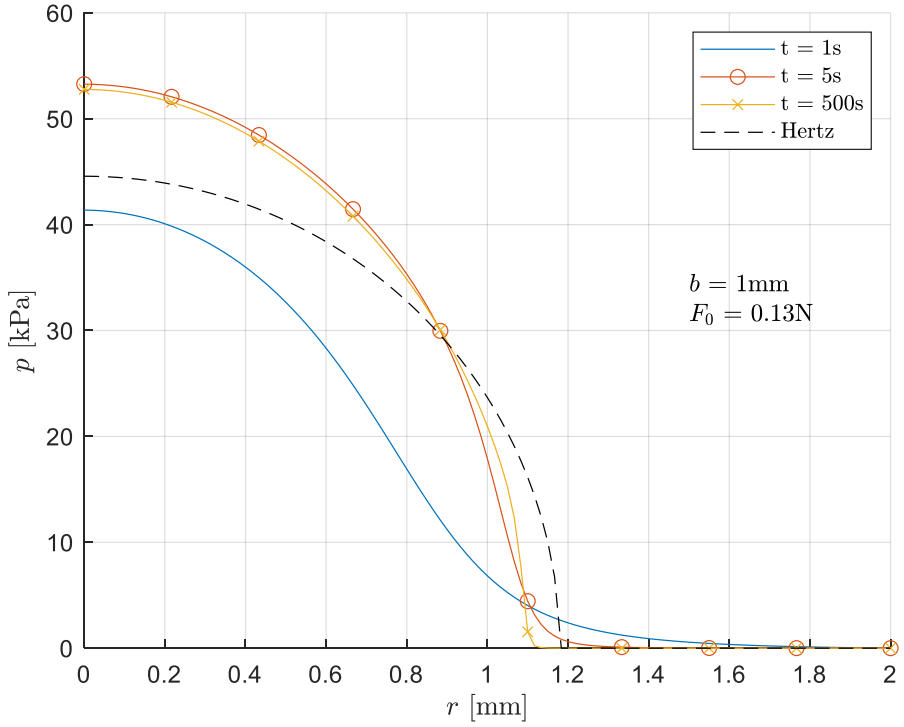

Figure 4.11 Film pressure $p(r,t)$, 0.13N Load, 1mm Conway thin slab

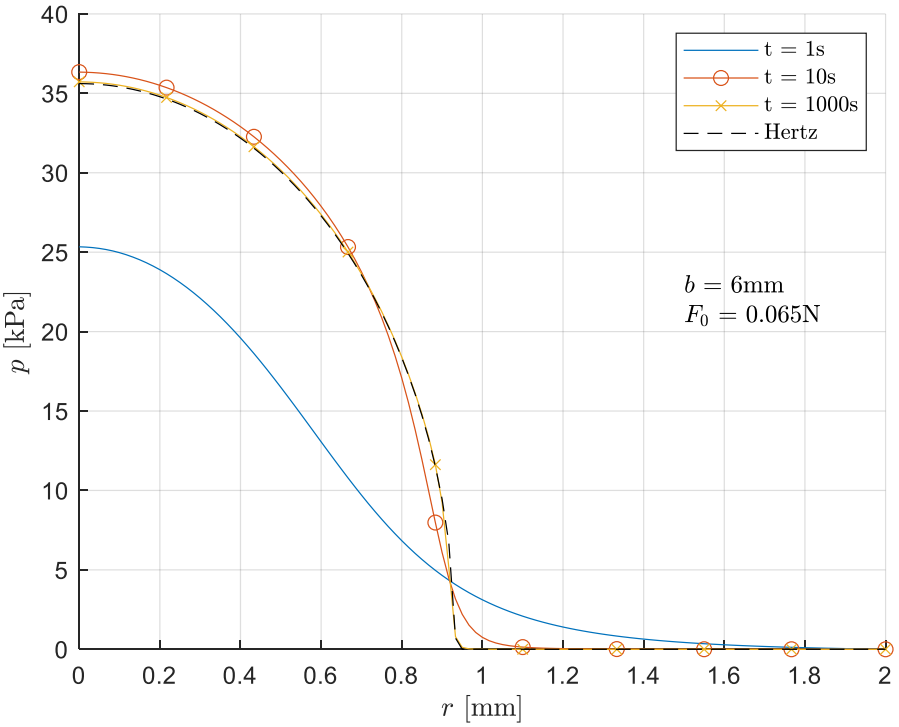

Figure 4.12 Film pressure $p(r,t)$, 0.065N Load, 6mm Conway thin slab

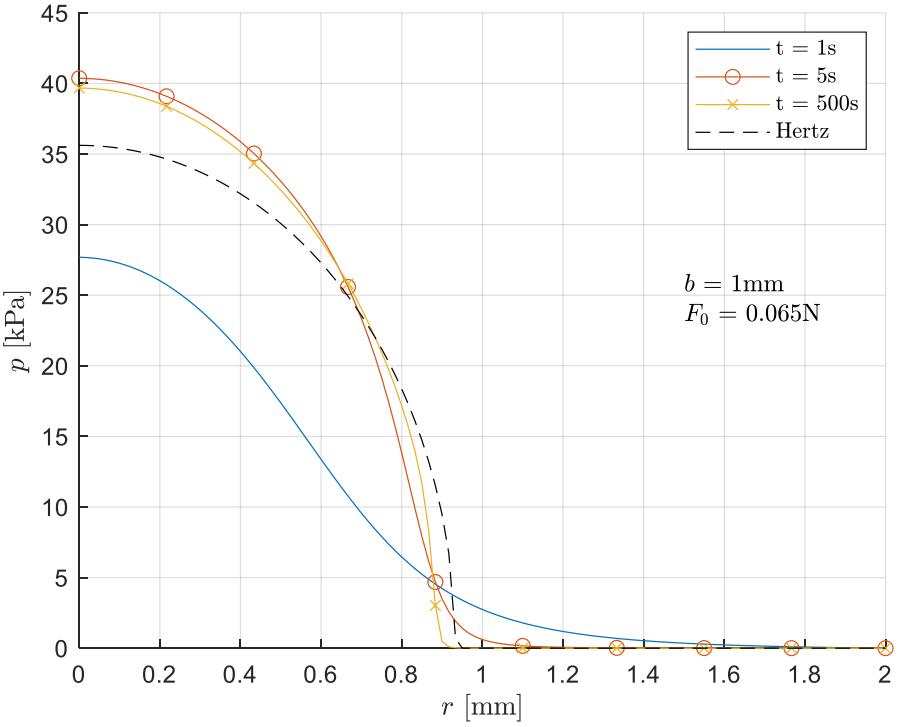

Figure 4.13 Film pressure $p(r,t)$, 0.065N Load, 1mm Conway thin slab

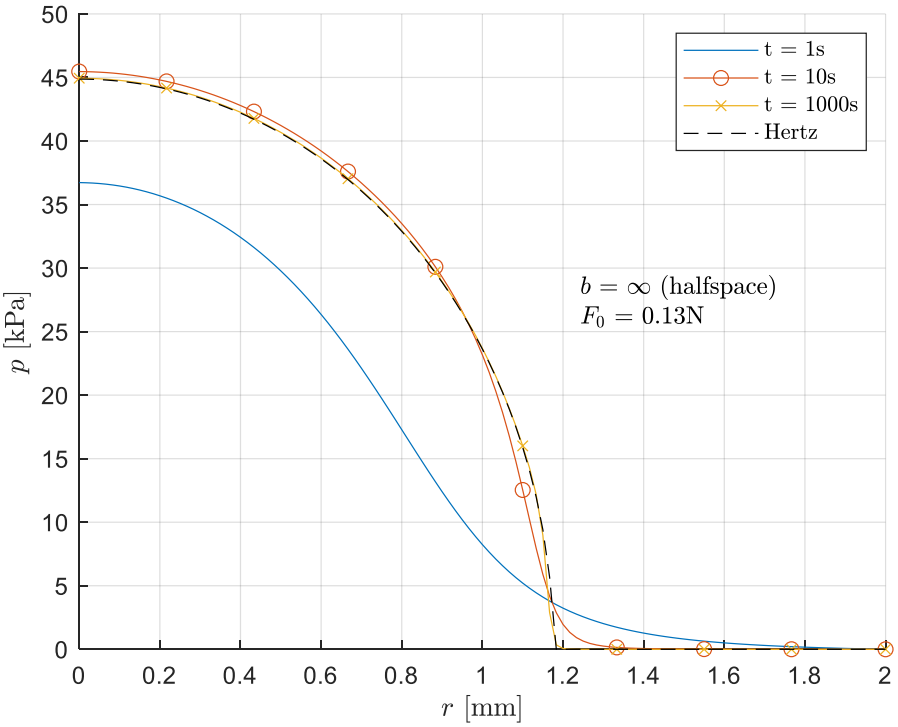

Figure 4.14 Film pressure $p(r,t)$, 0.13N Load, elastic halfspace

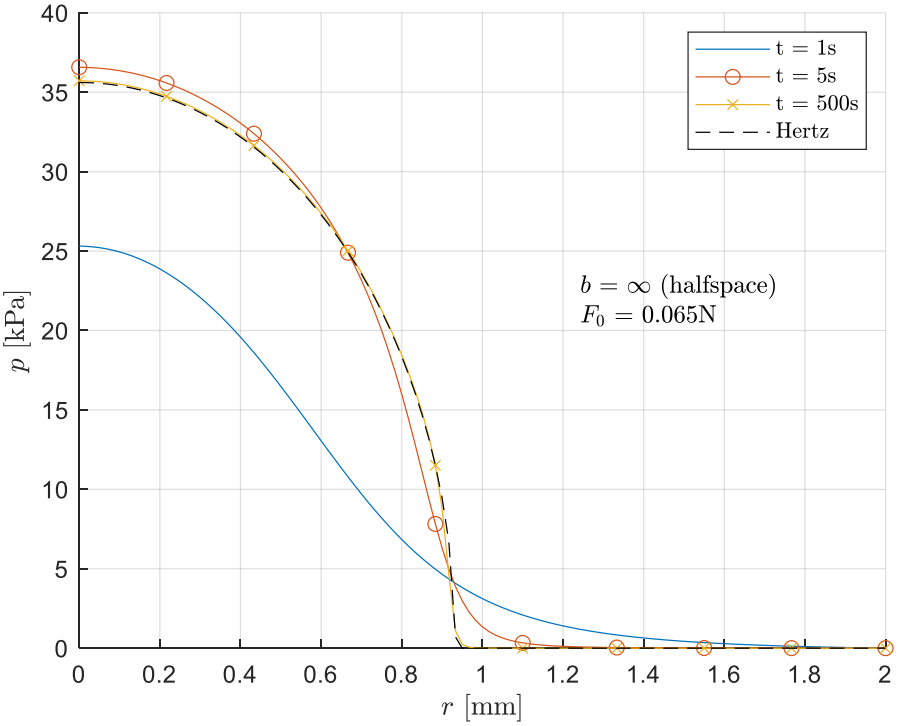

Figure 4.15 Film pressure $p(r,t)$, 0.065N Load, elastic halfspace

Figures 4.16 - 4.21 show the surface deflection of the elastic layer at three specified times in the squeeze film. The time steps are chosen to show the rapid development of the full deformation of the layer and to match the time steps of the film pressure profiles shown above. Figures 4.16 - 4.19 show the surface deflection for a slab with finite thickness, along with the associated Hertzian surface deflection. As expected, the deflections in the slab are smaller than for an elastic halfspace under dry contact, but the shape of the curves do agree well, despite being offset. Figures 4.20 and 4.21 show the surface deflections for an elastic halfspace, and these deflections are nearly identical to the associated Hertzian deformations, as would be expected since the pressure profiles matched Hertzian distributions (Figures 4.14 and 4.15). Interestingly, although the 6mm Conway slab and elastic halfspace produce graphically identical results for film thickness and pressure, the deflections in the thin slab are noticeably smaller (roughly 10% smaller peak deflection). This is curious since the smaller surface deflections might suggest a thinner fluid film for the thin slab, but this appears not to be the case, at least for the 0.13N loaded case, as seen from Figures 4.6 and 4.7.

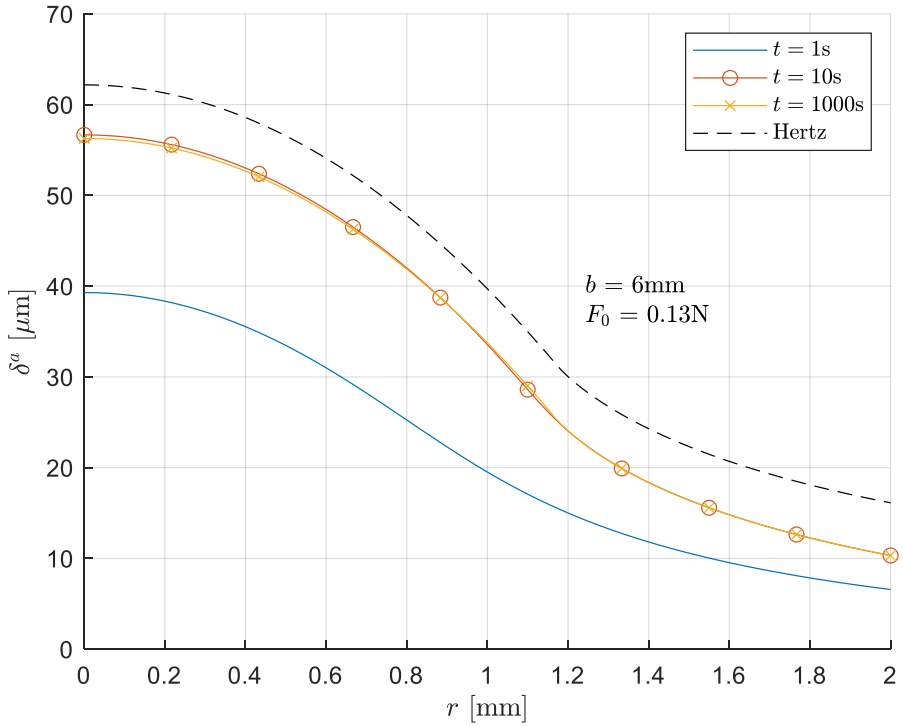

Figure 4.16 Elastic layer deflection $\delta^a(r,t)$, 0.13N Load, 6mm Conway thin slab

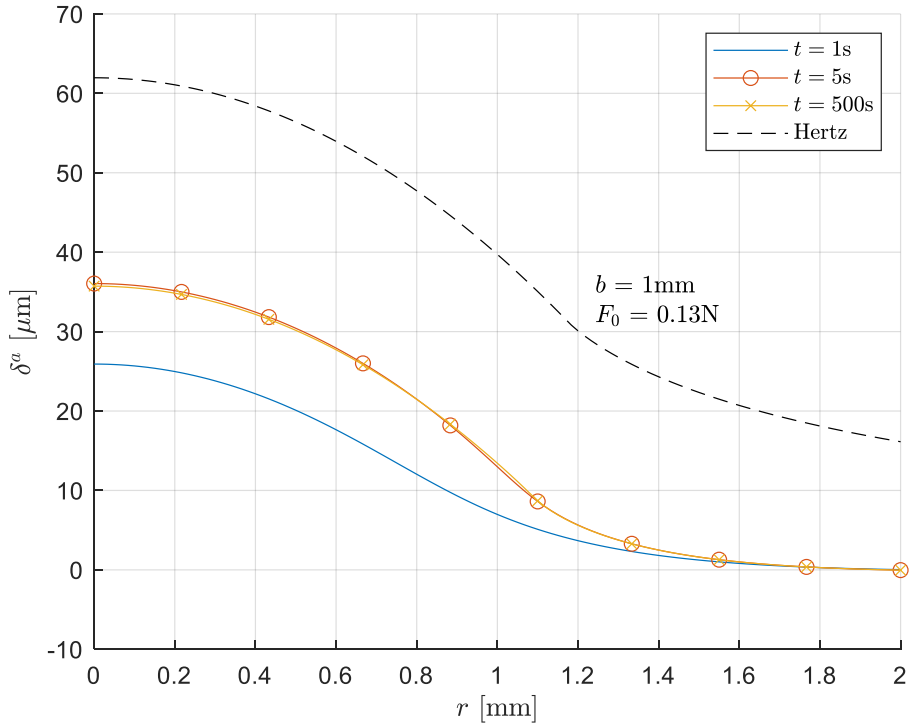

Figure 4.17 Elastic layer deflection $\delta^a(r,t)$, 0.13N Load, 1mm Conway thin slab

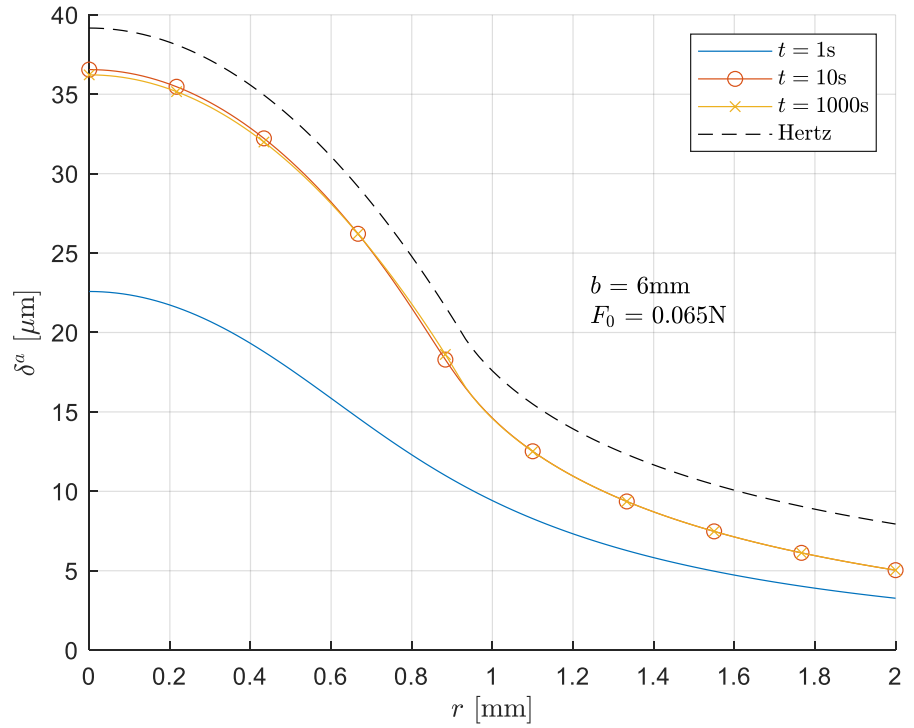

Figure 4.18 Elastic layer deflection $\delta^a(r,t)$, 0.065N Load, 6mm Conway thin slab

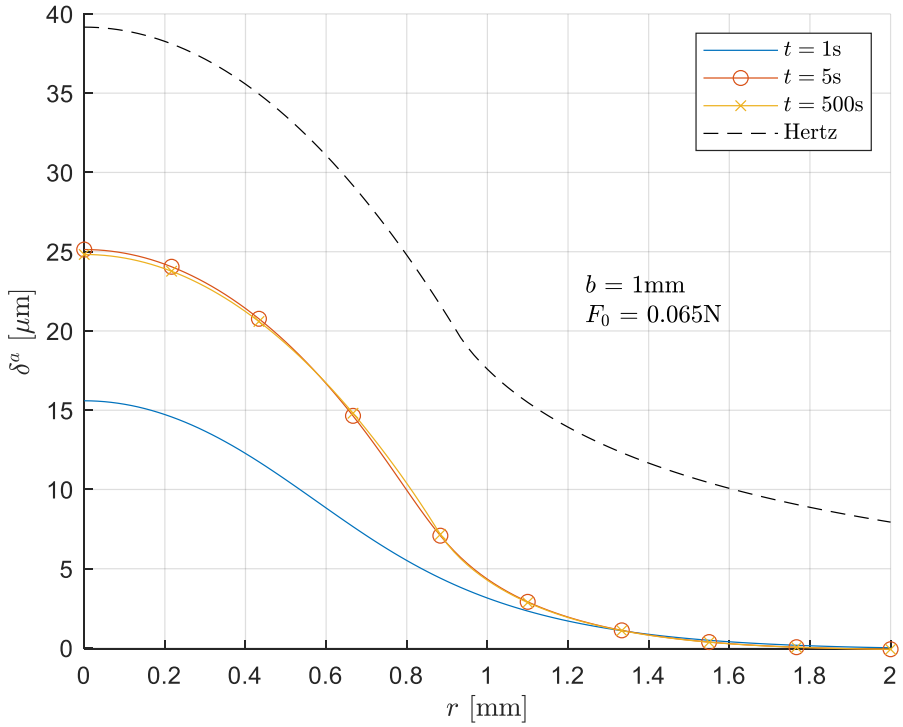

Figure 4.19 Elastic layer deflection $\delta^a(r,t)$, 0.065N Load, 1mm Conway thin slab

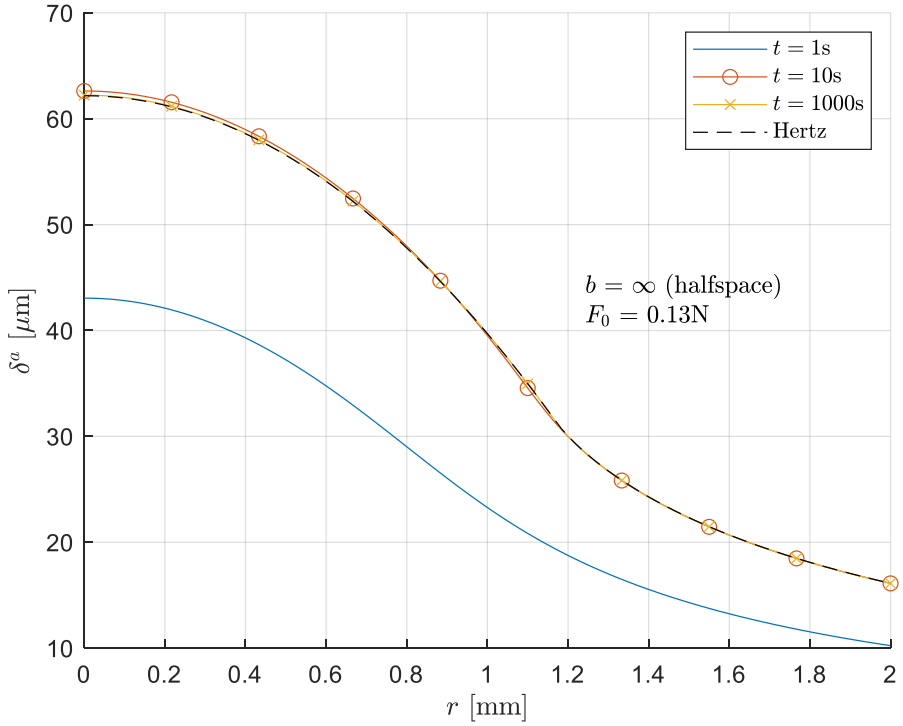

Figure 4.20 Elastic layer deflection $\delta^a(r,t)$, 0.13N Load, elastic halfspace

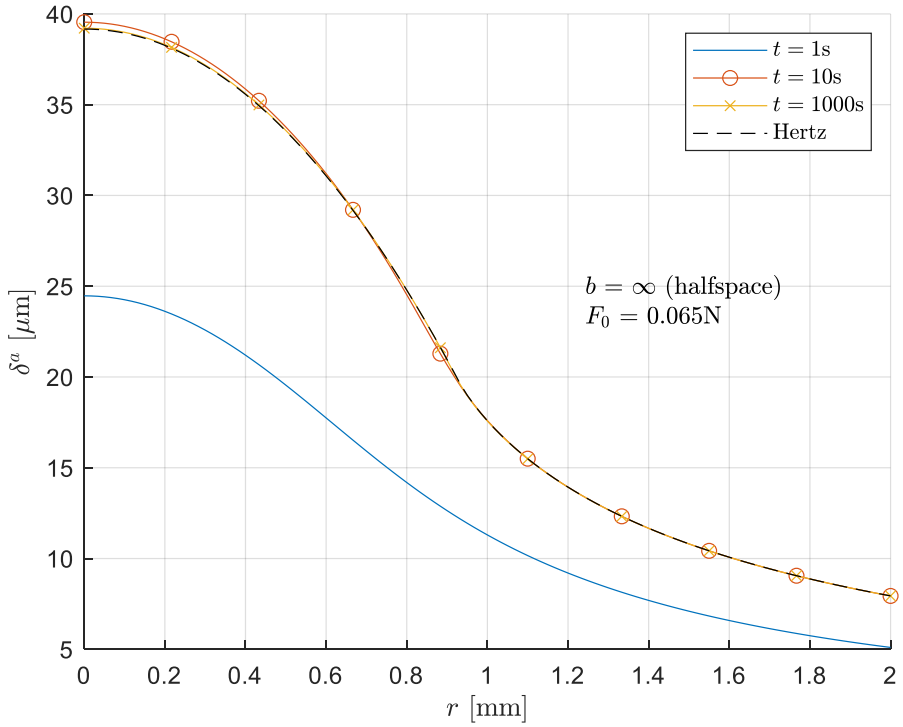

Figure 4.21 Elastic layer deflection $\delta^a(r,t)$, 0.065N Load, elastic halfspace

4.3 Comparison with Experimental Results with Rigid Support

Gaman et al. also provide experimental data for cases with nominally rigid surfaces. In these experiments, the lubricant film was situated between the steel ball and the glass, with the elastomer layer removed.

Boedo and Booker [21] provide an analytical solution for the case of a squeeze-film developed between a rigid flat surface and a rigid paraboloid indenter. However, Bair and Habchi [26] note that under certain conditions, nominally rigid EHD data actually contains effects from the elastic compliance of the approaching surfaces. This justifies using the current NIH formulation to simulate these experiments by representing the glass as an elastic structure. Bair and Habchi provide typical values for the elastic modulus and Poisson ratio of glass used in EHD testing equipment, given below in Table 4.2 with other experimental parameters. Central film thickness results from both the fully rigid formulation and the NIH halfspace formulation are compared with experimental data below in Figures 4.22 - 4.25.

Figures 4.22 and 4.23 show that the simulations using both the fully rigid formulation [21] and the NIH elastic formulation match the rigid body prediction given by Gaman:

$$\frac{h}{h_0} = exp\left(-\frac{\kappa^2 F_0 t}{6\pi\mu}\right) \tag{4.1}$$

Table 4.2 Dimensional specifications for experiments without elastomer layer

E	81	GPa	Young's modulus of glass* [26]
ν	0.208	-	Poisson ratio of glass* [26]
μ	0.5	Pa-s	Lubricant viscosity
κ	1/300, 1/22.5	1/mm	Indenter curvature
F_0	60, 0.13	N	External load
p_{atm}	0	Pa	Atmospheric pressure
h_0	250	μm	Initial central film thickness
α	10^4	1/s	Load rate parameter*

* Parameters only applicable to NIH simulation, not fully rigid simulation

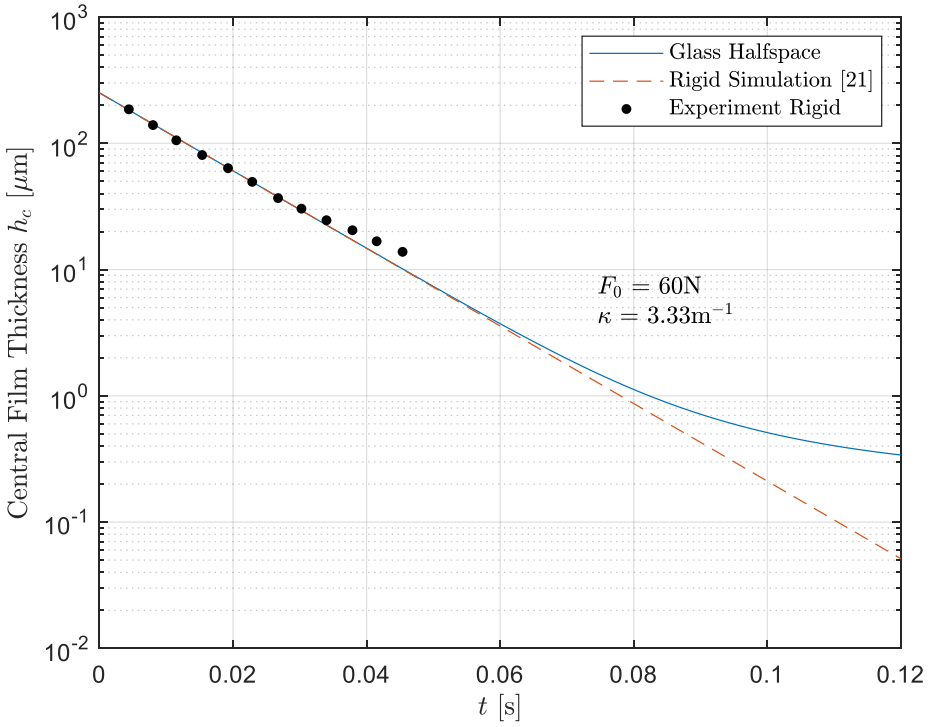

Figure 4.22 Early stage of approach of a steel ball onto glass (modeled as an elastic halfspace)

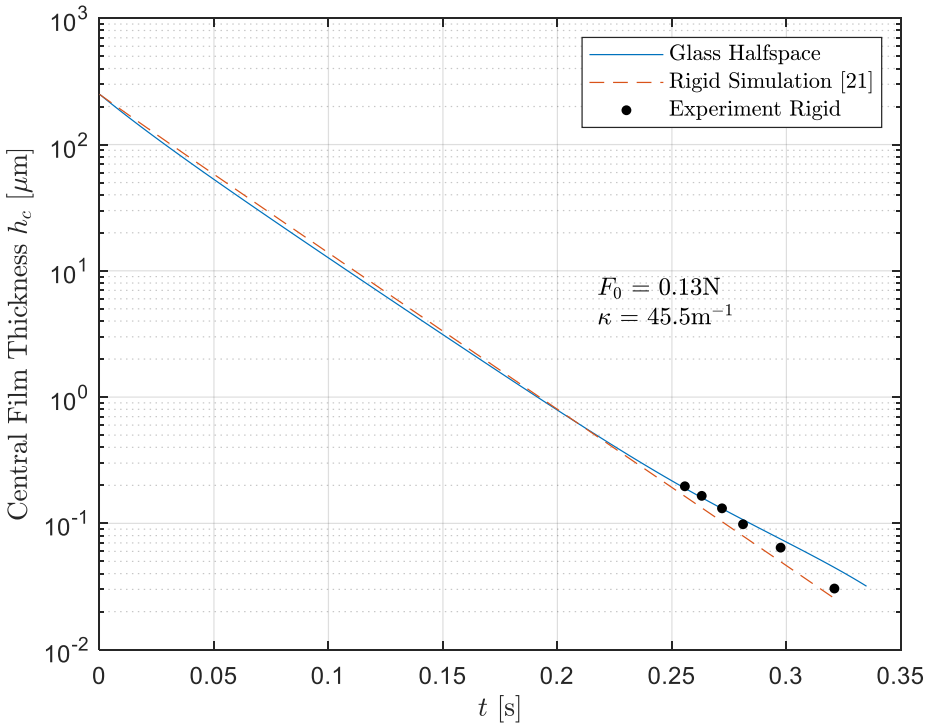

Figure 4.23 Closing stage of approach of a steel ball onto glass (modeled as an elastic halfspace)

Figure 4.24 shows the simulation of the 5mm elastic layer loaded with 60N with comparison to the rigid surface case, and there is actually an increase in film thickness at the very start. The likely cause of this is the overprediction of the elastic layer deflection due to the heavy loading. For this case, the dry contact depth is approximately 0.487mm, which is equivalent to a strain of 9.7%. This is a very large strain, and it is likely that the linear elasticity of the compliance matrix generation process is unsuitable for the large strains caused by such a heavy loading. As seen from previous cases, the elastic layer achieves its full deformation almost immediately as the full load is applied. Since these deflections are so large, and the indenter has not yet had time to close the gap, the film thickness increases. However, this result clearly does not align with the experimental evidence. A heavily loaded case like this likely exceeds the assumptions of small deformations and strains imposed by linear elasticity, so resort to nonlinear elasticity formulations is likely necessary. The initial growth in film thickness would necessitate an appropriate model of cavitation to ensure lubricant is actually able to flow into and fill the additional volume as the surfaces separate or to modify the film pressure accordingly if cavitation is present.

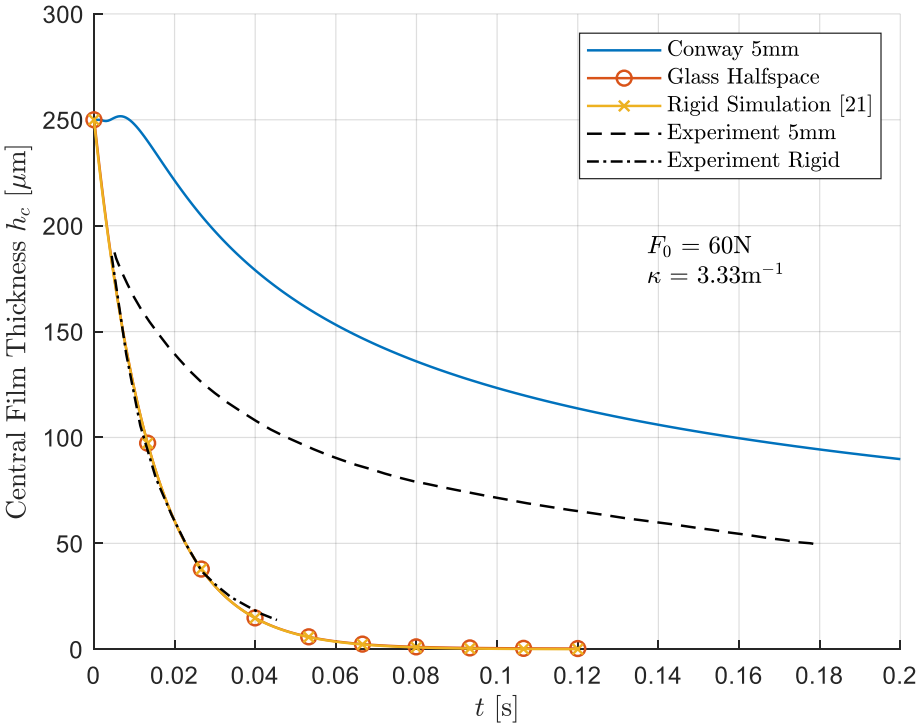

Figure 4.24 Early stages of approach: comparison of rigid and 5mm elastomer layer cases

Figure 4.25 shows simulated results for the closing stage of approach in the squeeze film. The rigid case shows extremely good agreement with the data. The 1mm elastic layer case was simulated using the current NIH formulation. The slope of the simulated result agrees extremely well with the data but is vertically offset. This may be due to some discrepancy in the value of the initial clearance, which is used to scale the central film thickness for plotting. There is some ambiguity in the initial clearance used for the experimental cases with the elastomer layer since Gaman does not explicitly state it. The results below for the 1mm elastic layer were scaled using $h_0 = 1.25$ mm.

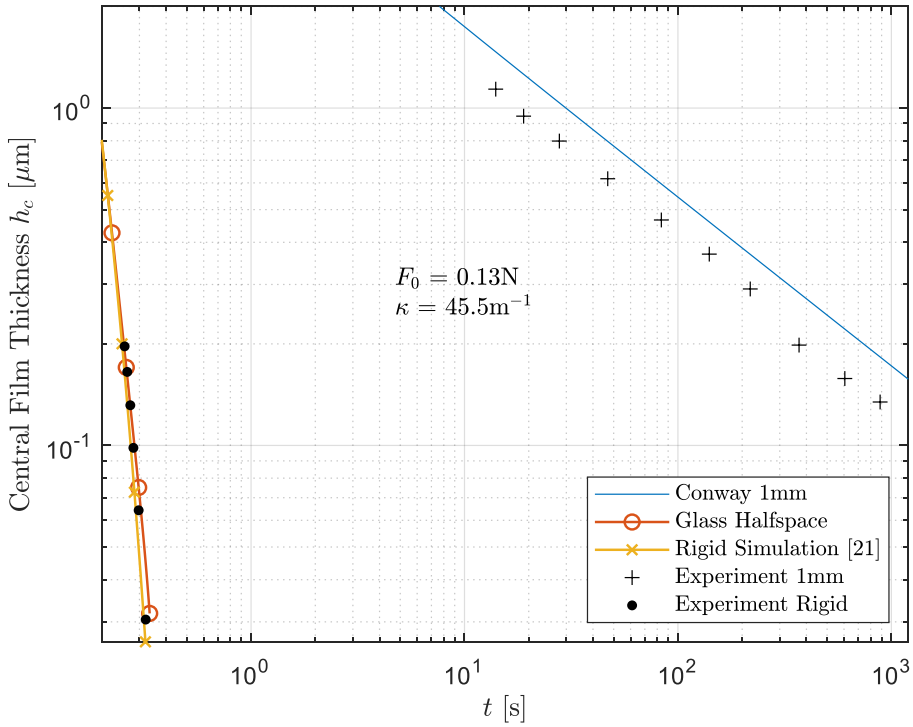

Figure 4.25 Closing stages of approach: comparison of rigid and soft 1mm elastomer layer cases

4.4 Displacement and Stresses in the Elastomer Layer

Figures 4.26 and 4.27 below show the stresses, strains, and vertical displacement along the z-axis of the elastic halfspace simulated for the experimental cases given. Since the vertical displacement of the thin elastomer layer must be zero, the theoretical displacement of the halfspace model gives some indication of how well the model matches the experimental apparatus. The elastic strains have peak values of approximately 2%, which can be considered to be in the linearly elastic range for typical elastomers. Under both loads, the stresses and displacements have their peak values at the surface, but rapidly decay in the top 2-3mm of the halfspace. From that point onward, the stresses and displacements continue to decay to zero (as required by the implicit boundary conditions at infinity), albeit much more slowly. This gives an explanation why the elastic halfspace does not provide a good approximation for the 1mm elastic layers: The displacements in the halfspace are still a large fraction of the surface displacements at a depth of 1mm. Conversely, the displacements in the halfspace at a depth of 6mm are significantly smaller than the surface displacements, which provides an adequate approximation of the 6mm elastic layer, as evidenced by the EHL results given above.

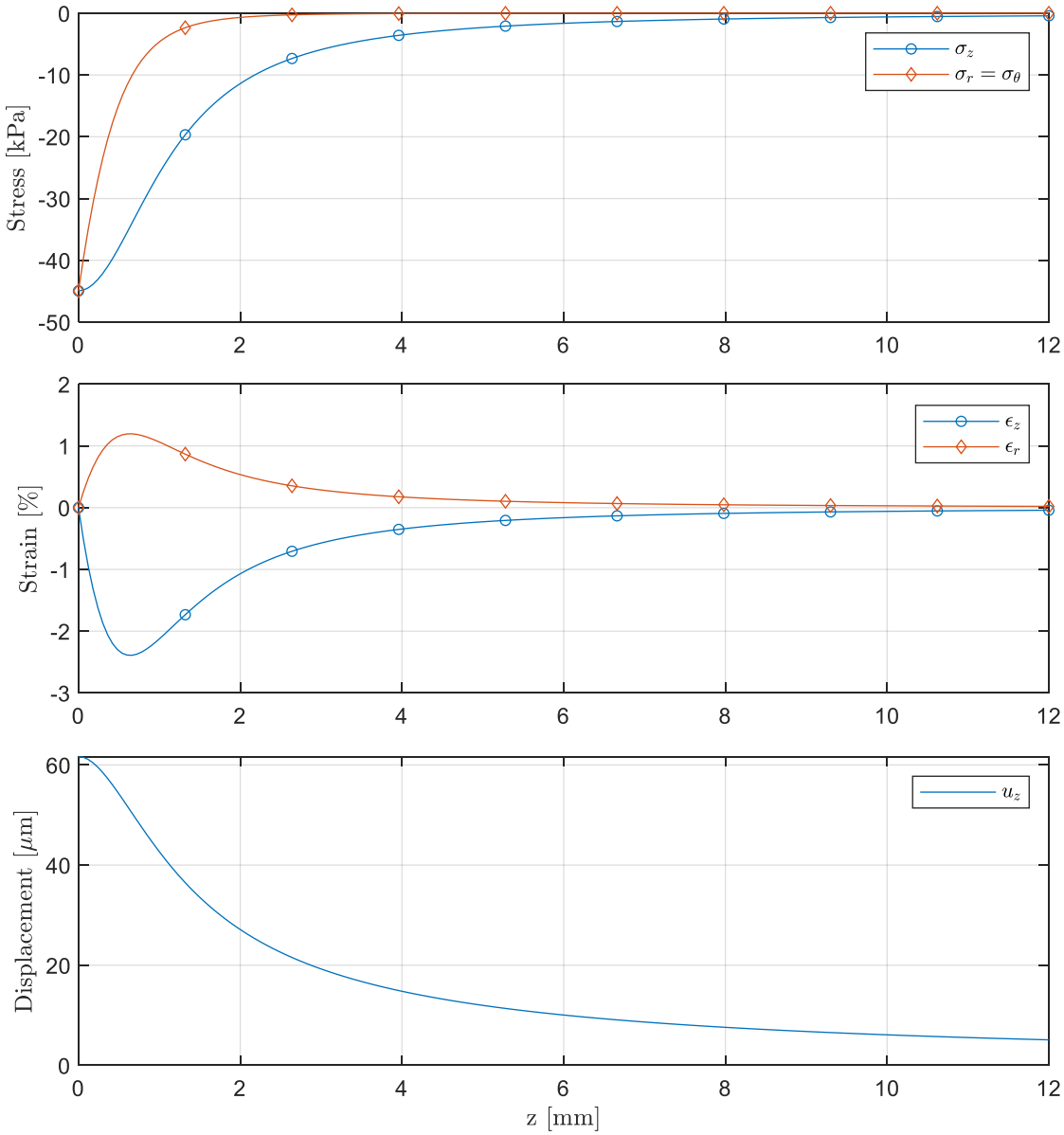

Figure 4.26 Stresses and displacements along z-axis in elastic halfspace for 0.13N case

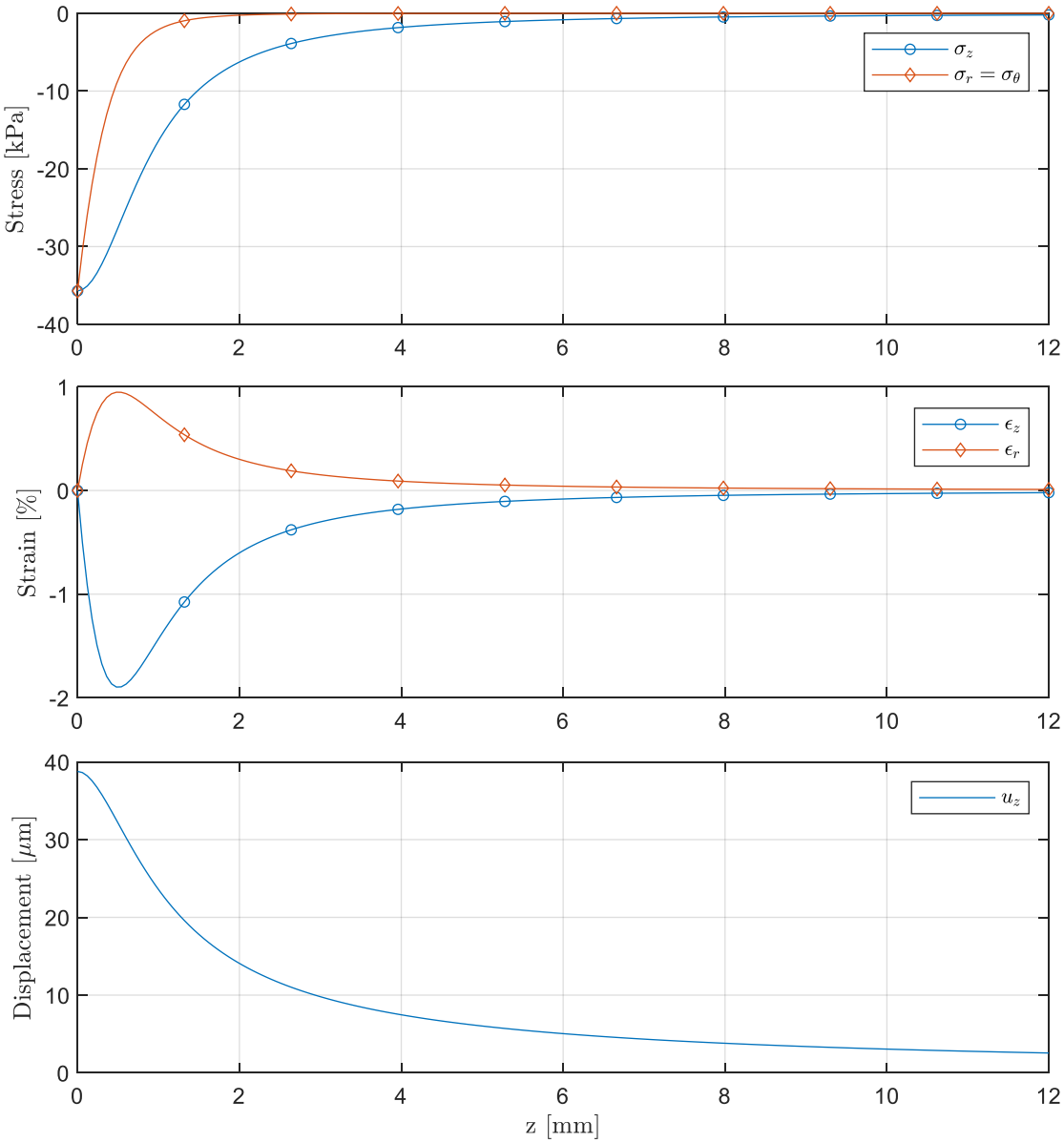

Figure 4.27 Stresses and displacements along z-axis in elastic halfspace for 0.065N case

Chapter 5

Non-Dimensional Problem Formulation

To assist in creating design charts useful for the practicing engineer, it is helpful to develop nondimensional parameters that characterize the system behavior. Since this EHL problem exhibits vastly different behavior for a conical indenter than for a parabolic indenter and the indenters are characterized differently, it is more convenient to scale these problems separately than to try to find a common parameterization.

5.1 Non-Dimensional Parameters: Paraboloid Indenter

The following scaled values can be used to nondimensionalize the Reynolds equation, the equations governing the boundary conditions, the load rate, and the surface deflection of the elastic layer:

$$\bar{r} = \frac{r}{R} \qquad \bar{h} = \frac{h}{\kappa R^2} \qquad \epsilon = \frac{e}{\kappa R^2} \qquad \bar{p} = \frac{\pi R^2}{F_0} p \qquad \tau = \frac{\kappa^2 F_0}{\mu} t$$

When these equations are scaled in this manner, the dimensionless groups given in Table 5.1 appear as parameters in the dimensionless equations.

Table 5.1 Dimensionless parameters for paraboloid indenter

Symbol	Group	Name
$\bar{h}_0$	$\frac{h_0}{\kappa R^2}$	Initial clearance parameter
$\bar{E}$	$\frac{\kappa R^3 E}{F_0(1-\nu^2)}$	Elasticity parameter
$\bar{\alpha}$	$\frac{\mu\alpha}{\kappa^2 F_0}$	Load rate parameter
$\bar{b}$	$\frac{b}{R}$	Layer thickness parameter

The nondimensional form of the Reynolds equation becomes

$$\frac{\partial}{\partial \bar{\mathrm{r}}}\left(\bar{\mathrm{r}}\bar{\mathrm{h}}^3\frac{\partial \bar{\mathrm{p}}}{\partial \bar{\mathrm{r}}}\right) = 12\pi\bar{\mathrm{r}}\frac{\partial \bar{\mathrm{h}}}{\partial \tau} \tag{5.1}$$

where film thickness is given by

$$\begin{aligned}\bar{\mathrm{h}}(\bar{\mathrm{r}},\tau) &= \frac{h_0}{\kappa R^2} + \frac{\bar{\mathrm{r}}^2}{2} + \frac{\delta^{\mathrm{a}}}{\kappa R^2} - \frac{\delta^{\mathrm{b}}}{\kappa R^2} \\ &= \frac{h_0}{\kappa R^2} + \frac{\bar{\mathrm{r}}^2}{2} + \frac{\delta^{\mathrm{a}}\left(\bar{\mathrm{r}},\tau;\frac{b}{R},\frac{\kappa R^3 E}{F_0(1-\nu^2)}\right)}{\kappa R^2} - \epsilon(\tau) \\ &= \bar{h}_0 + \frac{\bar{r}^2}{2} + \bar{\delta}^a\left(\bar{r},\tau;\bar{b},\bar{E}\right) - \epsilon(\tau)\end{aligned} \tag{5.2}$$

with the pressure boundary condition

$$\bar{\mathrm{p}}(\bar{\mathrm{r}}=1,\tau) = 0 \tag{5.3}$$

and initial conditions on the indenter position and film pressure are given by

$$\epsilon(\tau=0) = 0 \tag{5.4}$$

$$\bar{\mathrm{p}}(\bar{\mathrm{r}},\tau=0) = 0 \tag{5.5}$$

subject to the force balance constraint

$$2\int_0^1 \bar{\mathrm{p}}(\bar{\mathrm{r}},\tau)\bar{\mathrm{r}}\mathrm{d}\bar{\mathrm{r}} = 1-\exp\left[-\left(\frac{\mu\alpha}{\kappa^2 F_0}\right)^2\tau^2\right] = 1-\exp(-\bar{\alpha}^2\tau^2) \tag{5.6}$$

Elasticity Parameter

The elasticity parameter is of particular note because it can be manipulated to be given purely in terms of the indenter radius R and the dry contact radius a of the analogous Hertz contact problem (see section 2.3):

$$\bar{E} = \frac{3}{4}\left(\frac{R}{a}\right)^3 \tag{5.7}$$

Combining this expression with $\bar{b} = \frac{b}{R}$, an expression can be obtained for the ratio of the Hertz contact radius to the layer thickness:

$$\frac{a}{b} = \left(\frac{4}{3}\bar{E}\bar{b}^3\right)^{-1/3} \approx \frac{0.9086}{\bar{b}\bar{E}^{1/3}} \tag{5.8}$$

For large values of $\bar{b}$ and $\bar{E}$, $\frac{a}{b}$ is small, and the Hertz dry contact radius is a good approximation of the radius where the pressure under the lubricated indenter may be

expected to drop to zero. This means that the form of the elasticity parameter given above allows that radius to be conveniently estimated, even prior to simulation. However, as the value of $\bar{b}$ or $\bar{E}$ decreases, the Hertzian stress approximation will becomes significantly worse, as will be shown. The dependence on layer thickness is much greater than on any of the dimensional parameters in the elasticity parameter, as can be seen from the exponents.

5.2 Dynamic Similarity Example: Paraboloid Indenter

To ensure that this nondimensionalization is properly done, two simulations were run with different dimensional parameters but identical nondimensional parameters, shown in Table 5.2. Figures 5.1 - 5.4 show the nondimensional results for each dimensional case together. Figure 5.1 shows identical results for nondimensional central film thickness for the two cases. Similarly, the film thickness profile in Figure 5.2, film pressure profile in Figure 5.3, and elastic layer surface deflection profile in Figure 5.4 are all identical for the two cases. The profiles are taken at half of the final simulation time to help capture some of the transient nature of the squeeze film behavior.

Table 5.2 Dimensional and nondimensional specifications for paraboloid indenter dynamic similarity example

	Units	**Case 1**	**Case 2**
h_0	μm	400	640
κ	1/m	50	20
μ	Pa-s	0.5	0.25
F_0	N	0.1	0.5
α	1/s	1	1.6
E	MPa	1	1.8958
ν	-	0.5	0.3
b	mm	1	2
R	mm	2	4
$\bar{h}_0$		2	2
$\bar{E}$		5.3333	5.3333
$\bar{\alpha}$		0.002	0.002
$\bar{b}$		0.5	0.5
t_{final}	s	600	375
τ_{final}		3E+05	3E+05

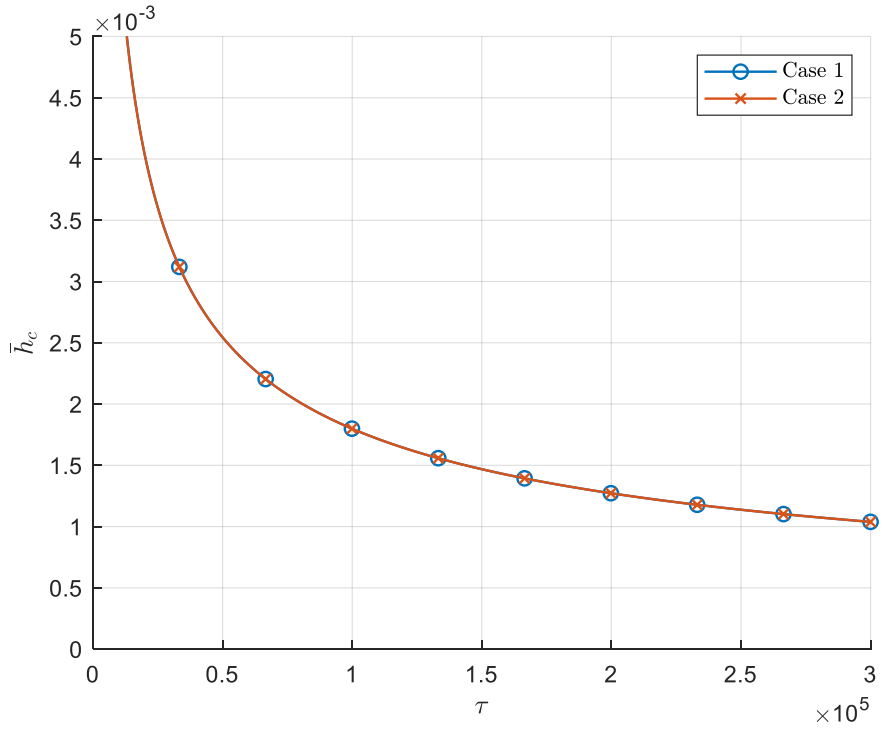

Figure 5.1 Comparison of nondimensional central film thickness for paraboloid dynamic similarity example

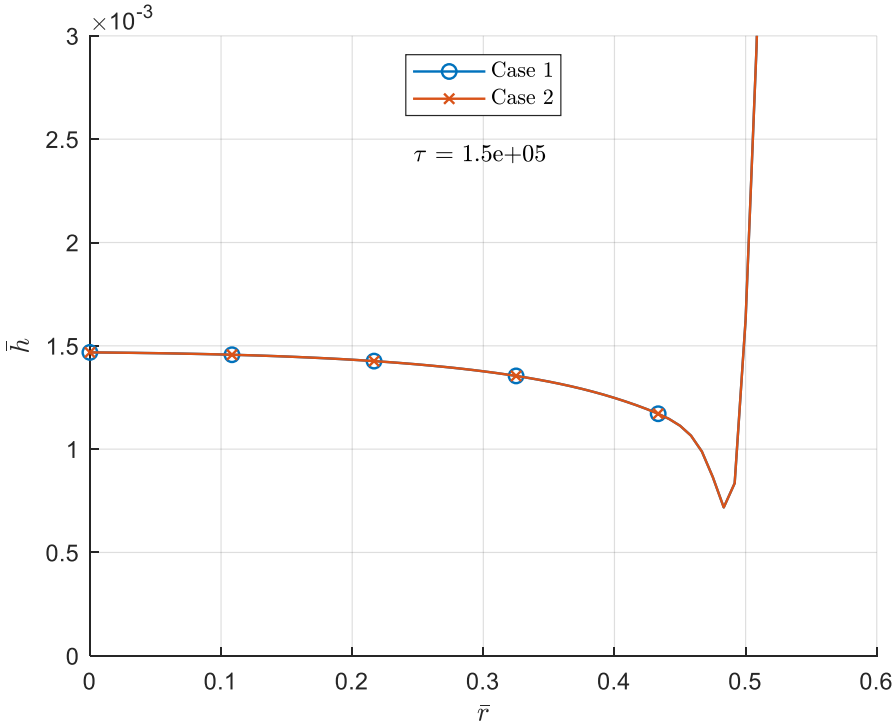

Figure 5.2 Comparison of nondimensional film thickness profile for paraboloid dynamic similarity example

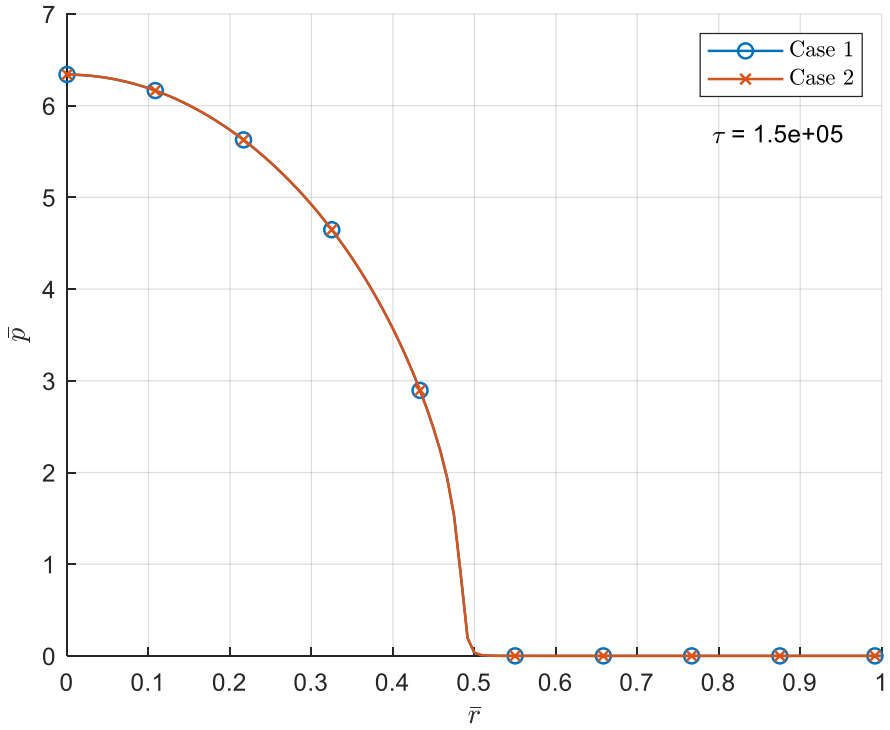

Figure 5.3 Comparison of nondimensional film pressure distribution for paraboloid dynamic similarity example

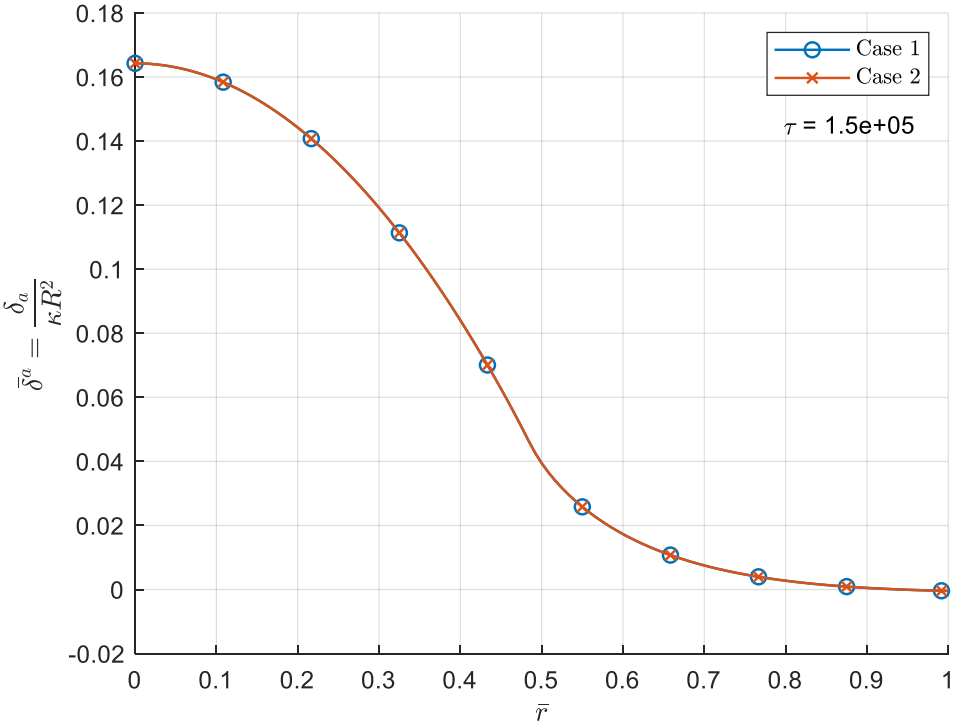

Figure 5.4 Comparison of nondimensional elastic layer deflection for paraboloid dynamic similarity example

5.3 Non-Dimensional Parameters: Conical Indenter

For the case of a conical indenter, the following scaled values nondimensionalize the governing equations of the system, which then contain the dimensionless parameters shown in Table 5.3:

$$\bar{r} = \frac{r}{R} \qquad \bar{\mathrm{h}} = \frac{\mathrm{h}}{\beta R} \qquad \epsilon = \frac{\mathrm{e}}{\beta R} \qquad \bar{\mathrm{p}} = \frac{\pi \mathrm{R}^2}{\mathrm{F}_0}\mathrm{p} \qquad \tau = \frac{\beta^2 \mathrm{F}_0}{\mathrm{R}^2 \mu}\mathrm{t}$$

Table 5.3 Dimensionless parameters for conical indenter

Symbol	Group	Name
$\bar{h}_0$	$\frac{h_0}{\beta R}$	Initial clearance parameter
$\bar{E}$	$\frac{\beta R^2 E}{F_0(1-\nu^2)}$	Elasticity parameter
$\bar{\alpha}$	$\frac{R^2 \mu \alpha}{\beta^2 F_0}$	Load rate parameter
$\bar{b}$	$\frac{b}{R}$	Layer thickness parameter

The nondimensional form of the Reynolds equation and the boundary/initial conditions are identical to the paraboloid indenter case given above. However, the equations for the film thickness and total load differ.

Film thickness is given by

$$\begin{aligned} \bar{\mathrm{h}}(\bar{\mathrm{r}}, \tau) &= \frac{h_0}{\beta R} + \bar{\mathrm{r}} + \frac{\delta^{\mathrm{a}}}{\beta R} - \frac{\delta^{\mathrm{b}}}{\beta R} \\ &= \bar{h}_0 + \bar{\mathrm{r}} + \frac{\delta^{\mathrm{a}}\left(\bar{\mathrm{r}}, \tau; \bar{b}, \bar{E}\right)}{\beta R} - \epsilon(\tau) \end{aligned} \tag{5.9}$$

subject to the constraint

$$2\int_0^1 \bar{\mathrm{p}}(\bar{\mathrm{r}}, \tau)\bar{\mathrm{r}}\mathrm{d}\bar{\mathrm{r}} = 1 - \exp\left[-\left(\frac{\mu\alpha R^2}{\beta^2 \mathrm{F}_0}\right)^2 \tau^2\right] = 1 - \exp(-\bar{\alpha}^2\tau^2) \tag{5.10}$$

To usefully scale the problem with a conical indenter, it is helpful to find the slope that "matches" the shape of paraboloid indenters used in experiments. As shown in Figure 5.5,

"matched" means that the indenter profiles curves overlap at $r = 0$ and $r = R$, whereupon the indenter curvature and indenter slope are related by

$$\beta = \frac{1}{2}\kappa R \tag{5.11}$$

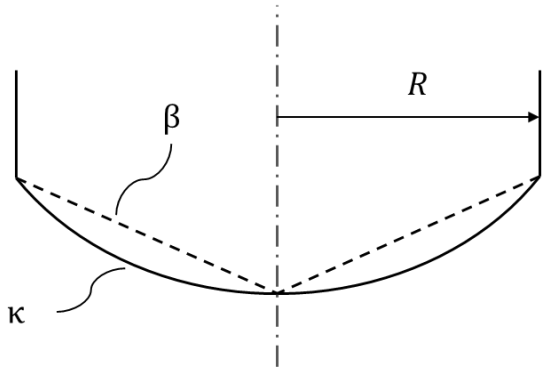

Figure 5.5 Schematic of "matched" paraboloid and conical indenter profiles

Elasticity Parameter

Similar to the paraboloid case, the elasticity parameter for the conical indenter case can be recast in terms of the contact radius of the analogous dry contact problem for an infinite halfspace (see section 2.4), namely,

$$\bar{E} = \frac{2}{\pi}\left(\frac{R}{a}\right)^2 \tag{5.12}$$

As before, using this expression for $\bar{E}$, an expression for $\frac{a}{b}$ can be given:

$$\frac{a}{b} = \left(\frac{\pi}{2}\bar{E}\bar{b}^2\right)^{-1/2} \approx \frac{0.7979}{\bar{b}\bar{E}^{1/2}}$$

5.4 Dynamic Similarity Example: Conical Indenter

Table 5.4 shows dimensional specifications for two cases of a conical indenter EHL problem, along with their corresponding nondimensional parameters, which are equivalent. Figures 5.6 - 5.9 show identical nondimensional results of these two simulations.

Table 5.4 Dimensional and nondimensional specifications for conical indenter dynamic similarity example

	Units	Case 1	Case 2
h_0	μm	100	60
β	-	0.01	0.003
μ	Pa-s	0.5	0.25
F_0	N	0.1	0.5
α	1/s	100	22.5
E	MPa	2	10.111
ν	-	0.5	0.3
b	mm	1	2
R	mm	2	4
$\bar{h}_0$		5	5
$\bar{E}$		1.0667	1.0667
$\bar{\alpha}$		20	20
$\bar{b}$		0.5	0.5
t_{final}	s	20	88.89
τ_{final}		100	100

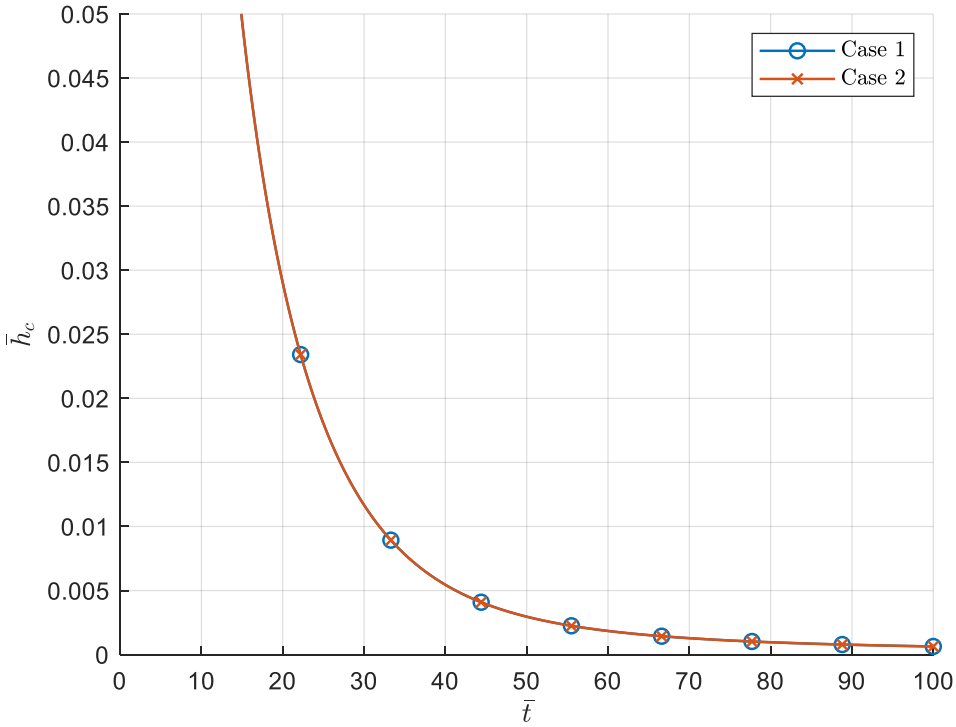

Figure 5.6 Comparison of nondimensional central film thickness for conical dynamic similarity example

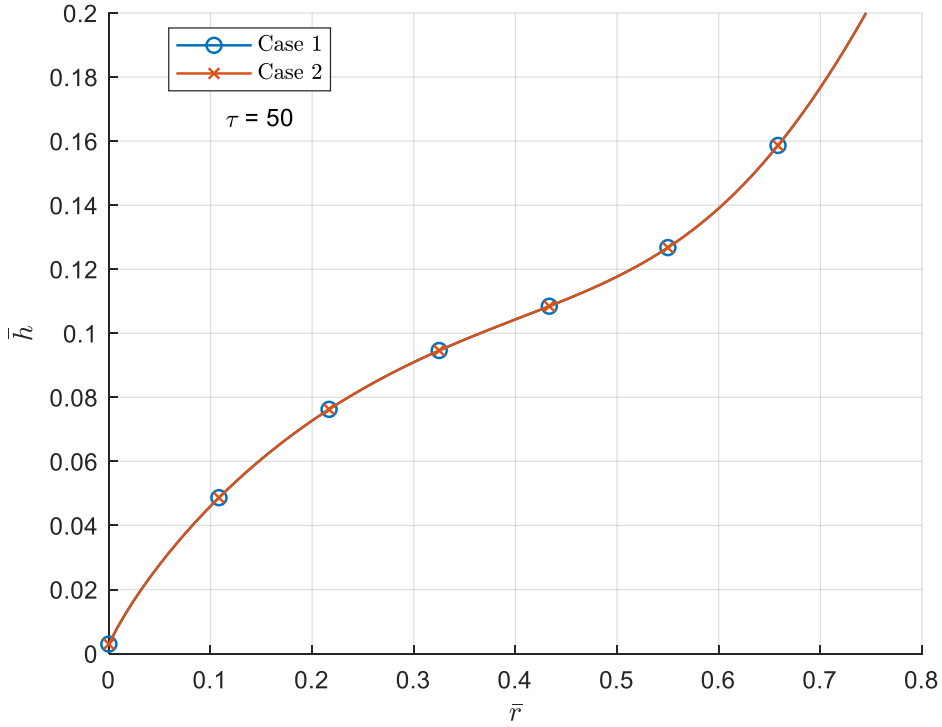

Figure 5.7 Comparison of nondimensional film thickness profile for conical dynamic similarity example

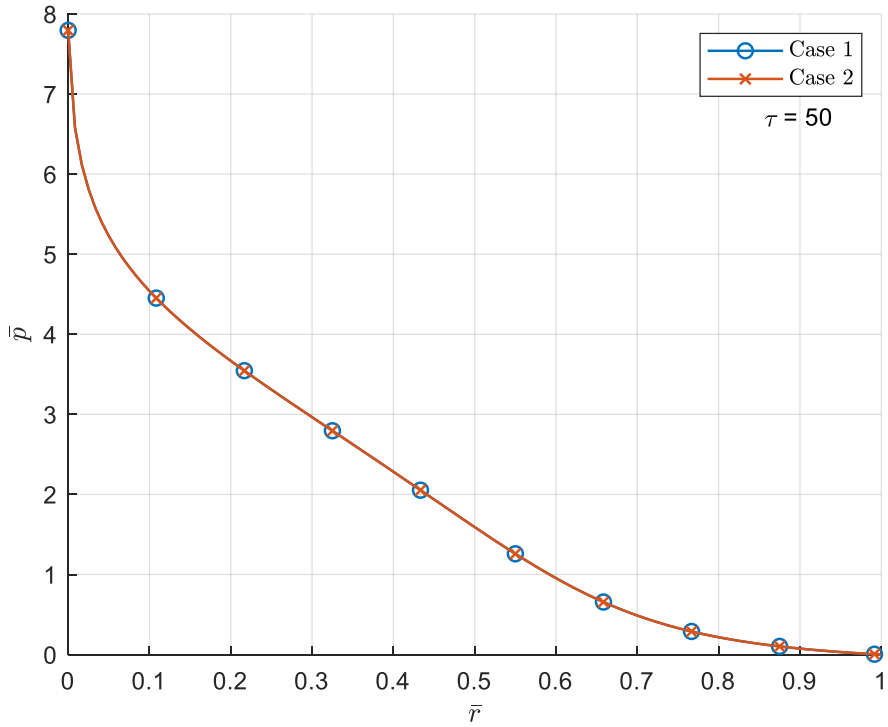

Figure 5.8 Comparison of nondimensional film pressure distribution for conical dynamic similarity example

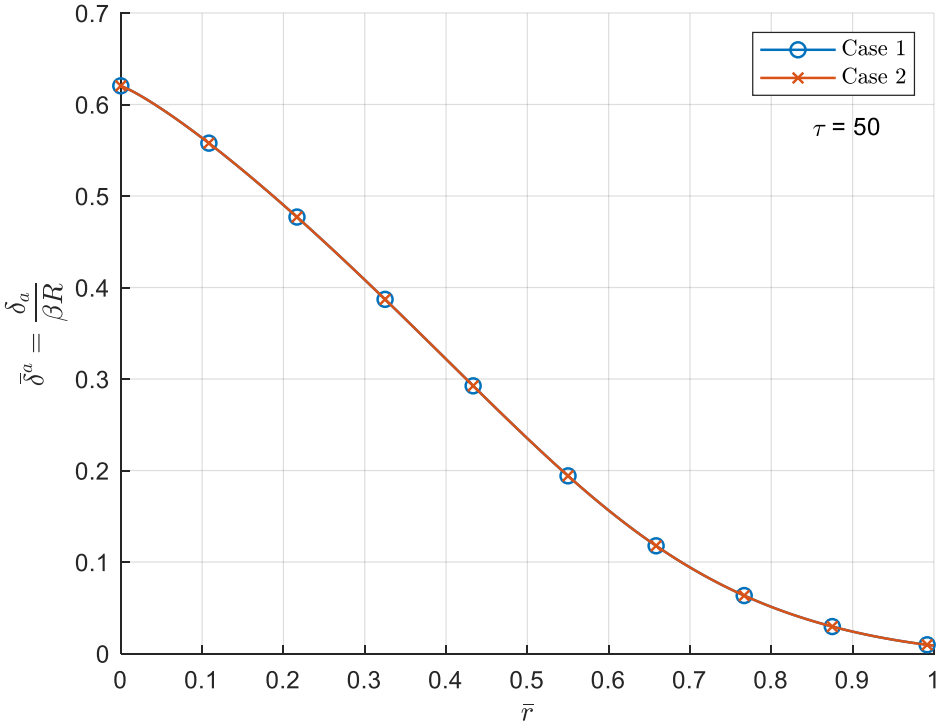

Figure 5.9 Comparison of nondimensional elastic layer surface deflection for conical dynamic similarity example

Chapter 6

Results and Discussion: Paraboloid Indenter

6.1 Initial Clearance Parameter Sweep

The results shown in Figures 6.1 - 6.8 are highly interesting, as they show that the time evolution of the system is extremely insensitive to the initial separation distance, even over a range of several orders of magnitude. The nondimensional parameters of the sweep are given in Table 6.1. Figures 6.1 and 6.2 show indistinguishable results for central film thickness and a film thickness profile taken at 10% of the simulated time to closure. Figures 6.3 - 6.5 show similarly indistinguishable results for film pressure, elastic layer surface deflection, and minimum film thickness.

Figures 6.6 and 6.7 show the central film thickness and a film thickness profile at a very early stage to highlight just how quickly the four cases converge. Only the case of the smallest initial clearance lies apart from the other curves, and only marginally at that, within the first 1% of the total simulated time to closure. Regardless of the initial clearance, the indenter appears to "crash down" from its initial position until the film thicknesses grow small enough to develop significant pressures and carry the applied. This is in contrast to the situation of a completely rigid indenter and rigid surface, which depends heavily upon, and hence can be usefully scaled by, the initial clearance. However, since the situation with a highly compliant support is insensitive to the initial clearance, it is more useful to select another characteristic length to scale the problem, as done here.

This behavior also help explain why the case of the smallest initial clearance takes the longest to converge with the other curves. Since the film is already near the thicknesses where load-carrying pressures develop, the indenter settles more gently than the "crashing" observed in the cases of larger initial clearances.

Gaman et al. [5] comment on the insensitivity to initial clearance in experiments with an elastomer layer, noting that plotting h/h_0 against nondimensionalized time on log-log scale produced curves with practically identical slopes, but out of alignment. The data appeared to follow a power law: $h \propto t^{-1/2}$. Figure 6.8 repeats the results of Figure 6.1 on a log-log plot and shows that these simulations follow that same trend.

Table 6.1 Nondimensional parameters for initial clearance sweeps

Sweep	$\bar{\alpha}$	$\bar{b}$	$\bar{E}$	$\bar{h}_0$
1	0.1	1	1	0.1, 1, 10, 100

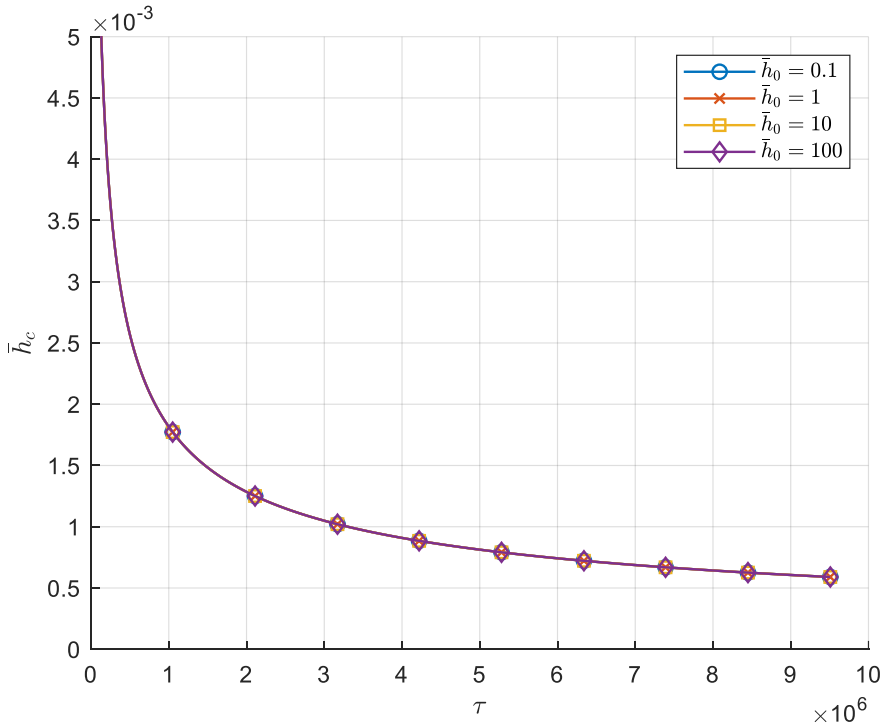

Figure 6.1 Initial Clearance Sweep 1: $\bar{\alpha} = 0.1, \bar{E} = 1, \bar{b} = 1$; Central film thickness time histories

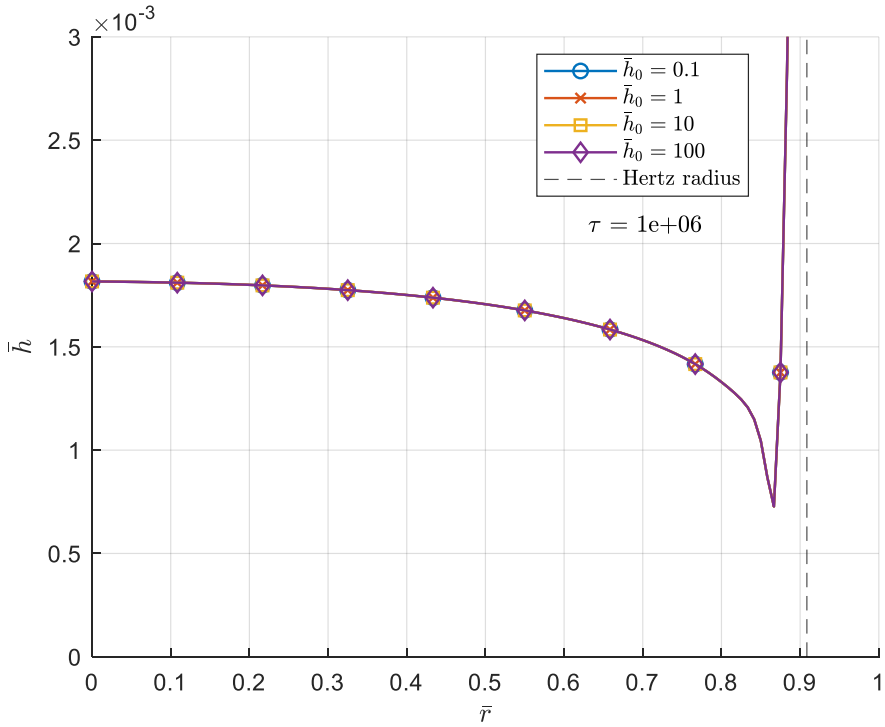

Figure 6.2 Initial Clearance Sweep 1: $\bar{\alpha} = 0.1, \bar{E} = 1, \bar{b} = 1$; Film thickness profiles; $\tau = 10^6$

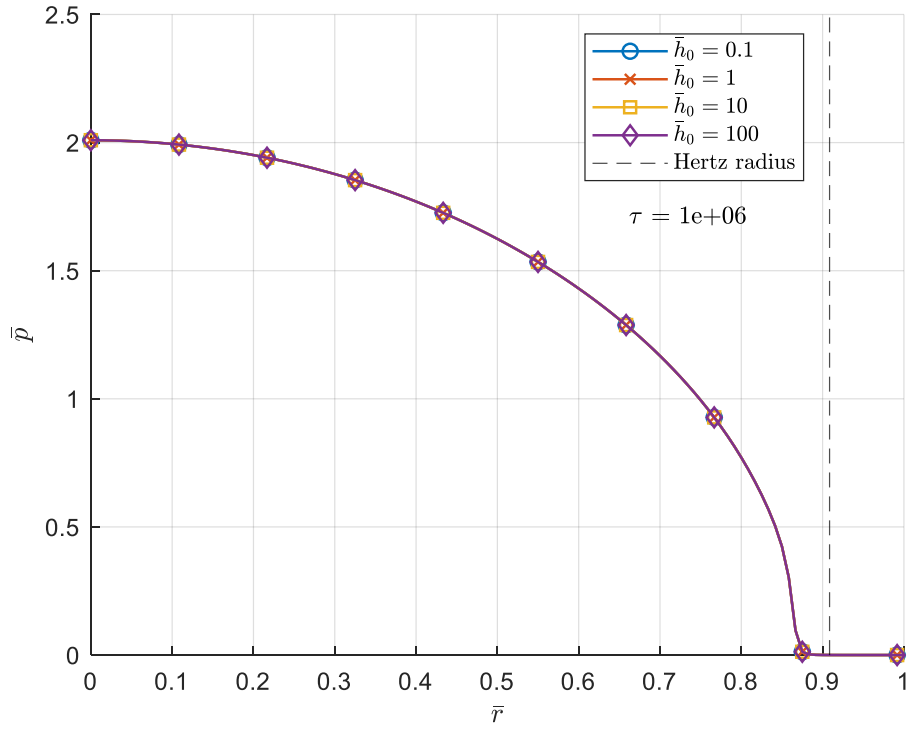

Figure 6.3 Initial Clearance Sweep 1: $\bar{\alpha} = 0.1, \bar{E} = 1, \bar{b} = 1$; Film pressure profiles; $\tau = 10^6$

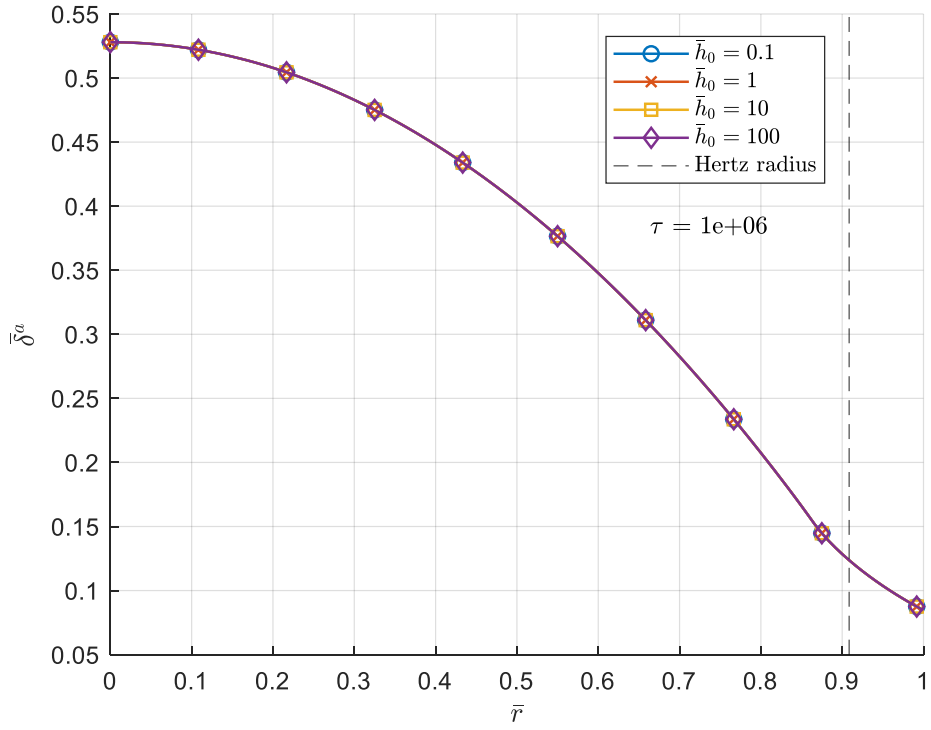

Figure 6.4 Initial Clearance Sweep 1: $\bar{\alpha} = 0.1, \bar{E} = 1, \bar{b} = 1$; Elastic layer surface deflection profiles; $\tau = 10^6$

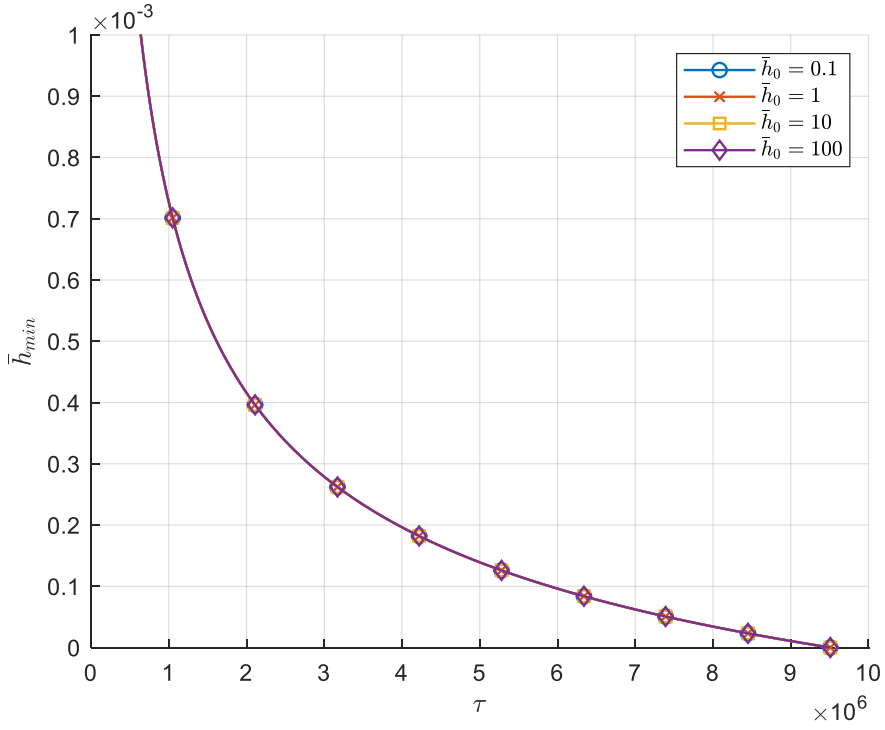

Figure 6.5 Initial Clearance Sweep 1: $\bar{\alpha} = 0.1, \bar{E} = 1, \bar{b} = 1$; Minimum film thickness time histories

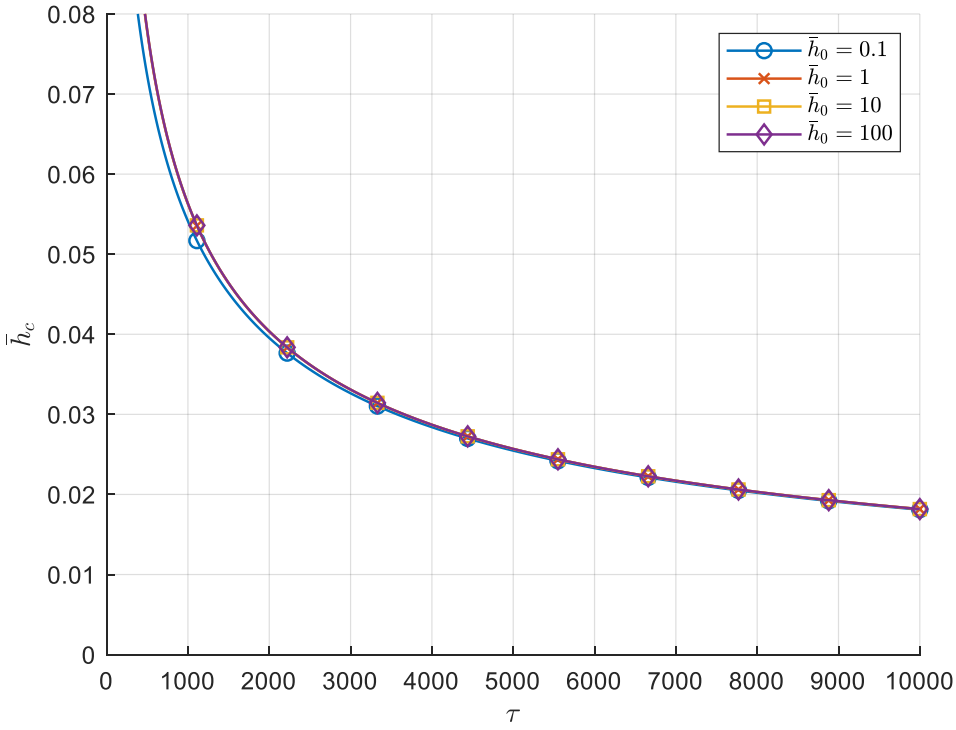

Figure 6.6 Initial Clearance Sweep 1: $\bar{\alpha} = 0.1, \bar{E} = 1, \bar{b} = 1$; Central film thickness time histories, early stages

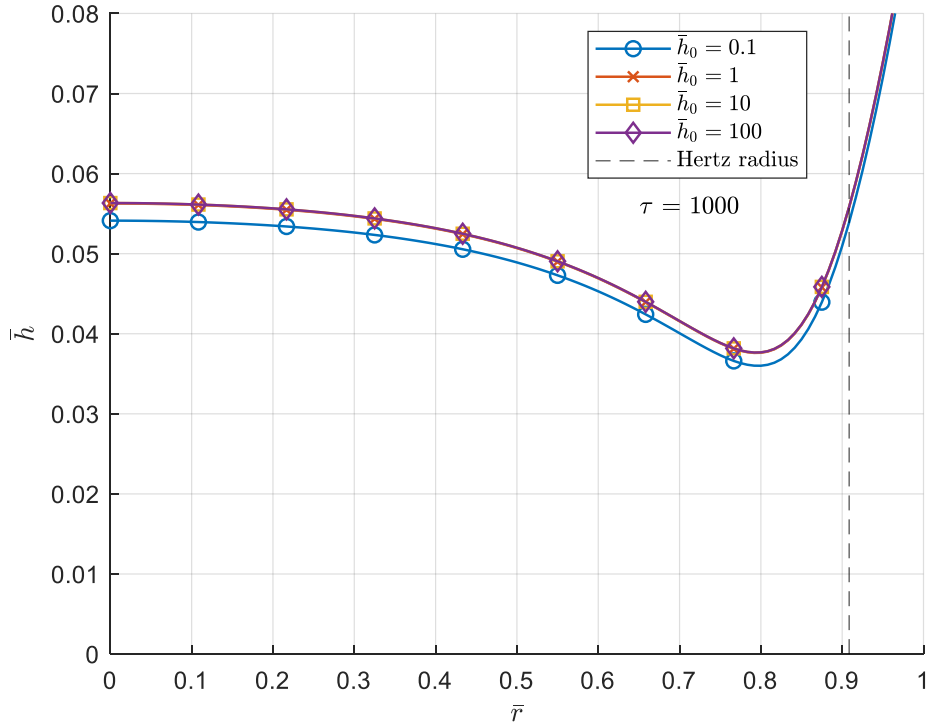

Figure 6.7 Initial Clearance Sweep 1: $\bar{\alpha} = 0.1, \bar{E} = 1, \bar{b} = 1$; Film thickness profiles; $\tau = 1000$

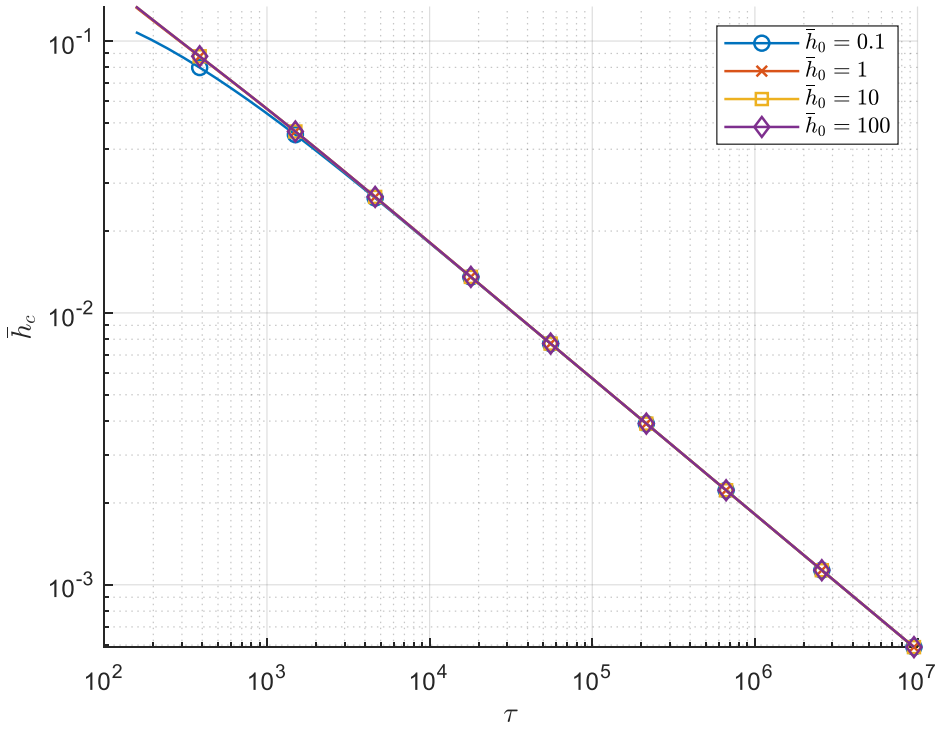

Figure 6.8 Initial Clearance Sweep 1: $\bar{\alpha} = 0.1, \bar{E} = 1, \bar{b} = 1$; Central film thickness time histories, Log-Log scale

6.2 Load Rate Parameter Sweep

The external load is nominally a step function. However, since this is computationally problematic, a ramped step with a tunable load rate parameter $\bar{\alpha}$ is used. By varying this load rate, we can observe how short the ramp time needs to be to approximate a real step. One measure of this would be to decrease the ramp time (increase the load rate parameter) until any further decrease does not produce different results. Figure 6.9 shows the applied load time histories for a range of values of $\bar{\alpha}$.

Figures 6.10 - 6.15 show the results of one sweep of the nondimensional load rate parameter. The values of $\bar{\alpha}$ span four orders of magnitude, shown in Table 6.2, to demonstrate the insensitivity of the system to variations in the load rate. Figures 6.10, 6.11, and 6.12 show essentially identical results for central film thickness, as well as film thickness and pressure profiles taken at $\tau = 10^4$. Only by zooming in on the early stages can some variation in central and minimum film thickness be seen in Figures 6.14 and 6.15, respectively. However, the curves converge quickly compared to the long period of relatively steady state central film thickness.

Table 6.2 Nondimensional parameters for load rate sweeps

Sweep	$\bar{h}_0$	$\bar{b}$	$\bar{E}$	$\bar{\alpha}$
1	1	1	1	10^{-3}, 10^{-2}, 10^{-1}, 1, 10

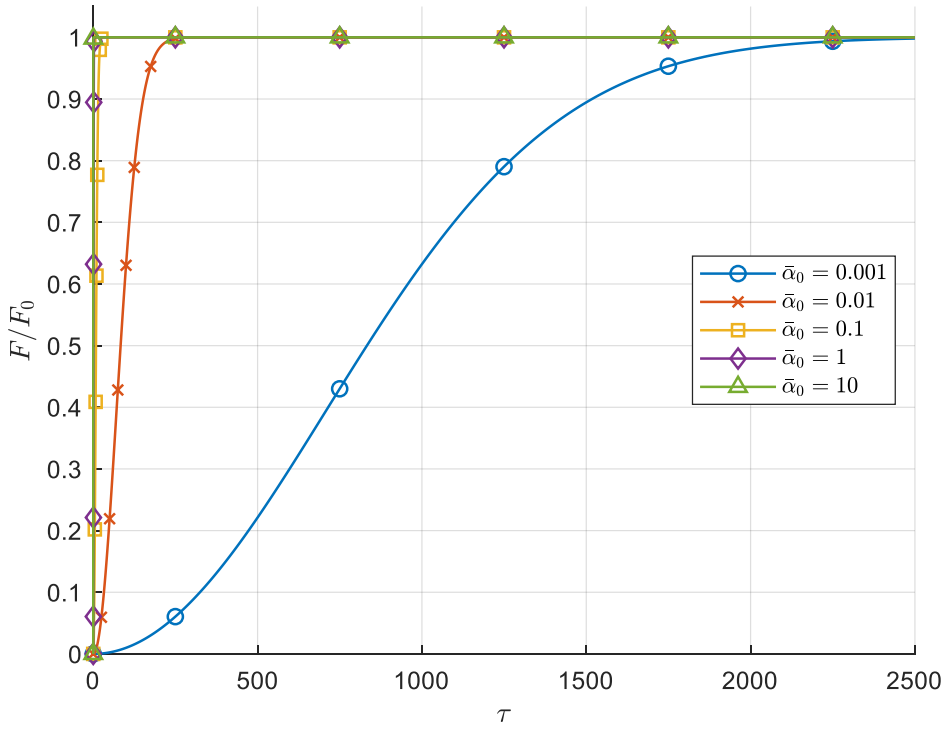

Figure 6.9 Load time history as a function of load rate parameter $\bar{\alpha}$

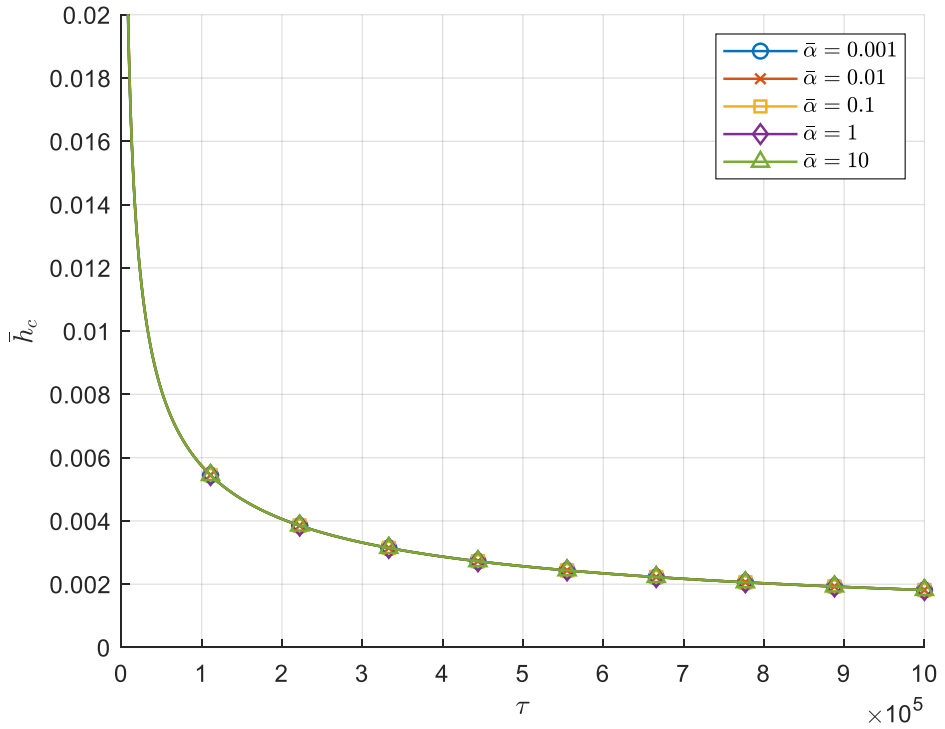

Figure 6.10 Load rate Sweep 1: $\bar{h}_0 = 1, \bar{E} = 1, \bar{b} = 1$; Central film thickness time histories

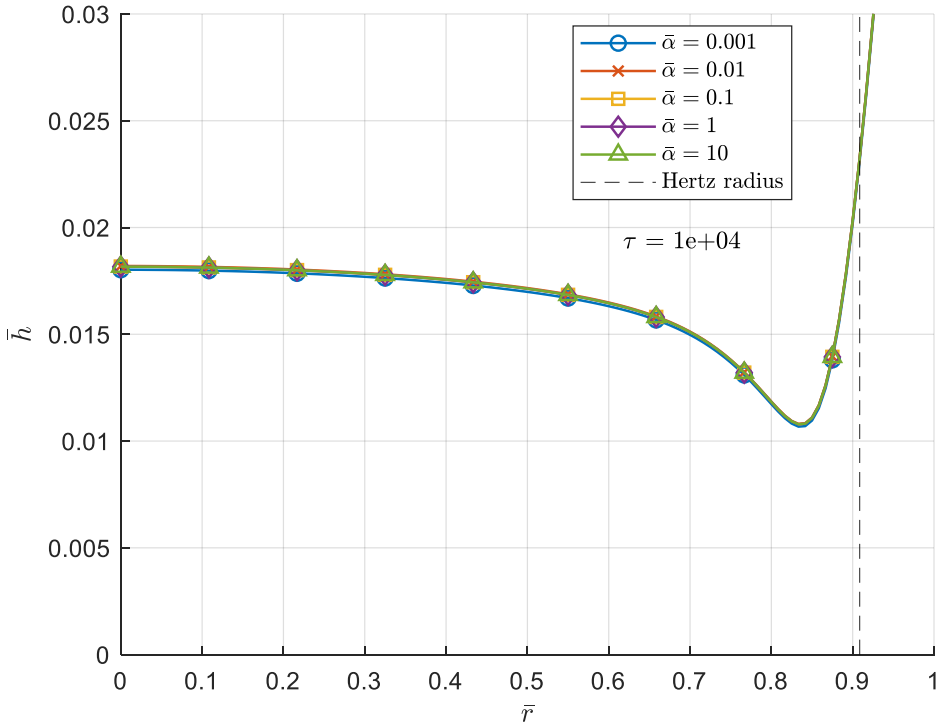

Figure 6.11 Load rate Sweep 1: $\bar{h}_0 = 1, \bar{E} = 1, \bar{b} = 1$; Film thickness profiles; $\tau = 10^4$

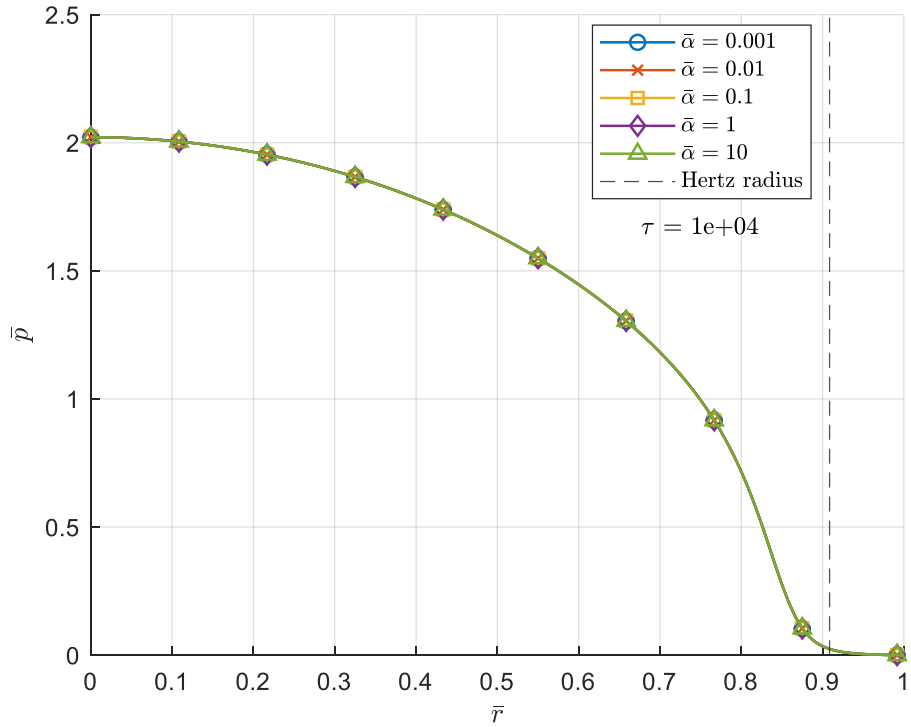

Figure 6.12 Load rate Sweep 1: $\bar{h}_0 = 1, \bar{E} = 1, \bar{b} = 1$; Film pressure profiles; $\tau = 10^4$

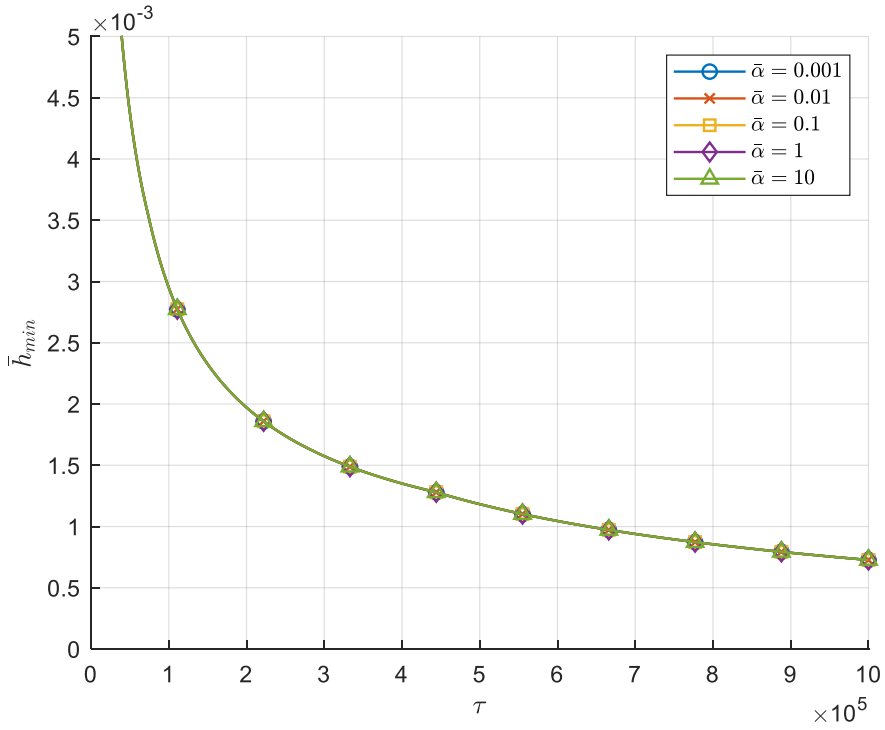

Figure 6.13 Load rate Sweep 1: $\bar{h}_0 = 1, \bar{E} = 1, \bar{b} = 1$; Minimum film thickness time histories

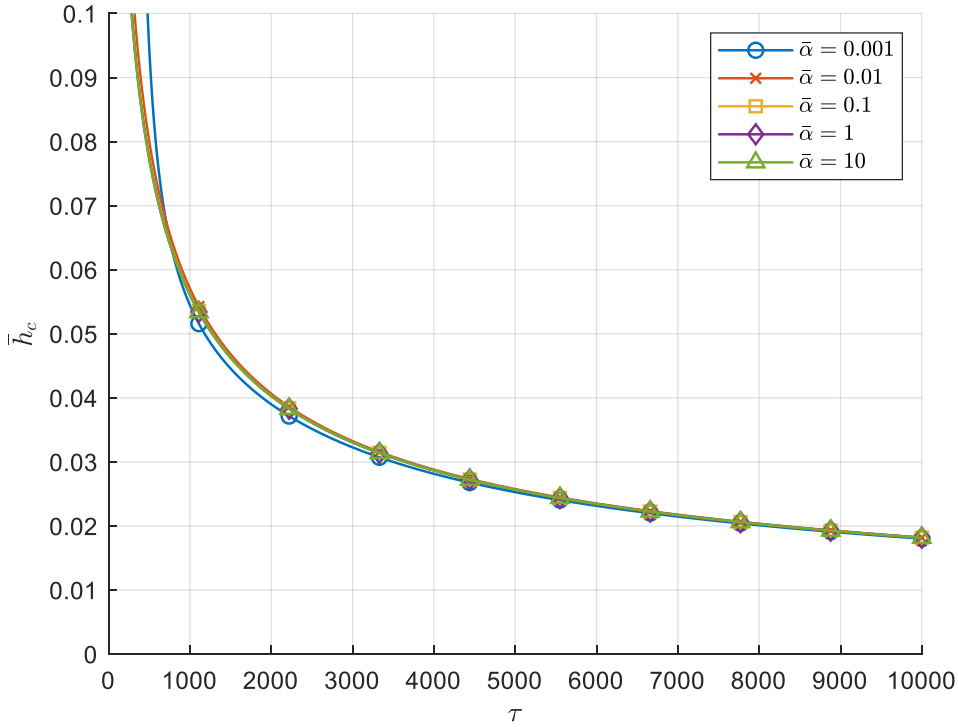

Figure 6.14 Load rate Sweep 1: $\bar{h}_0 = 1, \bar{E} = 1, \bar{b} = 1$; Central film thickness time histories, zoomed to early stages

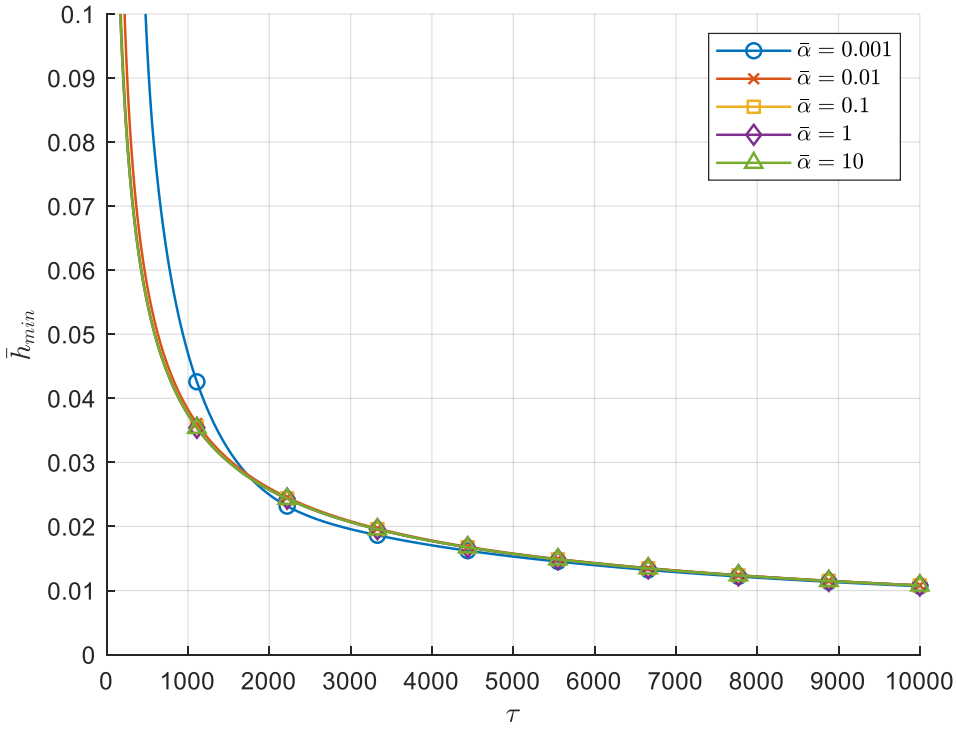

Figure 6.15 Load rate Sweep 1: $\bar{h}_0 = 1, \bar{E} = 1, \bar{b} = 1$; Minimum film thickness time histories, zoomed to early stages

6.3 Elastic Modulus Parameter Sweep

The compliance and thickness of the soft layer greatly affect the behavior of the system. At sufficiently low stiffness values, the "dry contact radius" of the EHL problem is larger than the indenter radius. When this is the case, no significant "ridge" or "shore" of displaced elastomer is developed around the central puddle of lubricant. This causes the lubricant to be quickly squeezed out, even under low pressures. The lowest value of $\bar{E}$ in the first sweep, Figures 6.16 - 6.21, is chosen to show this behavior. The system is extremely sensitive to changes in $\bar{E}$ in this regime, and the times to contact are very short, as seen in Figure 6.20. The point of minimum film thickness cannot be located near the dry contact radius, so it moves to the edge of the indenter, as Figures 6.17 and 6.21 show. The pressure distribution flattens greatly, with a sharp drop to ambient pressure at the boundary $r = R$, shown in Figure 6.18.

For sufficently large values of $\bar{E}$, the increased stiffness of the elastic layer results in much smaller deflections concentrated over a smaller area. This corresponds to much higher pressure in that area to carry the load. These high pressures and small deflections also cause the lubricant to be quickly squeezed out from the gap. A shore does form around the central puddle in this case, but it is significantly shallower than those formed at lower stiffnesses.

As the layer thickness decreases, the true dry contact radius shrinks to be considerably smaller than estimated by Hertzian contact. Once this transition is made, the form of the nondimensional elastic parameter in terms of the Hertzian contact radius is less useful for predicting the system behavior. Sweeps 2 and 3 demonstrate this behavior.

Table 6.3 Nondimensional parameters for elastic modulus sweeps

Sweep	$\bar{h}_0$	$\bar{\alpha}$	$\bar{b}$	$\bar{E}$	Figures
1	1	0.1	∞	0.7, 1, 2, 10	6.16 - 6.21
2			1	0.7, 1, 2, 10	6.22 - 6.27
3			0.1	0.7, 1, 2, 10	6.28 - 6.33

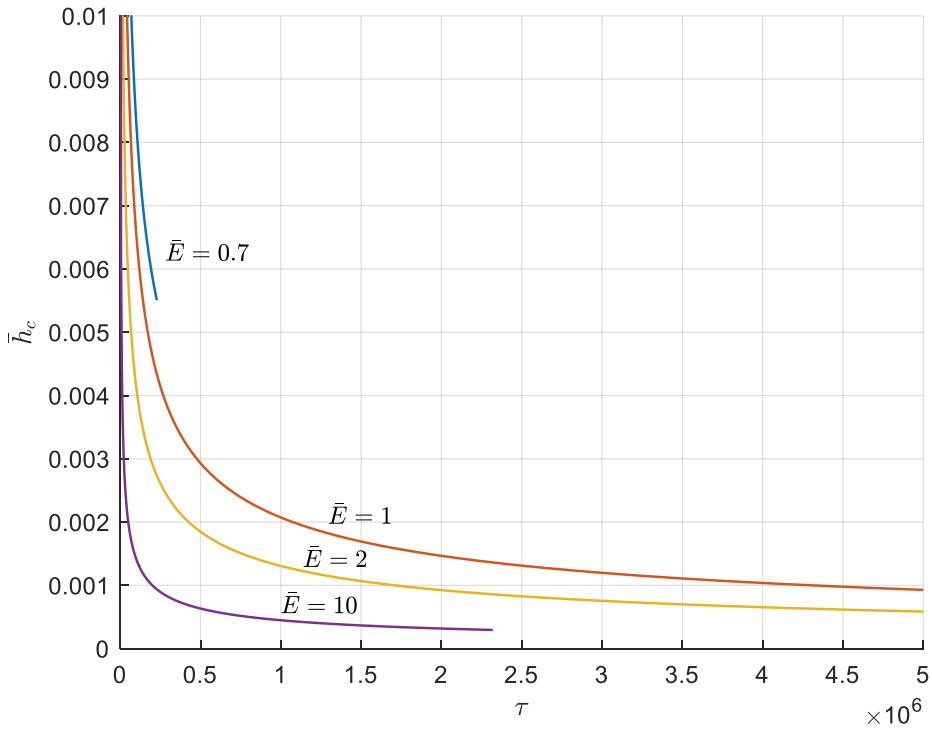

Figure 6.16 Elastic modulus Sweep 1: $\bar{h}_0 = 1, \bar{\alpha} = 0.1, \bar{b} = \infty$; Central film thickness time histories

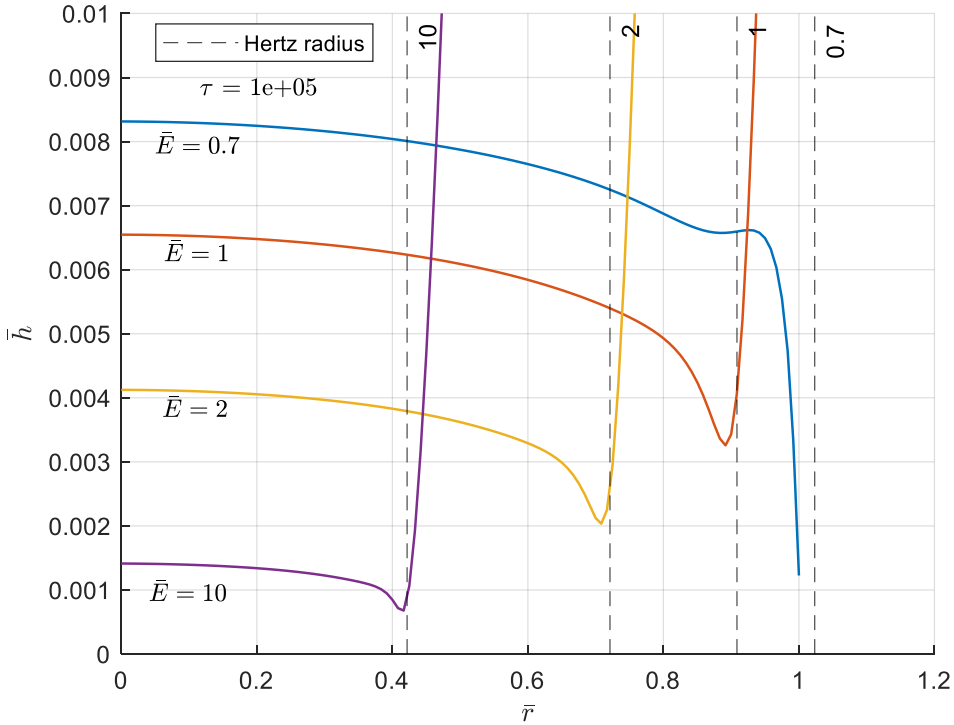

Figure 6.17 Elastic modulus Sweep 1: $\bar{h}_0 = 1, \bar{\alpha} = 0.1, \bar{b} = \infty$; Film thickness profiles, $\tau = 10^5$

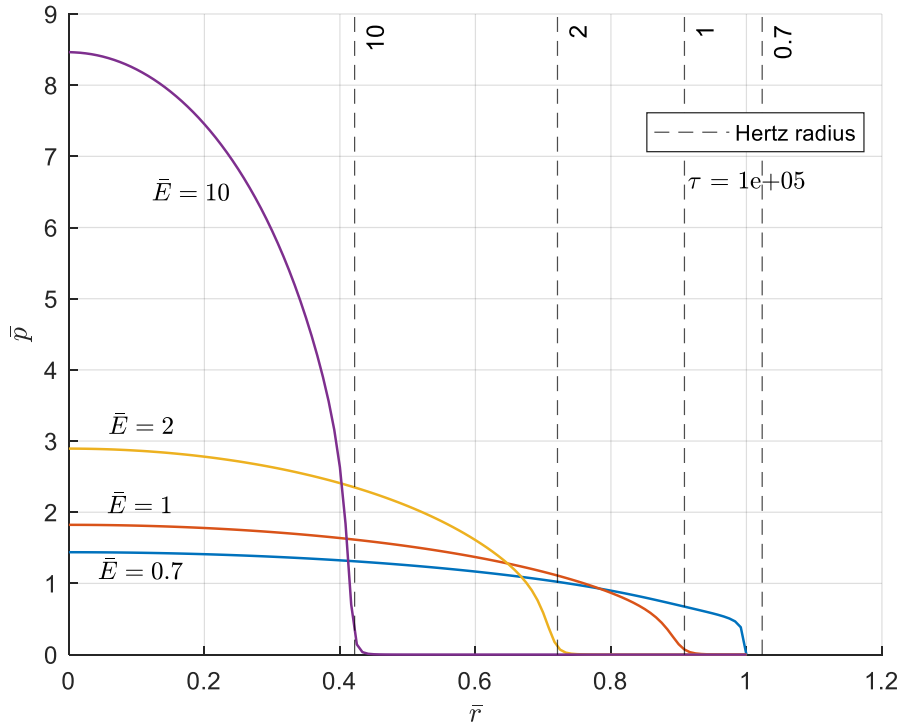

Figure 6.18 Elastic modulus Sweep 1: $\bar{h}_0 = 1, \bar{\alpha} = 0.1, \bar{b} = \infty$; Film pressure profiles, $\tau = 10^5$

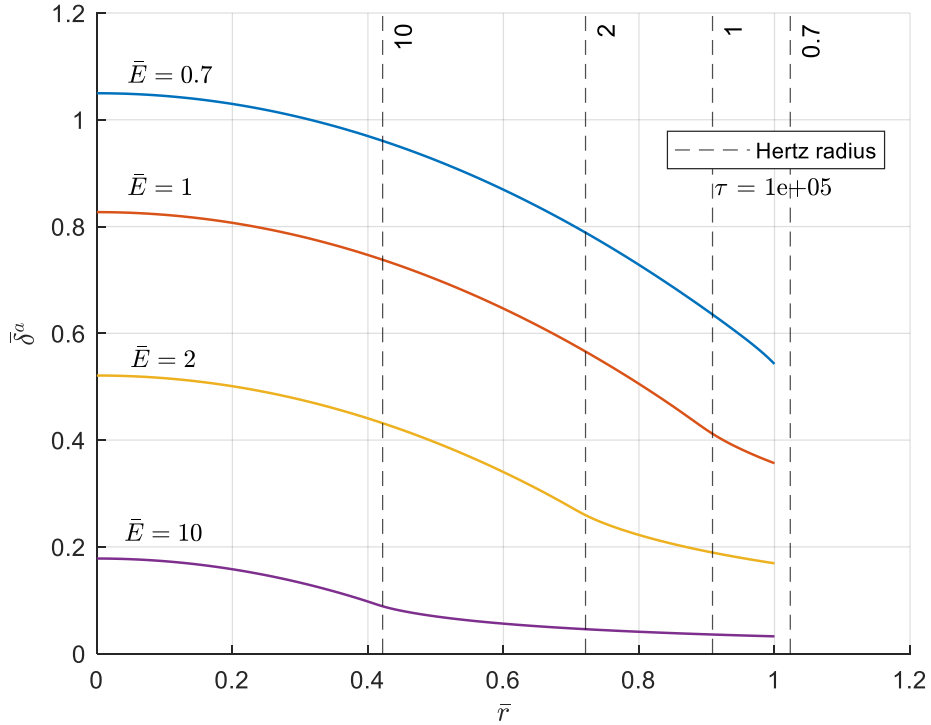

Figure 6.19 Elastic modulus Sweep 1: $\bar{h}_0 = 1, \bar{\alpha} = 0.1, \bar{b} = \infty$; Elastic layer surface deflection profiles, $\tau = 10^5$

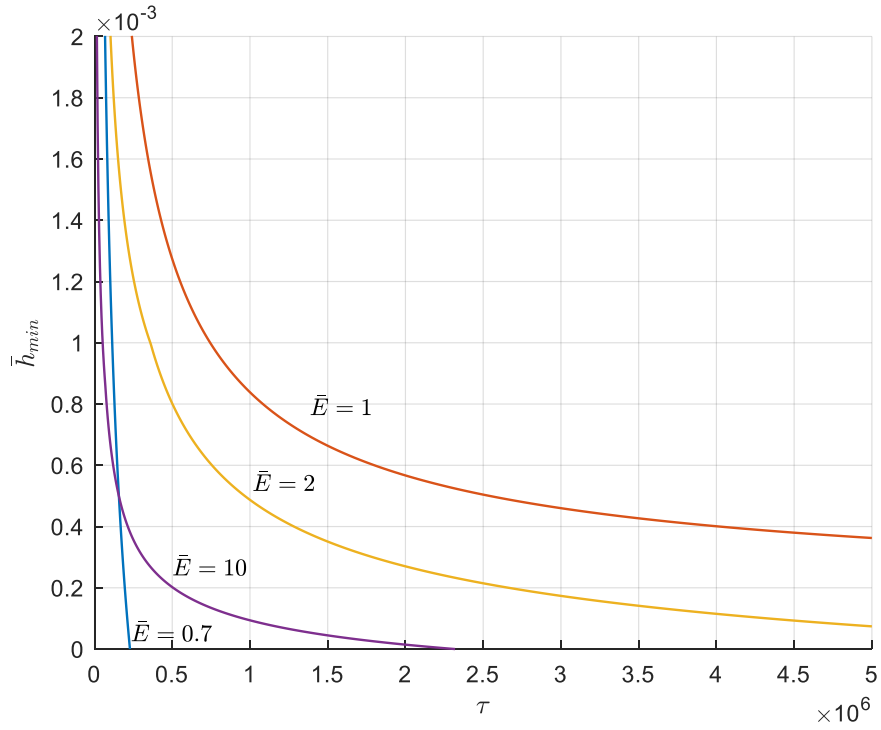

Figure 6.20 Elastic modulus Sweep 1: $\bar{h}_0 = 1, \bar{\alpha} = 0.1, \bar{b} = \infty$; Minimum film thickness time histories

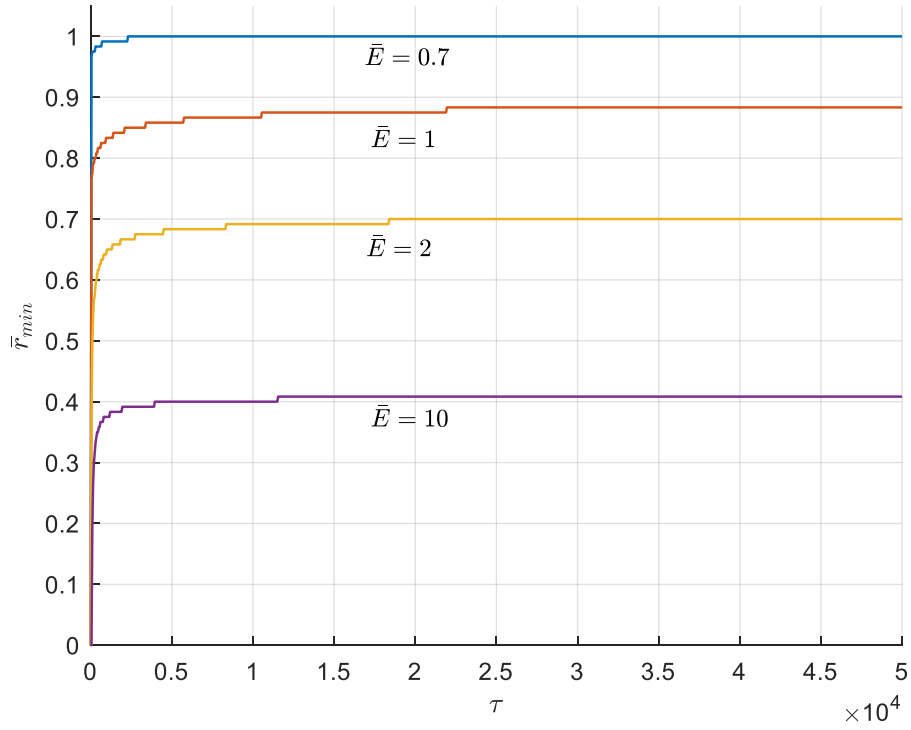

Figure 6.21 Elastic modulus Sweep 1: $\bar{h}_0 = 1, \bar{\alpha} = 0.1, \bar{b} = \infty$; Radial location of minimum film thickness time histories

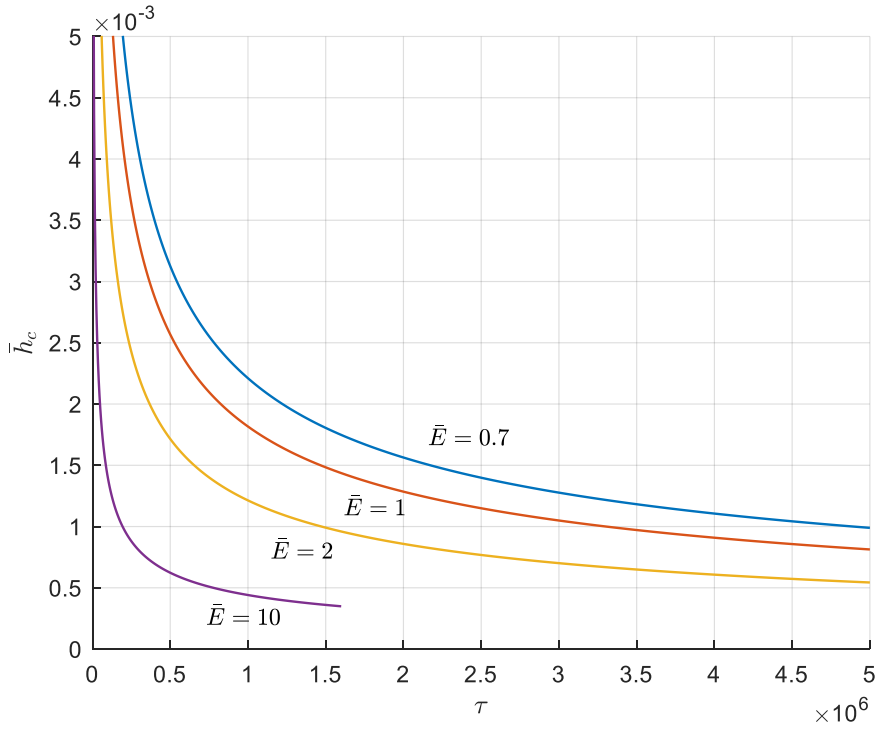

Figure 6.22 Elastic modulus Sweep 2: $\bar{h}_0 = 1, \bar{\alpha} = 0.1, \bar{b} = 1$; Central film thickness time histories

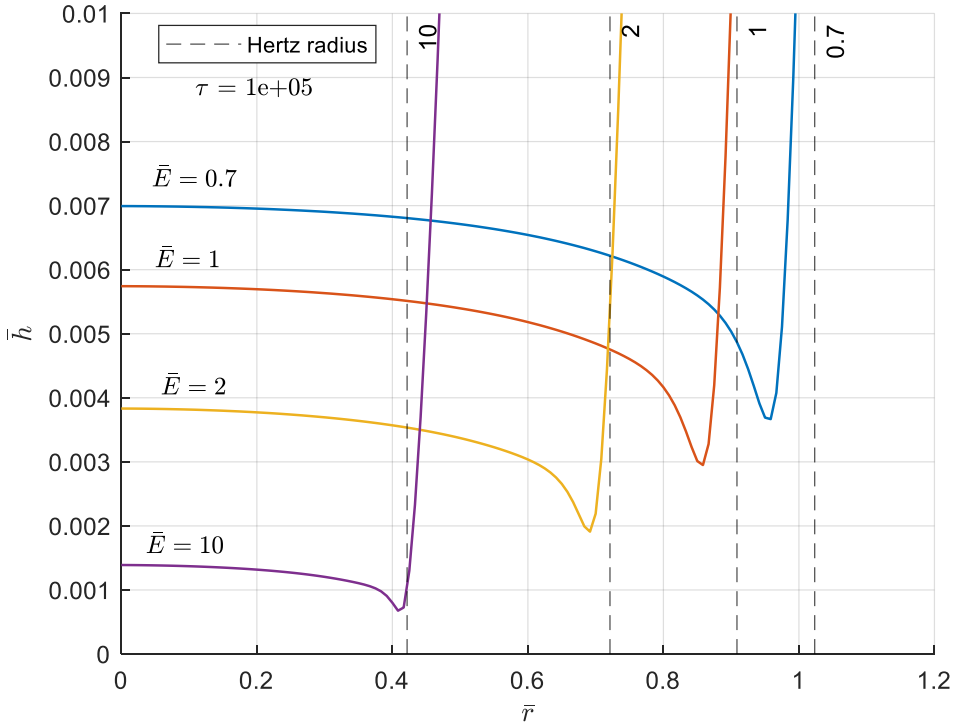

Figure 6.23 Elastic modulus Sweep 2: $\bar{h}_0 = 1, \bar{\alpha} = 0.1, \bar{b} = 1$; Film thickness profiles, $\tau = 10^5$

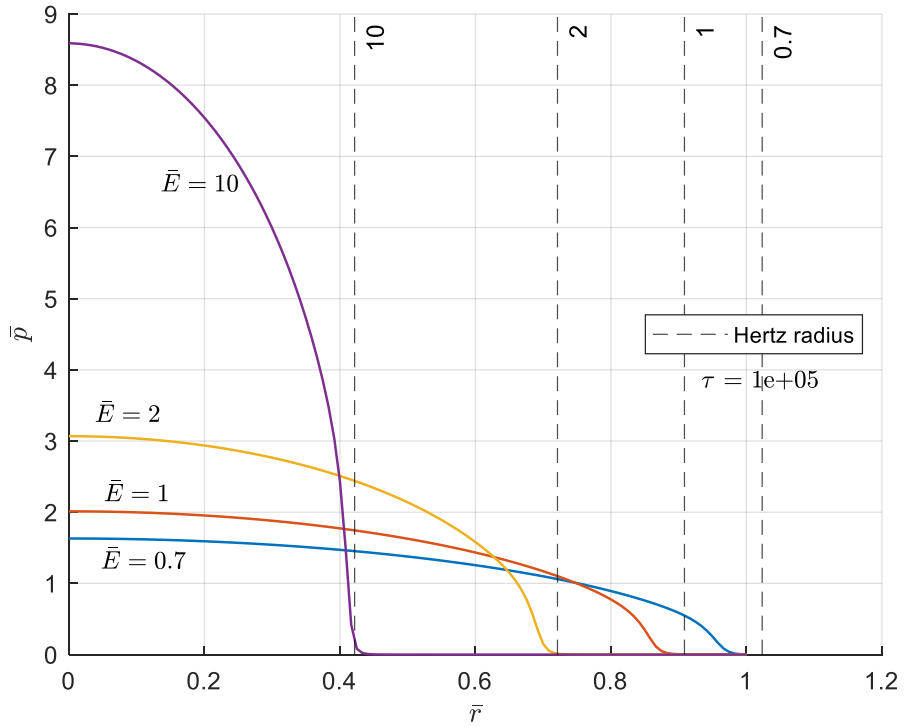

Figure 6.24 Elastic modulus Sweep 2: $\bar{h}_0 = 1, \bar{\alpha} = 0.1, \bar{b} = 1$; Film pressure profiles, $\tau = 10^5$

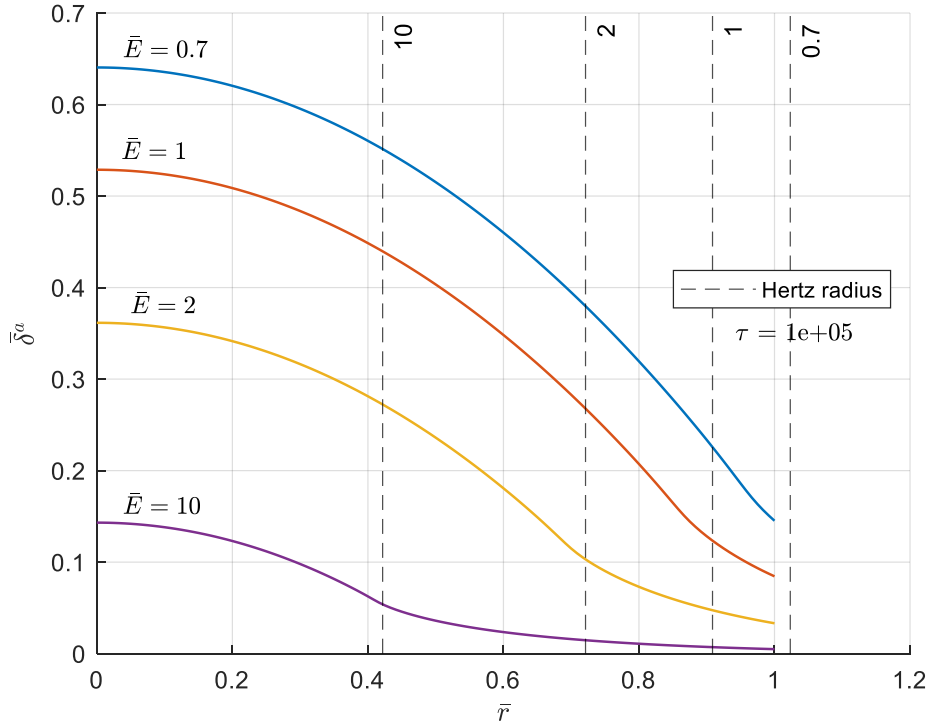

Figure 6.25 Elastic modulus Sweep 2: $\bar{h}_0 = 1, \bar{\alpha} = 0.1, \bar{b} = 1$; Elastic layer surface deflection profiles, $\tau = 10^5$

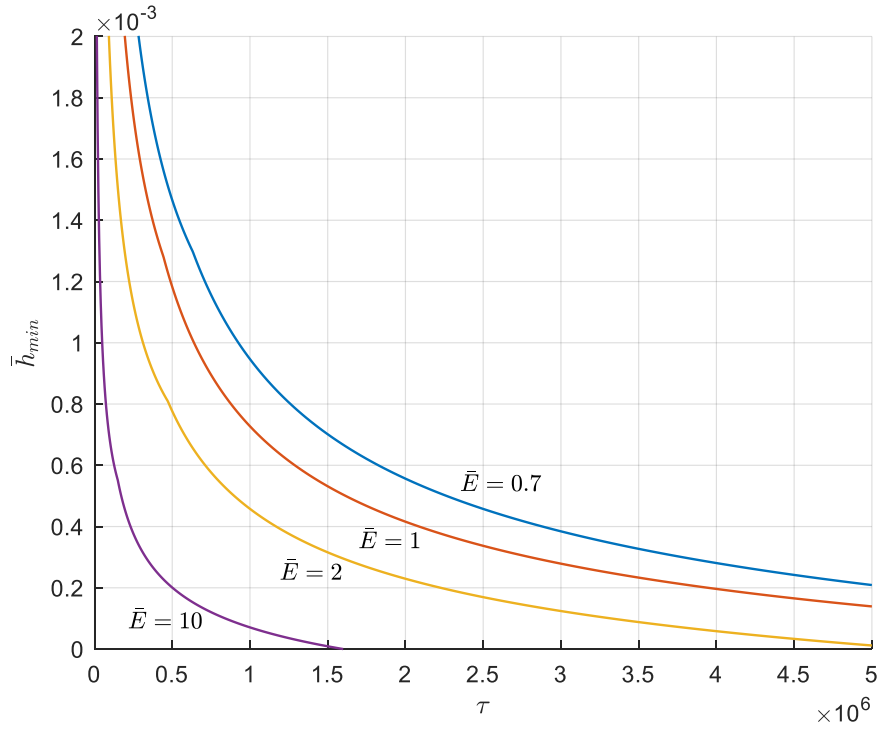

Figure 6.26 Elastic modulus Sweep 2: $\bar{h}_0 = 1, \bar{\alpha} = 0.1, \bar{b} = 1$; Minimum film thickness time histories

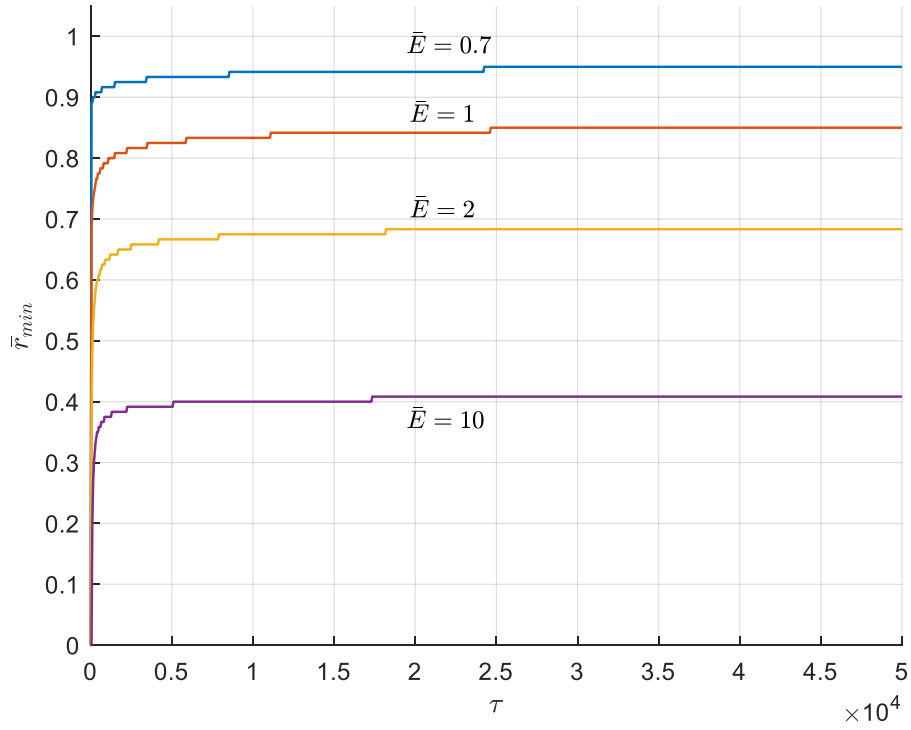

Figure 6.27 Elastic modulus Sweep 2: $\bar{h}_0 = 1, \bar{\alpha} = 0.1, \bar{b} = 1$; Radial location of minimum film thickness time histories

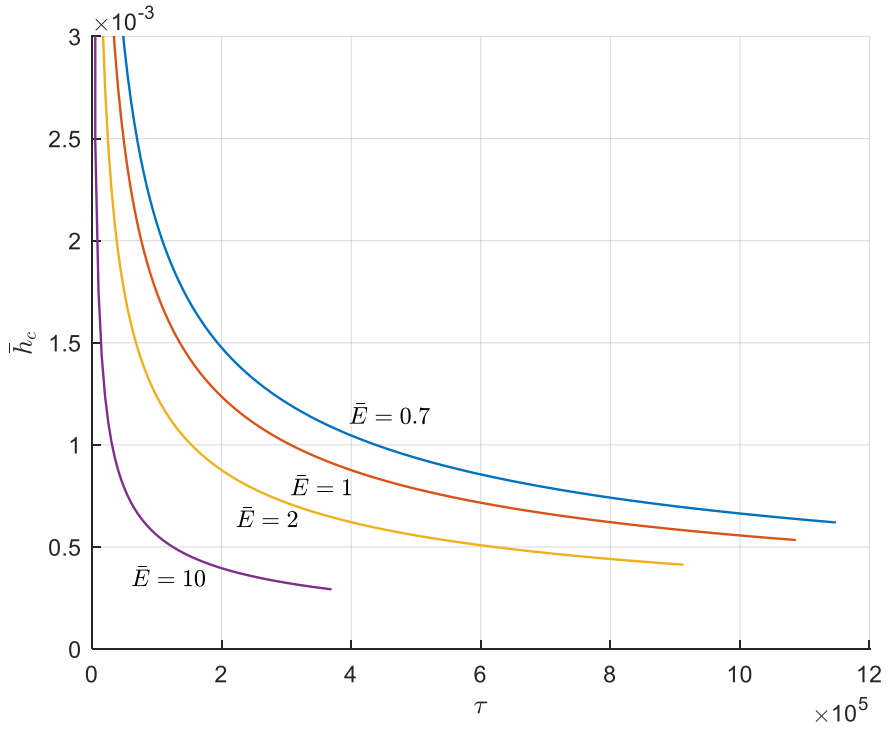

Figure 6.28 Elastic modulus Sweep 3: $\bar{h}_0 = 1, \bar{\alpha} = 0.1, \bar{b} = 0.1$; Central film thickness time histories

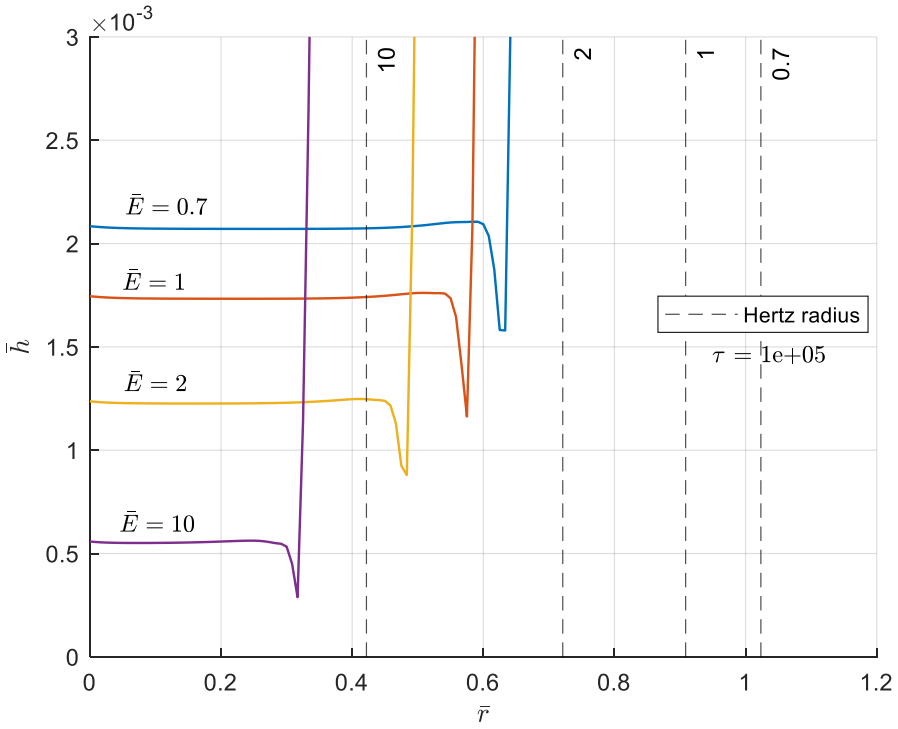

Figure 6.29 Elastic modulus Sweep 3: $\bar{h}_0 = 1, \bar{\alpha} = 0.1, \bar{b} = 0.1$; Film thickness profiles, $\tau = 10^5$

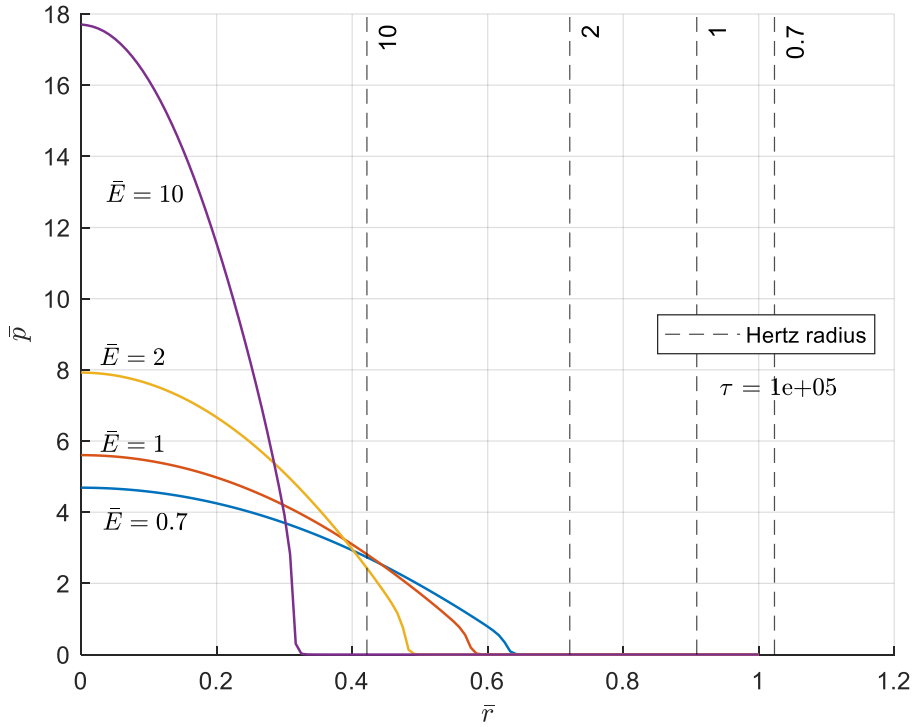

Figure 6.30 Elastic modulus Sweep 3: $\bar{h}_0 = 1, \bar{\alpha} = 0.1, \bar{b} = 0.1$; Film pressure profiles, $\tau = 10^5$

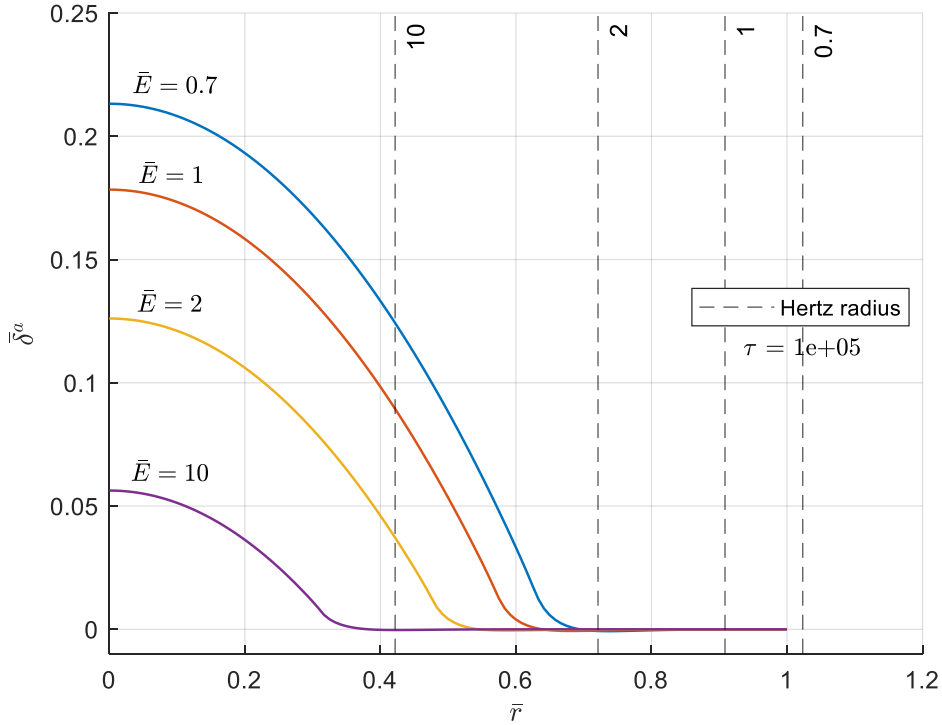

Figure 6.31 Elastic modulus Sweep 3: $\bar{h}_0 = 1, \bar{\alpha} = 0.1, \bar{b} = 0.1$; Elastic layer surface deflection profiles, $\tau = 10^5$

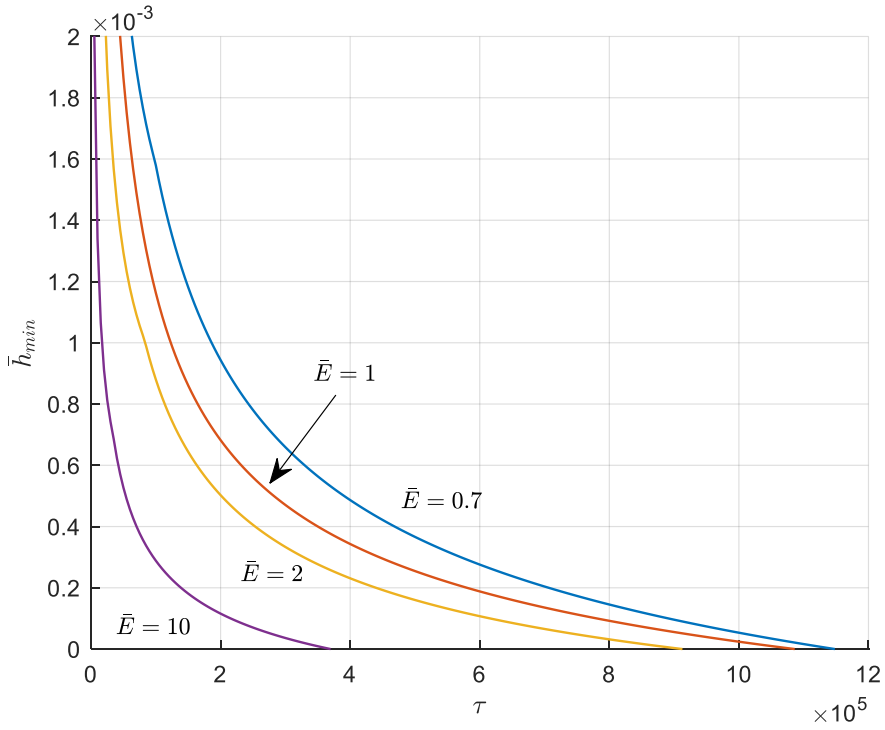

Figure 6.32 Elastic modulus Sweep 3: $\bar{h}_0 = 1, \bar{\alpha} = 0.1, \bar{b} = 0.1$; Minimum film thickness time histories

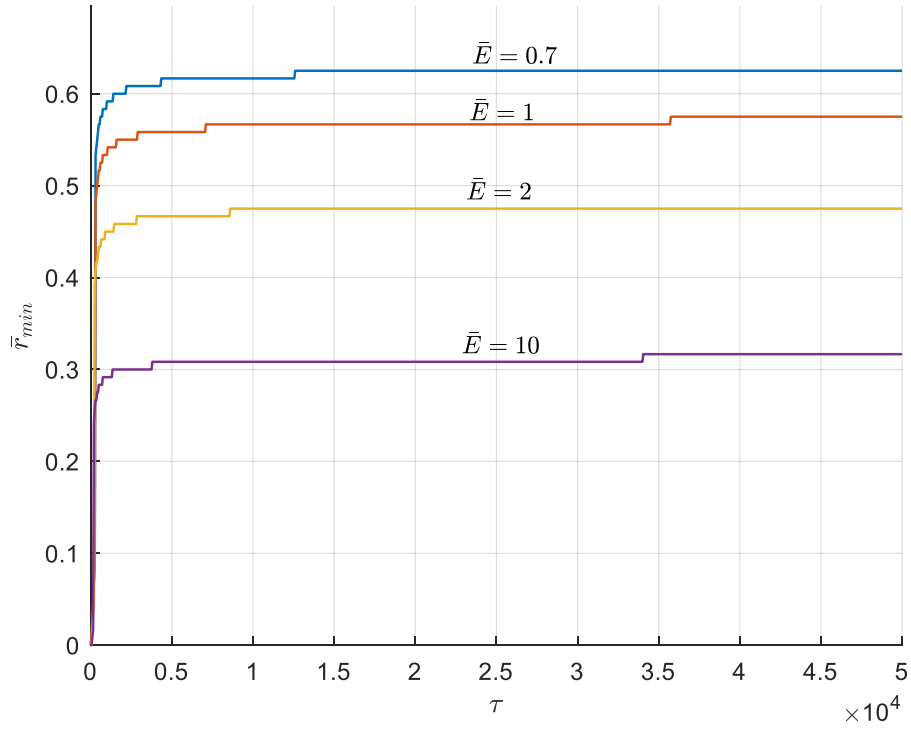

Figure 6.33 Elastic modulus Sweep 3: $\bar{h}_0 = 1, \bar{\alpha} = 0.1, \bar{b} = 0.1$; Radial location of minimum film thickness time histories

Chapter 7

Results and Discussion: Conical Indenter

7.1 Initial Clearance Parameter Sweep

Similar to the paraboloid case, a bearing comprised of a conical indenter on an elastic surface displays little to no dependence on the initial clearance. Table 7.1 shows the nondimensional parameters for the results shown in Figures 7.1 - 7.6.

Just like the paraboloid indenter, the conical indenter crashes down through the initial clearance until the film thickness is reduced enough to develop load-carrying pressures, as Figure 7.1 shows. Unsurprisingly, the minimum film thickness and peak pressure occur at the tip of the indenter, as seen in Figures 7.2 and 7.3. This makes sense since the tip is pressed deeply into the elastic layer, as Figure 7.4 shows.

Figure 7.2 shows the formation of shore material pushed up from the surface of the elastic layer, reminiscent of the effect seen in the case of the paraboloid indenter. However, this effect is much more subtle here, and seems to be not nearly as effective. The time scales for gap closure are much shorter than for the paraboloid indenter. Figure 7.5 shows an early stage film thickness profile to show the evolution of the shallow shore of elastomer.

Figure 7.6 repeats the central film thickness results of Figure 7.1 on a Log-Log scale. The conical indenter does not appear to follow a simple power law like the paraboloid indenter.

Table 7.1 Nondimensional parameters for initial clearance sweeps

Sweep	$\bar{\alpha}$	$\bar{E}$	$\bar{b}$	$\bar{h}_0$
1	1	1	1	1, 10, 100

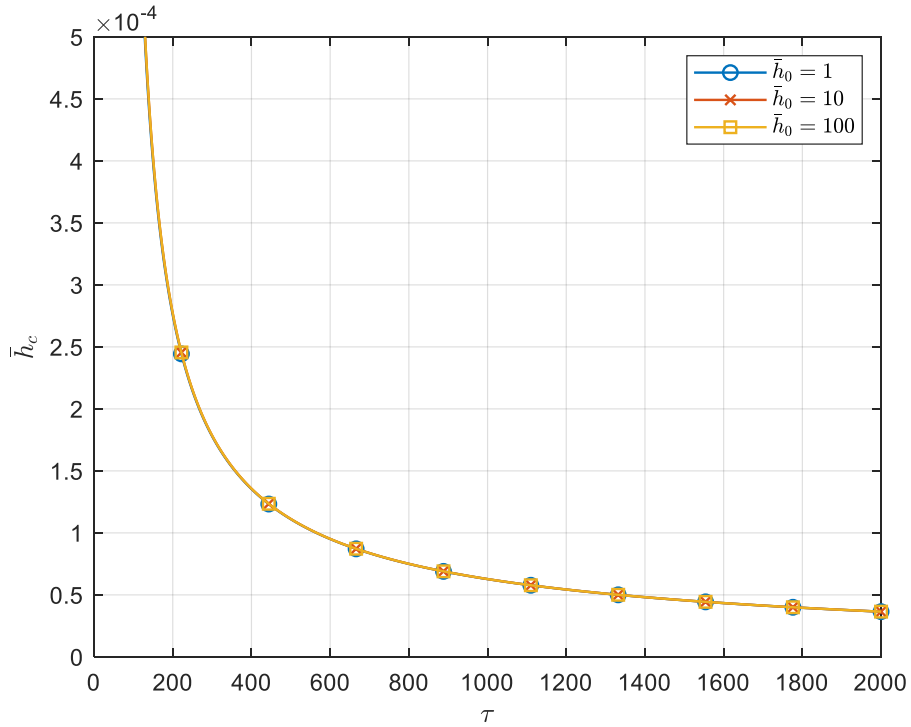

Figure 7.1 Initial Clearance Sweep 1: $\bar{\alpha} = 1, \bar{E} = 1, \bar{b} = 1$; Central film thickness time histories

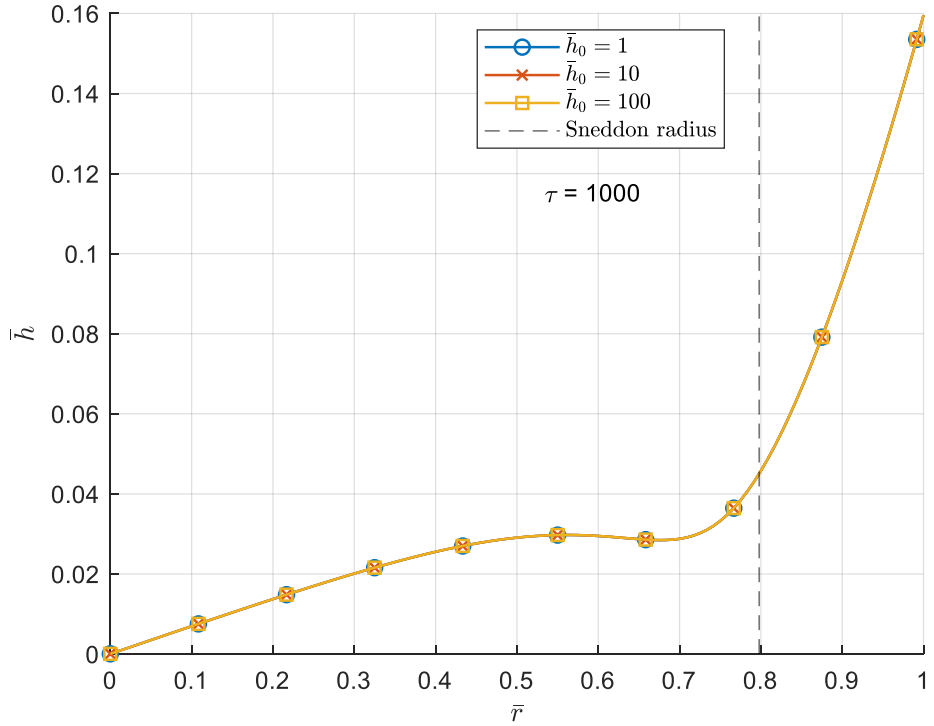

Figure 7.2 Initial Clearance Sweep 1: $\bar{\alpha} = 1, \bar{E} = 1, \bar{b} = 1$; Film thickness profiles; $\tau = 1000$

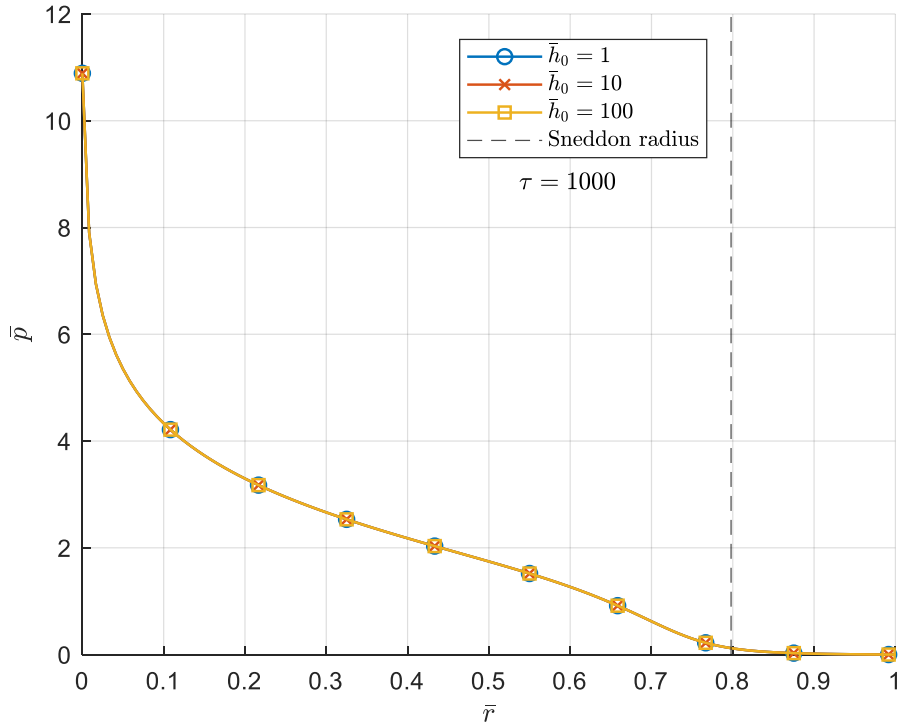

Figure 7.3 Initial Clearance Sweep 1: $\bar{\alpha} = 1, \bar{E} = 1, \bar{b} = 1$; Film pressure profiles; $\tau = 1000$

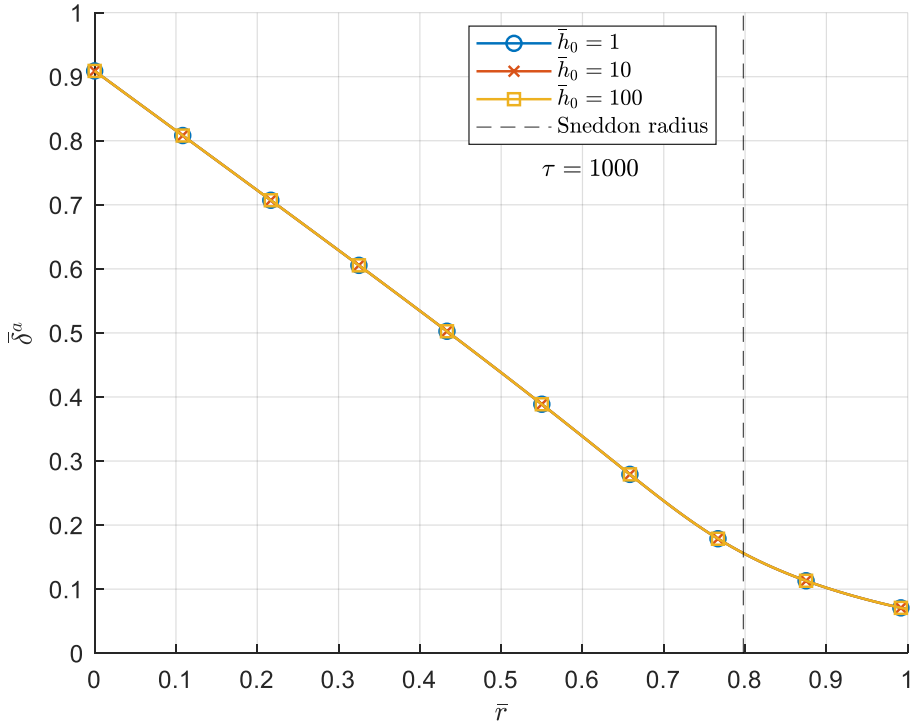

Figure 7.4 Initial Clearance Sweep 1: $\bar{\alpha} = 1, \bar{E} = 1, \bar{b} = 1$; Elastic layer surface deflection profiles; $\tau = 1000$

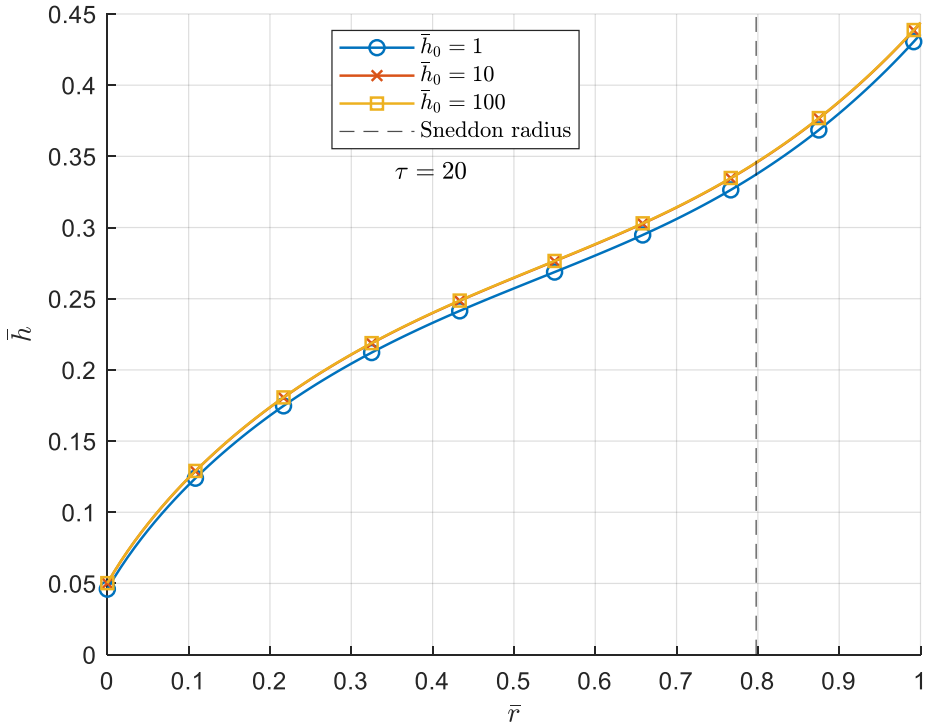

Figure 7.5 Initial Clearance Sweep 1: $\bar{\alpha} = 1, \bar{E} = 1, \bar{b} = 1$; Film thickness profiles; $\tau = 20$

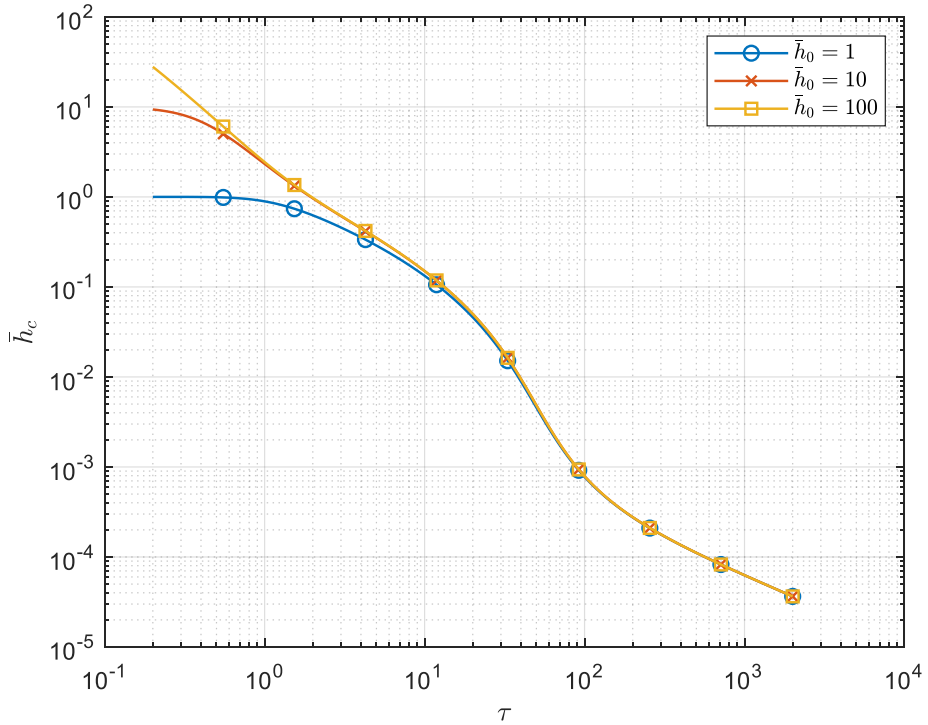

Figure 7.6 Initial Clearance Sweep 1: $\bar{\alpha} = 1, \bar{E} = 1, \bar{b} = 1$; Central film thickness time histories, Log-Log scale

7.2 Load Rate Parameter Sweep

Like the paraboloid indenter, the conical indenter exhibits little sensitivity to the load rate parameter provided that it is large enough that the load reaches full measure on a much shorter time scale than the natural transient behavior of the system. Since the conical indenter does approach contact much faster than a comparable paraboloid indenter, a larger value of the load rate parameter may be required to give a reasonably approximation of a step load.

Table 7.2 gives nondimensional specifications for a sweep of values of the load rate parameter. Figures 7.7 - 7.10 show essentially identical results for all values of $\bar{\alpha}$.

Table 7.2 Nondimensional parameters for load rate sweeps

Sweep	$\bar{h}_0$	$\bar{b}$	$\bar{E}$	$\bar{\alpha}$
1	10	1	1	10^{-2}, 10^{-1}, 1, 10

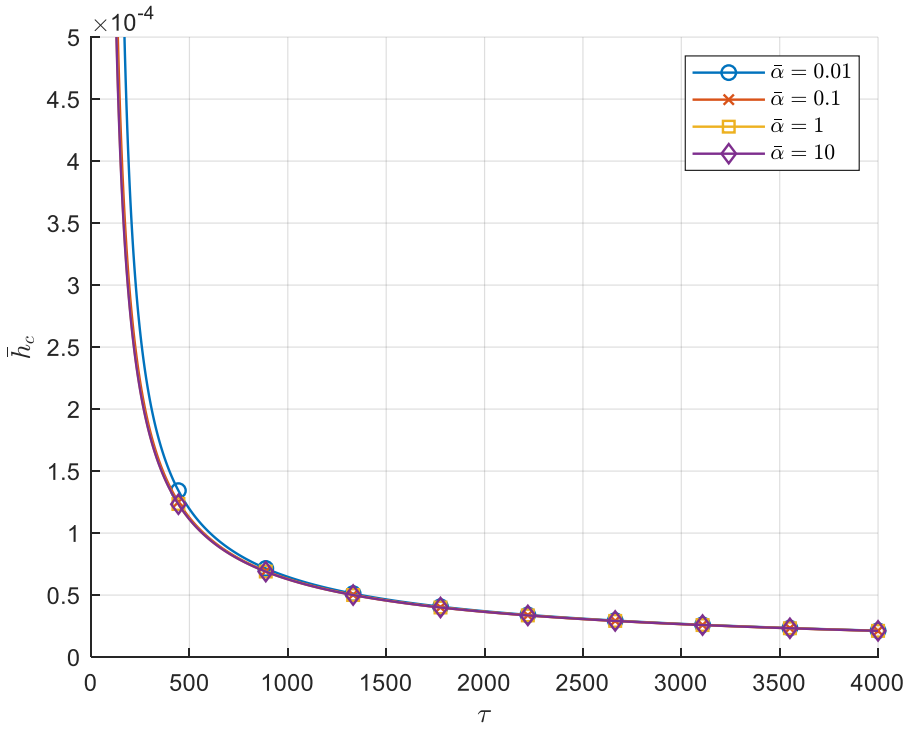

Figure 7.7 Load rate sweep 1: $\bar{h}_0 = 10, \bar{E} = 1, \bar{b} = 1$; Central film thickness time histories

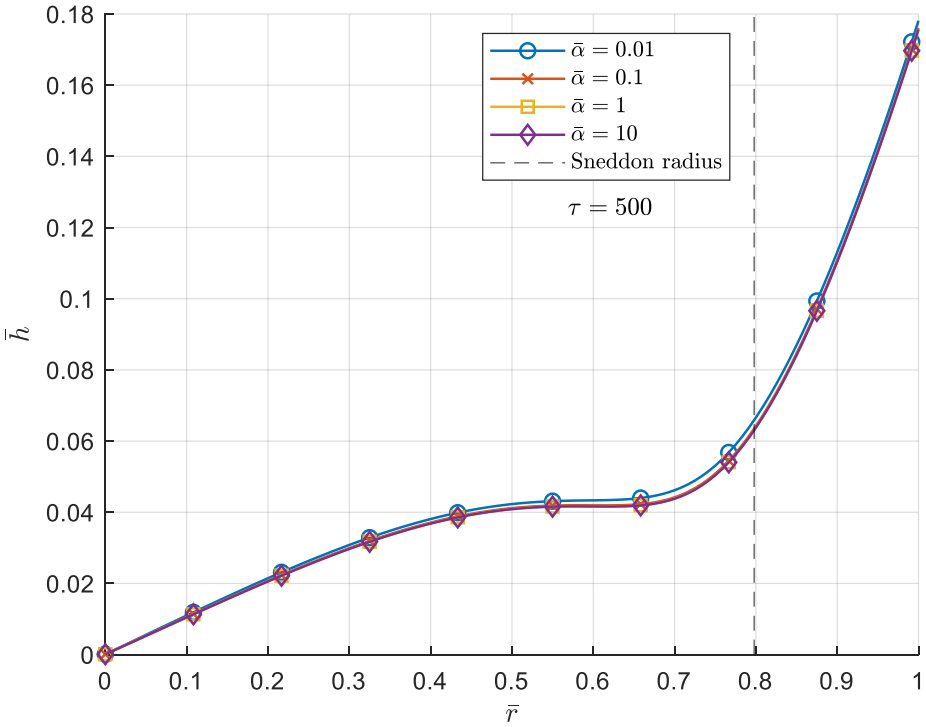

Figure 7.8 Load rate Sweep 1: $\bar{h}_0 = 10, \bar{E} = 1, \bar{b} = 1$; Film thickness profiles, $\tau = 500$

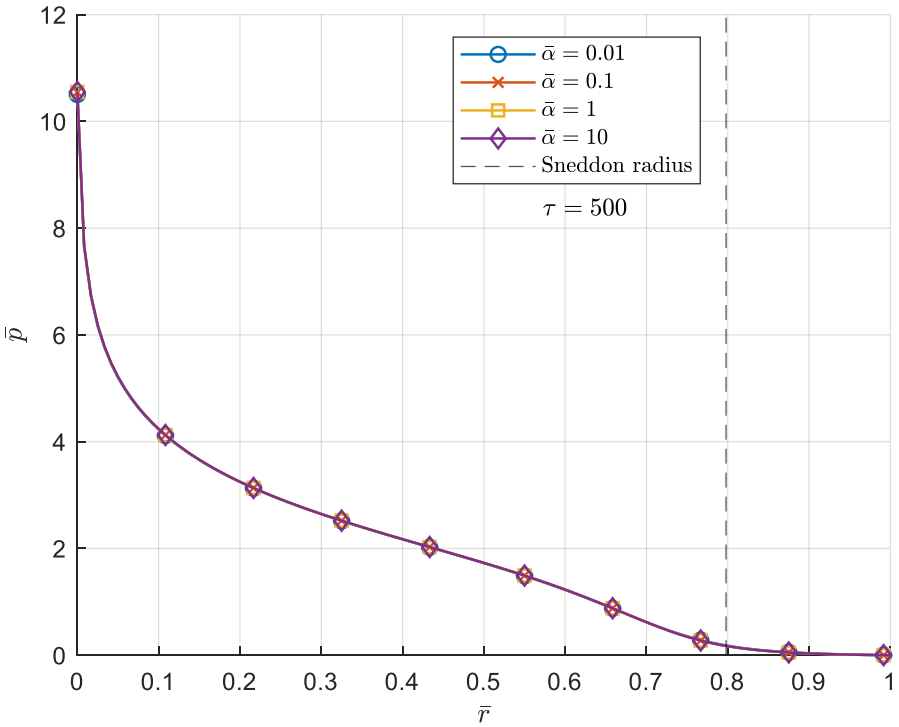

Figure 7.9 Load rate Sweep 1: $\bar{h}_0 = 10, \bar{E} = 1, \bar{b} = 1$; Film pressure profiles, $\tau = 500$

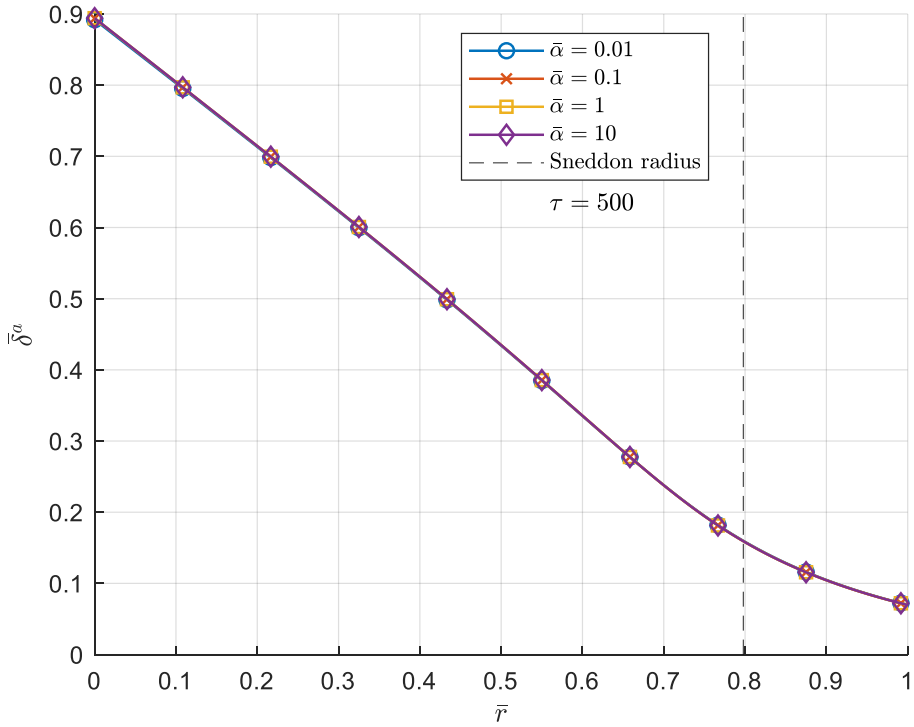

Figure 7.10 Load rate Sweep 1: $\bar{h}_0 = 10, \bar{E} = 1, \bar{b} = 1$; Elastic layer surface deflection profiles, $\tau = 500$

7.3 Elastic Modulus Parameter Sweep

Again, similar to the paraboloid indenter, the lubricant behavior between a conical indenter and an elastic surface is heavily dependent on the elastic layer stiffness and thickness. Table 7.3 gives the nondimensional parameters for three sweeps of the elastic modulus parameter for a range of layer thicknesses.

The first sweep corresponds to an elastic halfspace, whose results are shown in Figures 7.11 - 7.14. All four cases for the elastic halfspace reach zero film thickness extremely quickly; on a timescale almost 100x shorter than seen in sweeps 2 and 3. The film thicknesses shown in Figure 7.12 show little of the flattening affect seen in the case of the paraboloid indenter. Figures 7.16 and 7.20 show a bit of this flattening for the two sweeps with finite layer thicknesses. However, in all three sweeps, there is no significant formation of a shore of material to keep the lubricant contained in a central pocket.

This is compounded by the nature of the pressure distribution for the conical indenter. Unlike pressure distributions for the paraboloid indenter, which appear to have a gradient of zero at the origin, the pressure beneath the conical indenter has an extremely steep gradient. This gradient serves to increase pressure-driven flow of the lubricant away from the center of the bearing and contribute to the short times to closure.

In all three sweeps, the cases where $\bar{E} = 10$ reach significantly higher pressures than any of the softer cases. This requires some extra care in interpretation, because depending on the scale of the dimensional specifications, these large nondimensional pressures may result in physical pressures that fall into the range of piezoviscous effects, which are not modeled here.

Table 7.3 Nondimensional parameters for elastic modulus sweeps

Sweep	$\bar{h}_0$	$\bar{\alpha}$	$\bar{b}$	$\bar{E}$	Figures
1	10	1	∞	0.6, 1, 2, 10	7.11 - 7.14
2			1	0.6, 1, 2, 10	7.15 - 7.18
3			0.1	0.6, 1, 2, 10	7.19 - 7.22

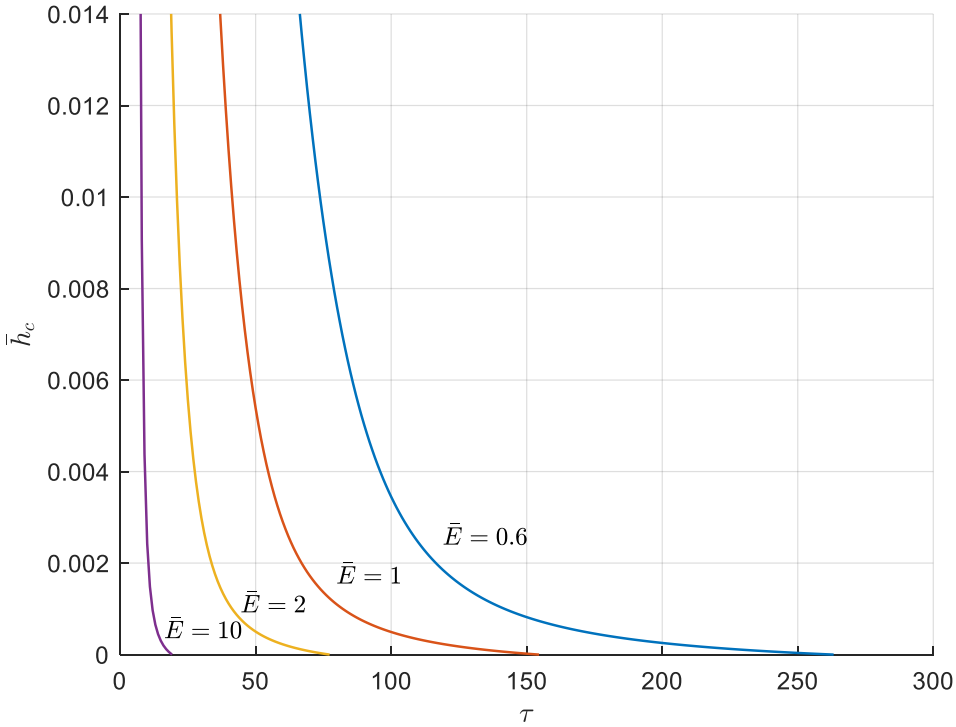

Figure 7.11 Elastic modulus Sweep 1: $\bar{h}_0 = 10, \bar{\alpha} = 1, \bar{b} = \infty$; Central film thickness time histories

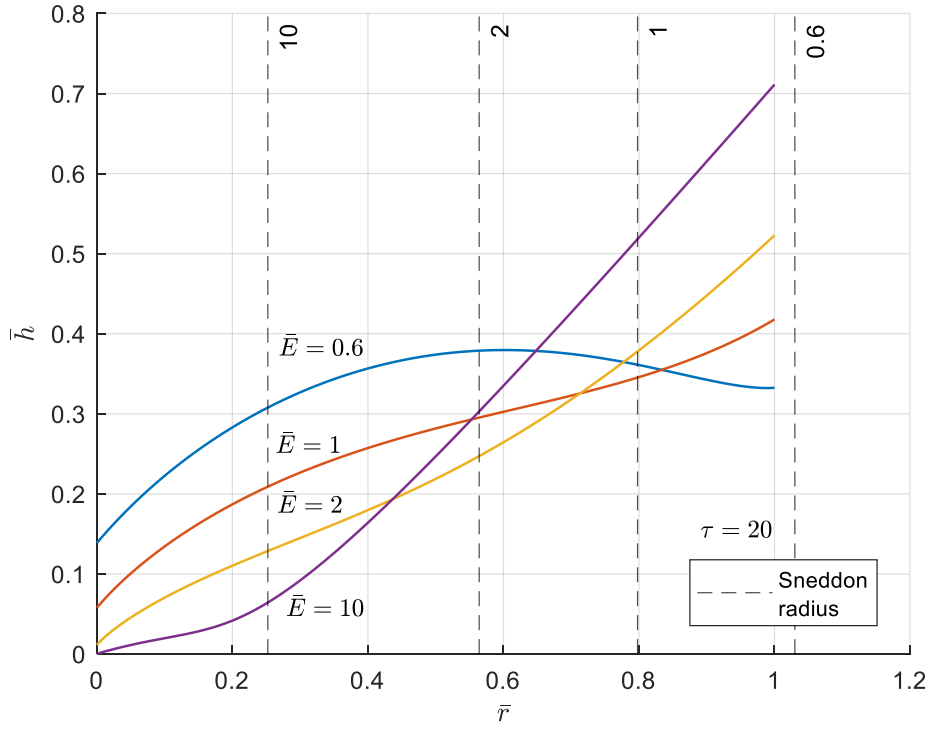

Figure 7.12 Elastic modulus Sweep 1: $\bar{h}_0 = 10, \bar{\alpha} = 1, \bar{b} = \infty$; Film thickness profiles, $\tau = 20$

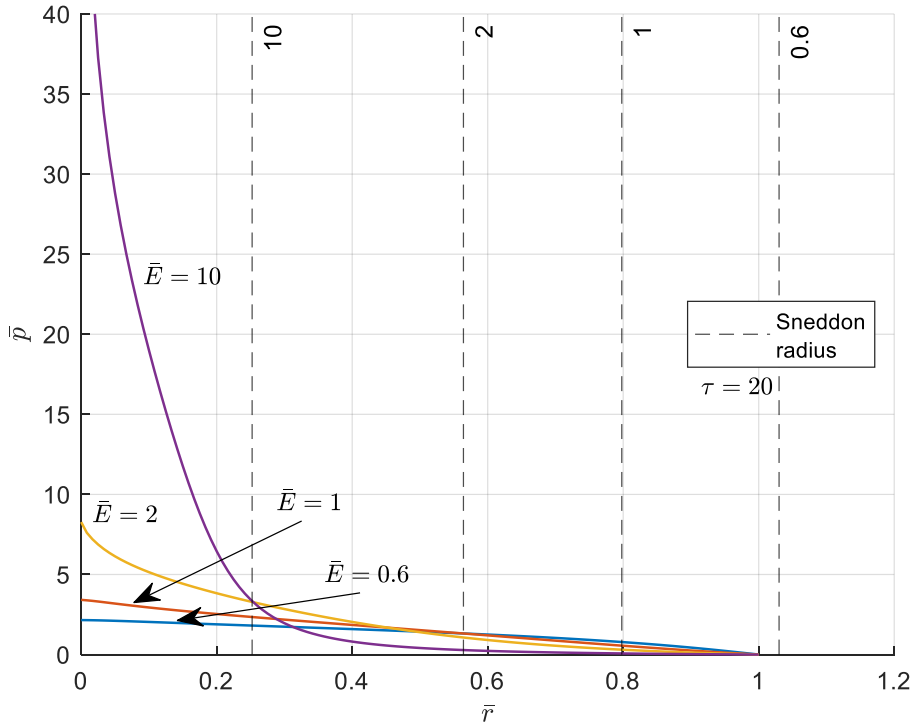

Figure 7.13 Elastic modulus Sweep 1: $\bar{h}_0 = 10, \bar{\alpha} = 1, \bar{b} = \infty$; Film pressure profiles, $\tau = 20$

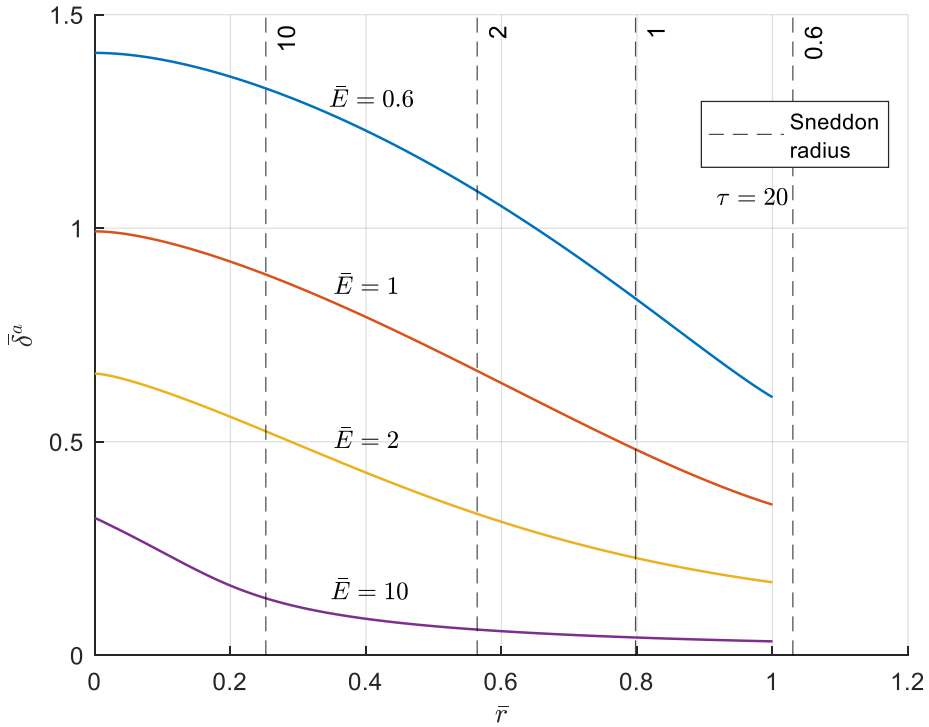

Figure 7.14 Elastic modulus Sweep 1: $\bar{h}_0 = 10, \bar{\alpha} = 1, \bar{b} = \infty$; Elastic layer surface deflection profiles, $\tau = 20$

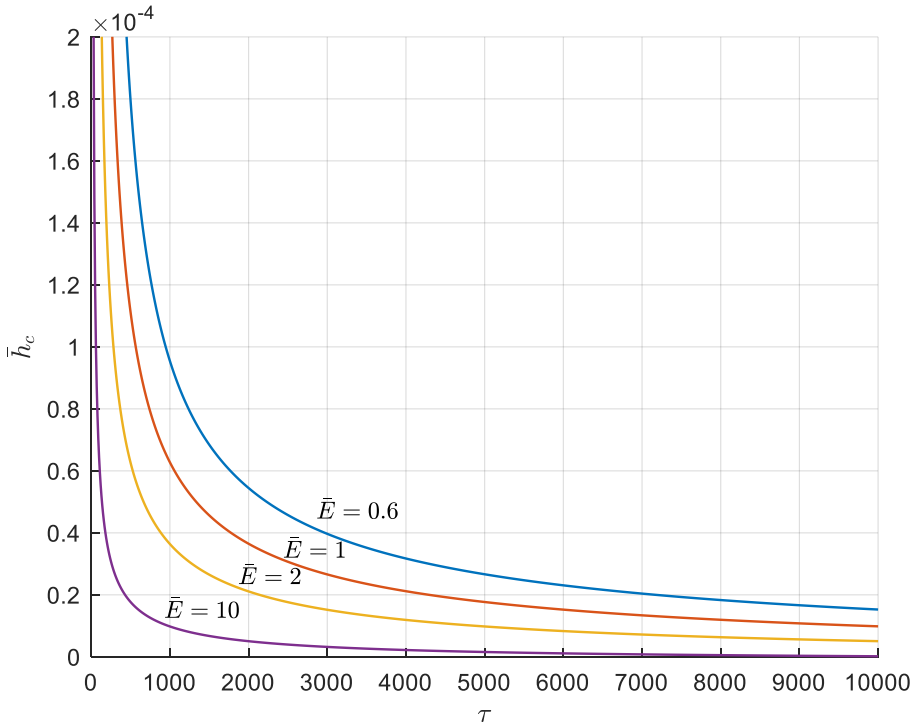

Figure 7.15 Elastic modulus Sweep 2: $\bar{h}_0 = 10, \bar{\alpha} = 1, \bar{b} = 1$; Central film thickness time histories

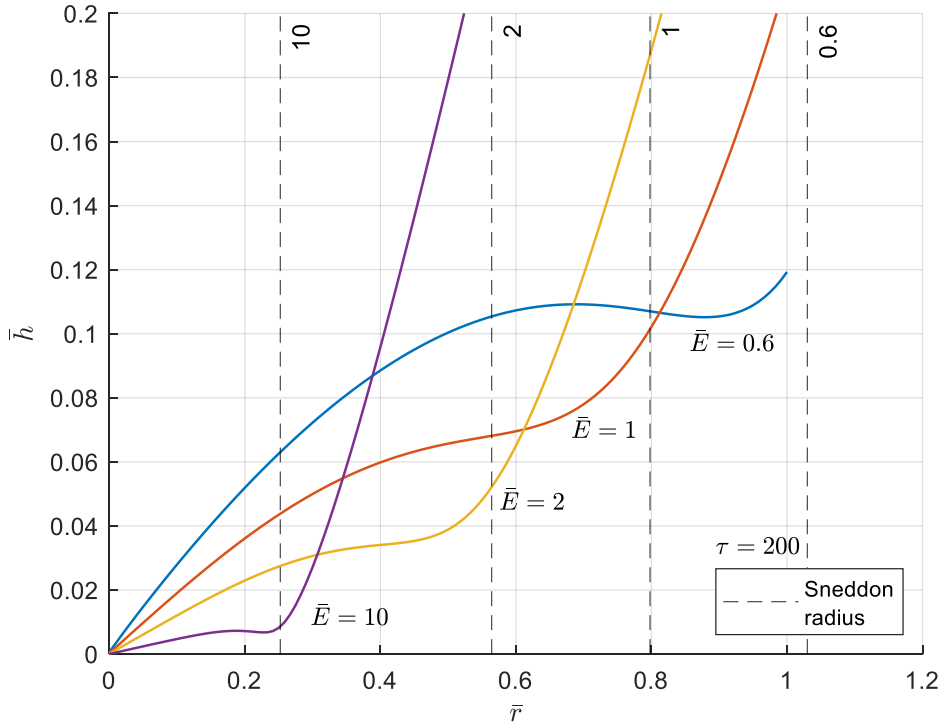

Figure 7.16 Elastic modulus Sweep 2: $\bar{h}_0 = 10, \bar{\alpha} = 1, \bar{b} = 1$; Film thickness profiles, $\tau = 200$

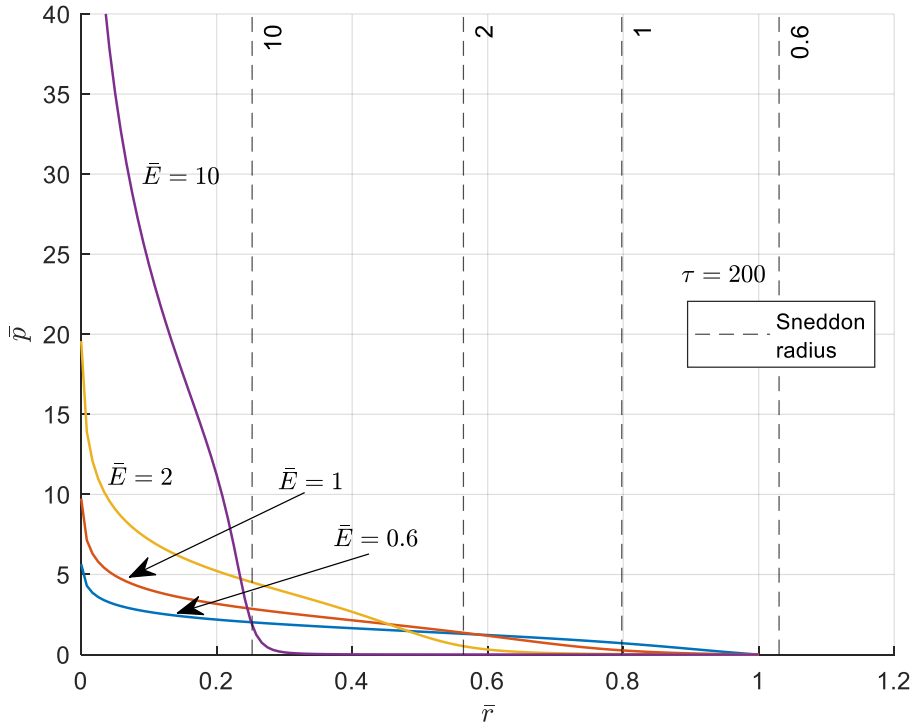

Figure 7.17 Elastic modulus Sweep 2: $\bar{h}_0 = 10, \bar{\alpha} = 1, \bar{b} = 1$; Film pressure profiles, $\tau = 200$

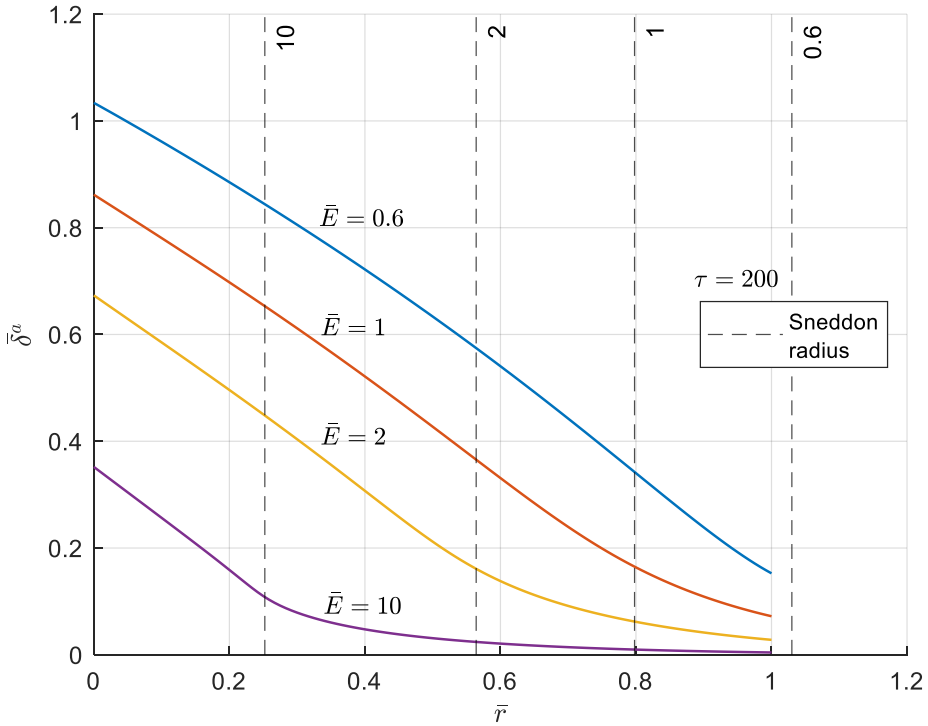

Figure 7.18 Elastic modulus Sweep 2: $\bar{h}_0 = 10, \bar{\alpha} = 1, \bar{b} = 1$; Elastic layer surface deflection profiles, $\tau = 200$

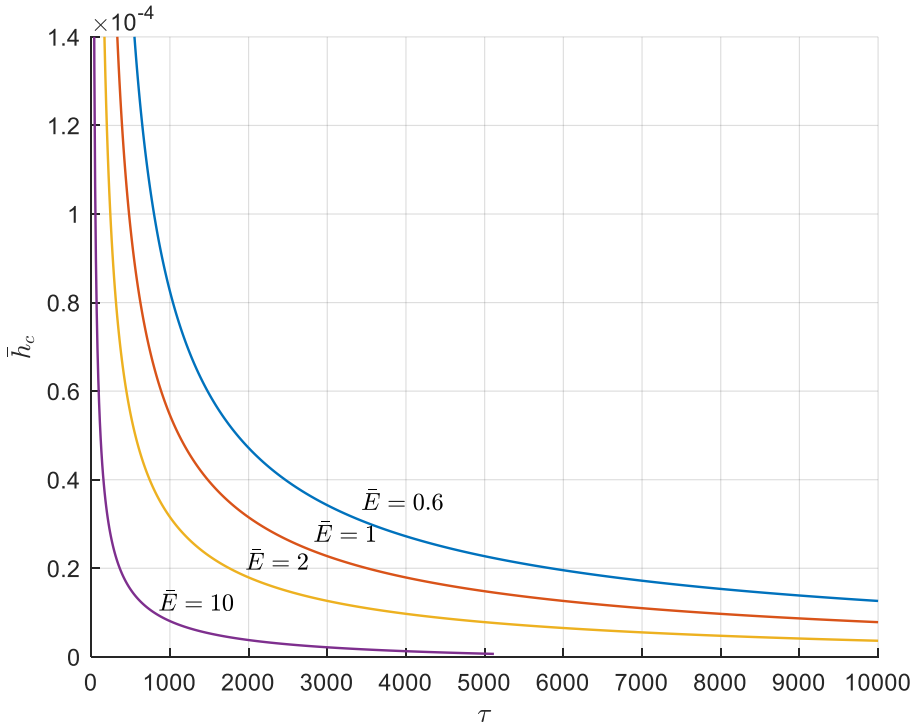

Figure 7.19 Elastic modulus Sweep 3: $\bar{h}_0 = 10, \bar{\alpha} = 1, \bar{b} = 0.1$; Central film thickness time histories

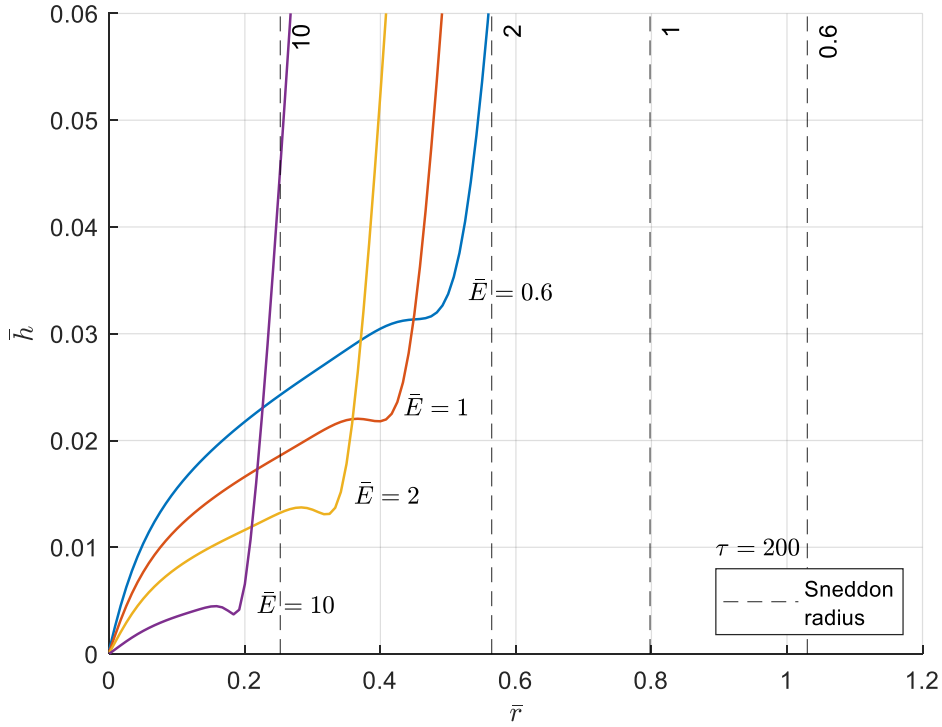

Figure 7.20 Elastic modulus Sweep 3: $\bar{h}_0 = 10, \bar{\alpha} = 1, \bar{b} = 0.1$; Film thickness profiles, $\tau = 200$

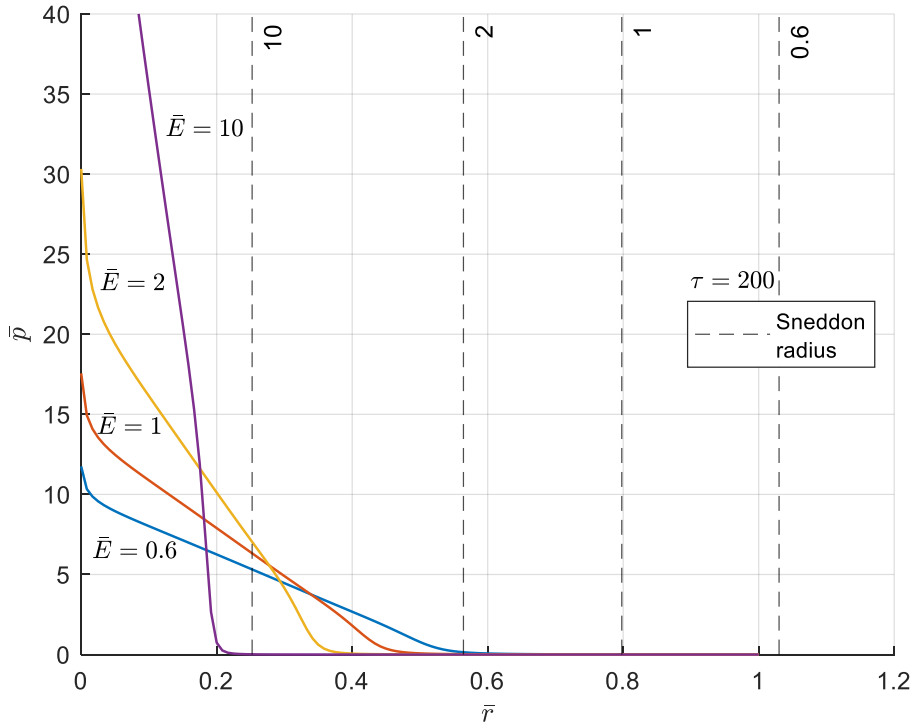

Figure 7.21 Elastic modulus Sweep 3: $\bar{h}_0 = 10, \bar{\alpha} = 1, \bar{b} = 0.1$; Film pressure profiles, $\tau = 200$

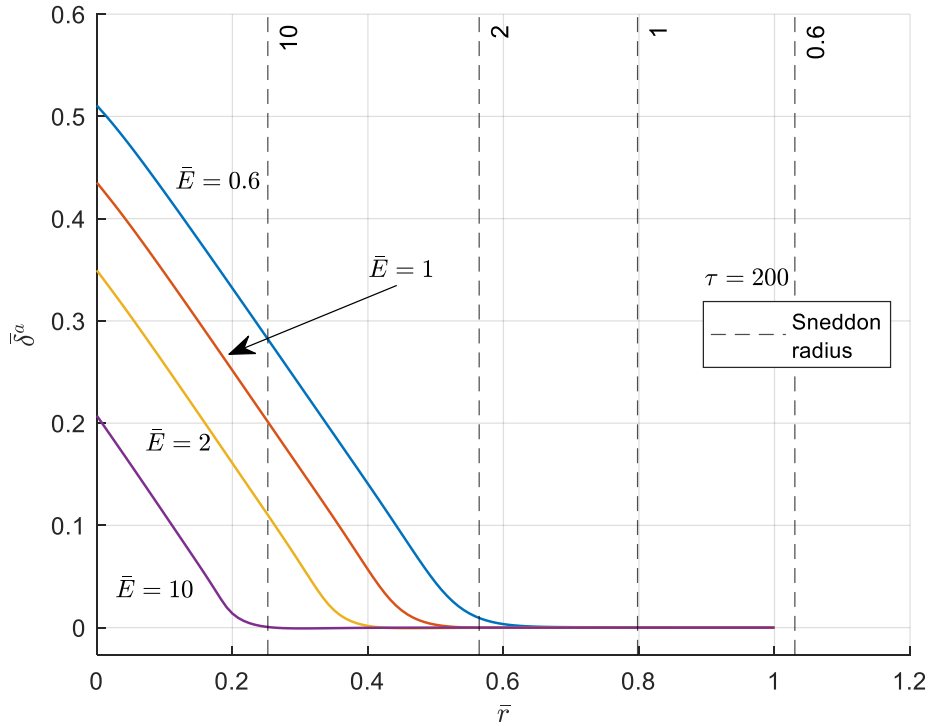

Figure 7.22 Elastic modulus Sweep 3: $\bar{h}_0 = 10, \bar{\alpha} = 1, \bar{b} = 0.1$; Elastic layer surface deflection profiles, $\tau = 200$

Chapter 8
Conclusions

This thesis has presented an efficient numerical scheme for studying the behavior of transient, axisymmetric, elastohydrodynamic squeeze-films between a rigid indenter and a thin elastic layer. This approach was used to provide the first comparison between theoretical EHL results and the complete experimental data set presented by Gaman et al. [5]. This comparison showed good agreement between the experimental data and theoretical results, providing validation of the current approach. The current approach was also compared with the results given by Booker and Boedo [8] to examine the validity of modeling a thin elastic layer as an elastic halfspace.

This thesis also provided full nondimensional formulations for bearings with indenters with either a paraboloid or conical profile. Parameter sweeps were given showing design trends. It was found that bearings with an elastic layer show little to no dependence on the initial clearence between the indenter and elastic layer. This is stark contrast to the behvior of squeeze-film bearings with fully rigid surfaces, which depend strongly on the initial clearence. Since the current approach also depends explicitly on the load rate, the effects of a a tunable load rate parameter were examined. When the load rate was increased enough that the rise time of the load was significantly shorter than the natural transient behavior of the system, further increases had no effect on the results.

The stiffness and thickness of the thin elastic layer were found to have a large impact on the system behavior. For extremely low stiffnesses, the pressure distribution flattened and the elastic layer pinched the edge of the indenter, reminiscent of a flat-ended indenter under dry contact (the Boussinesq problem). For more moderate stiffness values and large layer thicknesses, a ridge of material formed around a central pocket of lubricant. This allowed for a long settling time as the lubricant was slowly squeezed out through this constriction. However, at high stiffness values, the elastic deflections and the size of the ridge were greatly diminished which resulted in smaller film thicknesses and reduced settling times. Small layer thickness ratios served to affect the results similarly to increasing the stiffness by decreasing the apparent “contact radius” and film thicknesses.

The current Nodal Inverse Hydrodynamic approach provides great computational efficiency compared with other numerical methods since instantaneous film properties at each time step can be directly calculated. This is in contrast to the widely used Newton-Raphson method which requires iteration at each time step. This approach also offers advantages over analytical methods, such as work by Jaffar using Grubin's approximation [12]. Since no assumptions are made about the deformation profile, the development of a ridge in the elastic layer is predicted, which matches experimental evidence. The current approach also allows for analysis of effects not amenable to analytical solutions such as arbitrary indenter geometries or arbitrarily located lubricant feed holes or pressure taps.

This thesis examined the squeeze-film under several assumptions that could be relaxed for future investigations. Instead of the current isothermal and isoviscous lubricant, appropriate models of themal and piezoviscous effects could be included to examine the effects of higher pressures. The current thin elastic layer on a frictionless support could also be replaced by a thin layer bonded to its support, still modeled by exact linear elasticity. The linearly elastic model of the thin, soft layer could be replaced by a finite deformation model to examine the effects of large deflections in the thin layer or viscoelastic effects. The non-reversing step load could also be replaced with an arbitrarily varying load (e.g. sinusoidal). This would necessitate incorporating the effects of cavitation in cases where the film thickness increases due to normal separation of the surfaces.

With a minor modification of boundary conditions, the current approach can also be compared with experimental data for a hydrostatic thrust bearing with a soft thin layer fed by a pressurized central feed hole given by Castelli, Rightmire, Fuller [14], Dowson, Jones [27], and Dowson, Taylor [23]. Such a comparison would provide further experimental validation.

This thesis provides the theoretical background for the numerical approach used so that other analysts can develop simulations for similar squeeze-film problems with compliance layers. It also provides design charts useful for lookup of design parameters to determine system parameters to achive system behavior deisred by a bearing designer.

Appendix A

Surface Deflection of a Slab due to a Uniform Pressure Distribution

Conway [16] provides a semi-analytical method for computing the compliance matrix of a thin axisymmetric slab with infinite radius. The surface displacement of a point at radius r, due to a constant pressure distribution p_0 of radius c, as shown in Figure A-1, is given by

$$\bar{w} = \frac{4(1-\nu^2)p_0 c}{E}\int_0^\infty \frac{\sinh^2(\alpha b)J_0(\alpha r)J_1(\alpha c)}{2(\alpha b)^2 + \alpha b\,\sinh^2(2\alpha b)}\,\mathrm{d}(\alpha b)$$

Introducing three dimensionless parameters $\xi = \alpha b$, $r = \bar{r}b$, $c = \bar{c}b$, yields

$$\bar{w} = \frac{4(1-\nu^2)p_0 c}{E}\int_0^\infty \frac{\sinh^2(\xi)J_0(\bar{r}\xi)J_1(\bar{c}\xi)}{2\xi^2 + \xi\sinh^2(2\xi)}\,\mathrm{d}\xi = \frac{4(1-\nu^2)p_0 c}{E}\,\mathrm{I}(\bar{r},\bar{c})$$

The integral I is exceedingly difficult to evaluate numerically, so an approximation is required. Following Conway, for "large" values of ξ

$$\frac{\sinh^2\xi}{2\xi^2 + \xi\sinh(2\xi)} \approx \frac{1}{2\xi}$$

The absolute error of this approximation to the original expression is on the order of 10^{-8} and 10^{-17} for $\xi = 10$ and $\xi = 20$, respectively. Using this approximation, I is given by

$$\mathrm{I}(\bar{r},\bar{c}) = \int_0^\infty \frac{\sinh^2(\xi)J_0(\bar{r}\xi)J_1(\bar{c}\xi)}{2\xi^2 + \xi\sinh^2(2\xi)}\,\mathrm{d}\xi$$

$$= \int_0^{\mathrm{A}} \frac{\sinh^2(\xi)J_0(\bar{r}\xi)J_1(\bar{c}\xi)}{2\xi^2 + \xi\sinh^2(2\xi)}\,\mathrm{d}\xi + \int_A^\infty \frac{\sinh^2(\xi)J_0(\bar{r}\xi)J_1(\bar{c}\xi)}{2\xi^2 + \xi\sinh^2(2\xi)}\,\mathrm{d}\xi$$

$$\approx \int_0^{\mathrm{A}} \frac{\sinh^2(\xi)J_0(\bar{r}\xi)J_1(\bar{c}\xi)}{2\xi^2 + \xi\sinh^2(2\xi)}\,\mathrm{d}\xi + \int_A^\infty \frac{J_0(\bar{r}\xi)J_1(\bar{c}\xi)}{2\xi}\,\mathrm{d}\xi$$

$$= \int_0^{\mathrm{A}} \left(\frac{\sinh^2(\xi)}{2\xi^2 + \xi\sinh^2(2\xi)} - \frac{1}{2\xi}\right)J_0(\bar{r}\xi)J_1(\bar{c}\xi)\,\mathrm{d}\xi + \int_0^\infty \frac{J_0(\bar{r}\xi)J_1(\bar{c}\xi)}{2\xi}\,\mathrm{d}\xi$$

$$= \int_0^{\mathrm{A}} \left(\frac{\sinh^2(\xi)}{2\xi^2 + \xi\sinh^2(2\xi)} - \frac{1}{2\xi}\right)J_0(\bar{r}\xi)J_1(\bar{c}\xi)\,\mathrm{d}\xi + \begin{cases} \dfrac{1}{\pi}E\left(\dfrac{\bar{r}}{\bar{c}}\right) & 0 < \bar{r} < \bar{c} \\ \dfrac{\bar{r}}{\pi\bar{c}}E\left(\dfrac{\bar{c}}{\bar{r}}\right) + \dfrac{1}{\pi}\left(\dfrac{\bar{c}}{\bar{r}} - \dfrac{\bar{r}}{\bar{c}}\right)K\left(\dfrac{\bar{c}}{\bar{r}}\right) & 0 < \bar{c} < \bar{r} \\ \dfrac{1}{\pi} & \bar{c} = \bar{r} \end{cases}$$

where $\mathrm{K(k)} = \int_0^{\frac{\pi}{2}} (1 - \mathrm{k}^2 \sin^2 \theta)^{\frac{-1}{2}} \, \mathrm{d}\theta$ and $\mathrm{E(k)} = \int_0^{\frac{\pi}{2}} (1 - k^2 \sin^2 \theta)^{\frac{1}{2}} \mathrm{d}\theta$ are the complete elliptic integrals of the first and second kind, respectively. The integration limit A is a constant chosen such that the integral in the first term converges without succumbing to numerical loss of precision ($A = 25$ was found to be suitable).

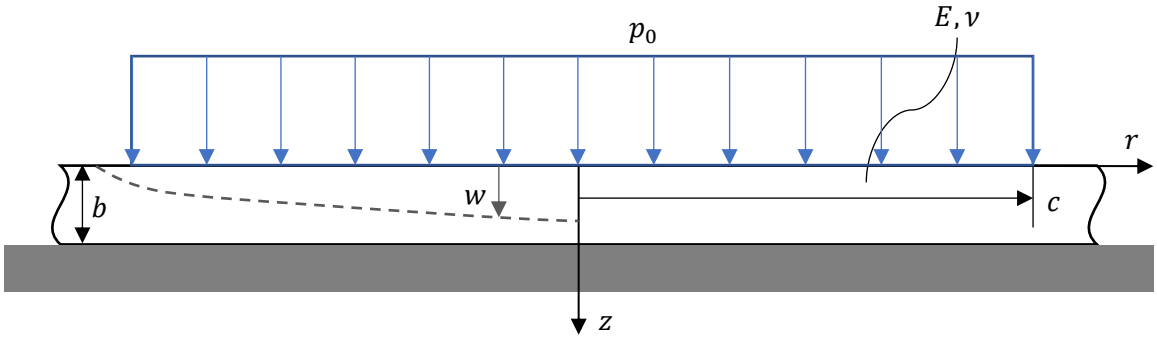

Figure A-1 Infinite, thin elastic layer loaded with an uniform pressure over a circular region

Appendix B

Surface Deflection of a Slab due to a Triangular Pressure Distribution

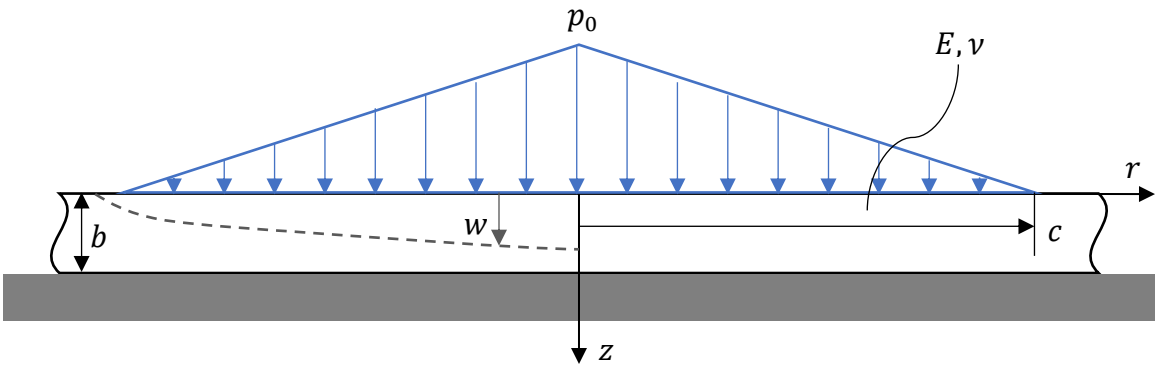

Figure B-1 Triangular, axisymmetric pressure distribution

Based on Conway [16],

$$\mathrm{w} = \frac{4(1-\nu^2)}{E}\int_0^\infty \frac{\sinh^2(\alpha b)}{2(\alpha b)^2 + \alpha b \sinh(\alpha b)}\,\psi(\alpha)\,J_0(\alpha r)\,\alpha\,d\alpha$$

where $\psi(\alpha)$ is the transformed pressure distribution given by

$$\psi(\alpha) = \int_0^\infty p(r)\,J_0(\alpha r)\,r\,dr$$

For the triangular pressure distribution shown in Figure B-1,

$$\mathrm{p}(r) = \begin{cases} p_0\left(1-\dfrac{r}{c}\right) & r \le c \\ 0 & r > c \end{cases}$$

and the transformed pressure distribution is given by [28]

$$\psi(\alpha) = \frac{\pi\,p_0}{2\,\alpha^2}[J_1(\alpha c)H_0(\alpha c) - J_0(\alpha c)H_1(\alpha c)]$$

where

J_0 and J_1 are Bessel functions of the first kind, order zero and one, respectively.

H_0 and H_1 are Struve functions, order zero and one, respectively

The surface displacement can then be written

$$\mathrm{w} = \frac{4(1-\nu^2)}{E}\int_0^\infty \frac{\sinh^2(\alpha b)}{2(\alpha b)^2 + \alpha b \sinh(\alpha b)}\frac{\pi\,p_0}{2\,\alpha^2}[J_1(\alpha c)H_0(\alpha c) - J_0(\alpha c)H_1(\alpha c)]\,J_0(\alpha r)\,\alpha \mathrm{d}\alpha$$

$$= \frac{2\pi(1-\nu^2)p_0}{E}\int_0^\infty \frac{\sinh^2(\alpha b)}{2(\alpha b)^2 + \alpha b\sinh(\alpha b)}\left[J_1(\alpha c)H_0(\alpha c) - J_0(\alpha c)H_1(\alpha c)\right]J_0(\alpha r)\frac{\mathrm{d}\alpha}{\alpha}$$

$$= \frac{2\pi(1-\nu^2)p_0 b}{E}\int_0^\infty \frac{\sinh^2\xi}{2\xi^3 + \xi^2\sinh\xi}\left[J_1(\bar{c}\xi)H_0(\bar{c}\xi) - J_0(\bar{c}\xi)H_1(\bar{c}\xi)\right]J_0(\bar{r}\xi)\,\mathrm{d}\xi$$

where $\xi = \alpha b$, $r = \bar{r}\,b$, $c = \bar{c}\,b$

For brevity, introduce

$$\bar{\psi}(\xi;\bar{c}) = J_1(\bar{c}\xi)H_0(\bar{c}\xi) - J_0(\bar{c}\xi)H_1(\bar{c}\xi)$$

and define the dimensionless integral

$$J(\bar{r},\bar{c}) = \int_0^\infty \frac{\sinh^2\xi}{2\xi^3 + \xi^2\sinh\xi}\left[J_1(\bar{c}\xi)H_0(\bar{c}\xi) - J_0(\bar{c}\xi)H_1(\bar{c}\xi)\right]J_0(\bar{r}\xi)\,d\xi$$

$$= \int_0^\infty \frac{\sinh^2\xi}{2\xi^3 + \xi^2\sinh\xi}\bar{\psi}(\xi;\bar{c})J_0(\bar{r}\xi)\,d\xi$$

This integral is problematic to numerically integrate, similar to those found in [16]. To evaluate this integral, the same approximation can be employed. For "large" values of ξ:

$$\frac{\sinh^2\xi}{2\xi^3 + \xi^2\sinh\xi} \approx \frac{1}{2\xi^2}$$

Using this approximation, the integral can be split into two regions at a suitable point A. Both of these integrals can then be evaluated numerically. Unfortunately, there appears to be no convenient simplification for the latter integral similar to those in [16], so numerical integration is required.

$$J(\bar{r},\bar{c}) \approx \int_0^A \frac{\sinh^2\xi}{2\xi^3 + \xi^2\sinh\xi}\bar{\psi}(\xi;\bar{c})J_0(\bar{r}\xi)\,d\xi + \int_A^\infty \frac{1}{2\xi^2}\bar{\psi}(\xi;\bar{c})J_0(\bar{r}\xi)\,d\xi$$

Finally, the surface deflection can be written as

$$\bar{w} = \frac{2\pi(1-\nu^2)p_0 b}{E}J(\bar{r},\bar{c})$$

Note: MATLAB has no built-in function for evaluating Struve functions. Various polynomial approximations and algorithms are available [29]. There are also implementations uploaded to the MathWorks community file exchange [30].

Appendix C

C^0 Continuous Thin Slab Compliance

The entries in the compliance matrix generated using formulas from Conway [16] can be efficiently computed thanks to convenient solutions for some of the integral expressions that are produced. However, it relies on an approximation of the pressure distribution that is discontinuous. And while that approximation is amenable for convenient numerical evaluation, it is unreflective of realistic, physical pressure distributions.

Using a similar methodology, a compliance matrix can be derived that relies instead on a piecewise-linear pressure distribution. This representation can be formulated such that it has C^0 continuity (i.e. no discontinuous jumps in pressure). This provides a more realistic, although still approximate, distribution of pressure. Unfortunately, the formulas obtained from this process do not appear to have any convenient solutions analogous to those for the stepwise pressure distribution. This necessitates the numerical integration of an infinite, oscillatory integral, which is highly computationally expensive. The difference in computation time between these methods is substantial, at a factor of 1300:1.

Despite the high computational cost, it is worthwhile to compare the results of two otherwise identical simulations run with the Conway thin slab compliance matrix and this C^0 continuous compliance matrix. If there is negligible difference between the results, then further simulations can be carried out with confidence using the more efficient Conway formulation, rather than the more accurate but costly C^0 continuous formulation. Figures C-1 and C-2 show surface pressure distributions underneath a flat-ended indenter for a range of layer thicknesses for the discontinuous Conway compliance matrix and C^0 compliance matrix, respectively. These curves show essentially no difference between the two calculation methods, apart for differences in the oscillatory behavior near the indenter edge where a singularity occurs. This provides confidence that the computationally efficient Conway compliance matrix is suitable for numerical simulations despite its more approximate pressure distribution.

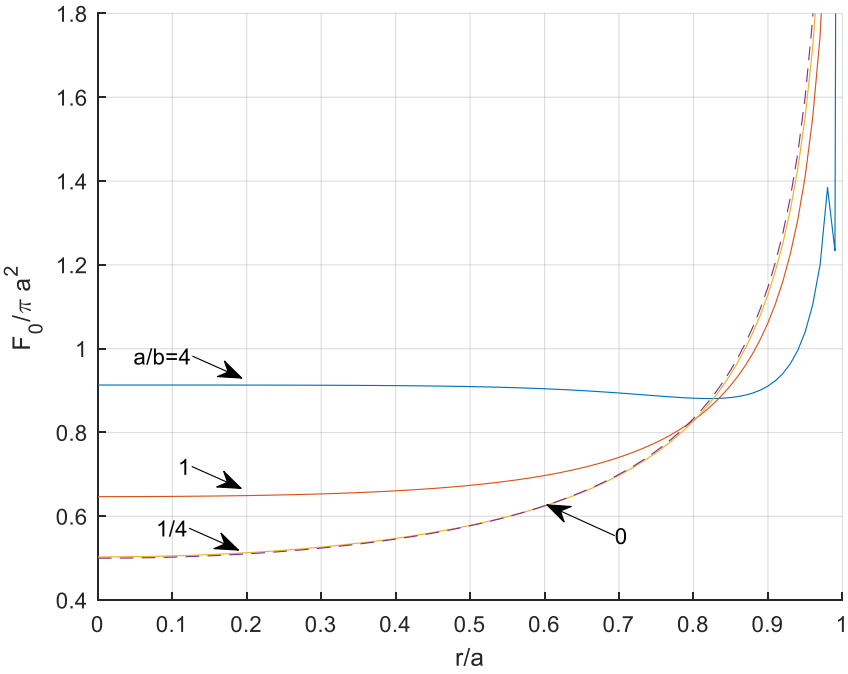

Figure C-1 Normal stress distribution under axially loaded, flat-ended, frictionless indenter using Conway compliance matrix

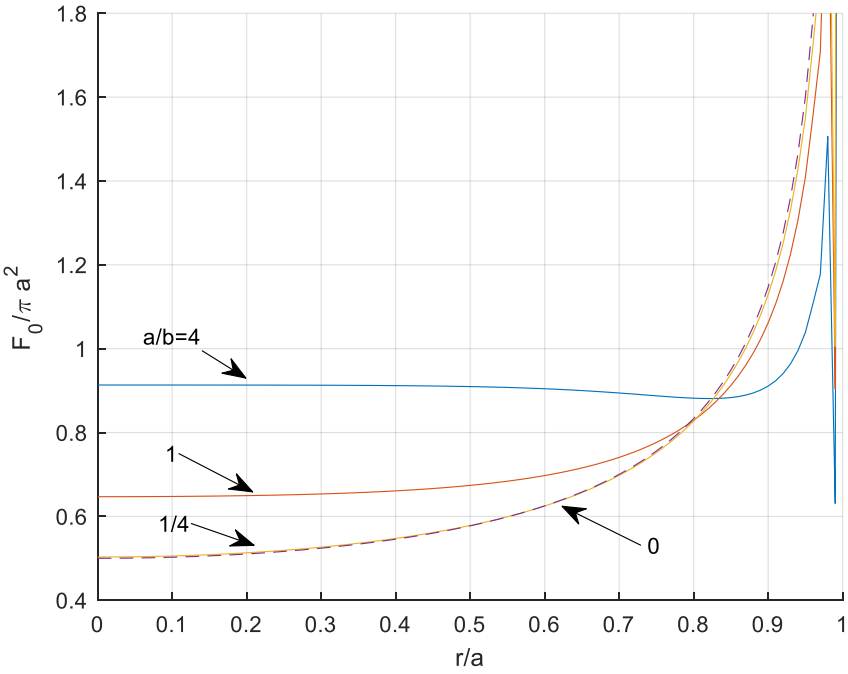

Figure C-2 Normal stress distribution under axially loaded, flat-ended, frictionless indenter using C^0 compliance matrix

The C^0 continuous compliance matrix is based on a tent function of a typical linear 1D finite element. This tent function can be broken up into a downward sloping portion and an upward sloping portion. Each of these pieces is more convenient to analyze separately.

C.1 Downward Slope Triangular Annulus

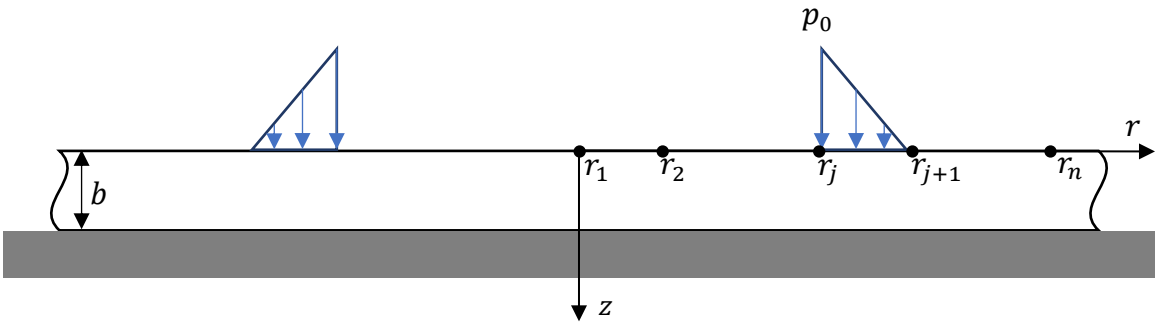

Figure C-3 Infinite, thin elastic layer loaded with an annulus of pressure with a triangular cross-section, with a negative slope

The downward sloping portion of the tent function pressure distribution shown in Figure C-3 can be represented as the superposition of three simpler pressure distributions: two triangular and one uniform.

1) The first triangular distribution acts downward on the surface. It has a slope of $\frac{-p_0}{r_{j+1}-r_j}$, and has an extent of r_{j+1}. Hence, its pressure distribution is given by

$$p_1(r) = \frac{p_0}{r_{j+1}-r_j}\left(r_{j+1}-r\right) = \frac{p_0}{1-\frac{r_j}{r_{j+1}}}\left(1-\frac{r}{r_{j+1}}\right) \quad 0 \le r \le r_{j+1}$$

2) The second triangular pressure distribution acts upward on the surface (i.e. a negative pressure). It also has a slope of $\frac{p_0}{r_{j+1}-r_j}$, but only extends to r_j:

$$p_2(r) = -\frac{p_0}{r_{j+1}-r_j}\left(r_j-r\right) = \frac{p_0}{1-\frac{r_{j+1}}{r_j}}\left(1-\frac{r}{r_j}\right) \quad 0 \le r \le r_j$$

3) The uniform pressure distribution also acts upward on the surface with a magnitude of p_0 and an extent of r_j.

$$p_3(r) = -p_0 \quad 0 \le r \le r_j$$

Since slab is linearly elastic, the total surface deflection is the superposition of these three cases. The surface deflection due to a uniform pressure distribution is given in Appendix A.

The surface deflection due to a triangular distribution is derived in Appendix B. The total surface deflection is then given by

$$\mathrm{w} = \frac{2\pi(1-\nu^2)b}{E}\frac{p_0}{1-\frac{r_j}{r_{j+1}}}\mathrm{J}\left(\bar{r}=\frac{r}{b},\bar{c}=\frac{r_{j+1}}{b}\right)$$

$$+\frac{2\pi(1-\nu^2)b}{E}\frac{p_0}{1-\frac{r_{j+1}}{r_j}}J\left(\bar{r}=\frac{r}{b},\bar{c}=\frac{r_j}{b}\right)$$

$$+\frac{4(1-\nu^2)r_j}{E}(-p_0)I\left(\bar{r}=\frac{r}{b},\bar{c}=\frac{r_j}{b}\right)$$

Using this formula, a compliance matrix can be constructed to represent the deflection at each node i on the surface due to a unit pressure at each node j. This "downward sloping compliance matrix" has entries given by

$$C_{ij}^{(d)} = \frac{2\pi(1-\nu^2)b}{E}\left[\frac{1}{1-\frac{r_j}{r_{j+1}}}J\left(\bar{r}=\frac{r_i}{b},\bar{c}=\frac{r_{j+1}}{b}\right)+\frac{1}{1-\frac{r_{j+1}}{r_j}}J\left(\bar{r}=\frac{r_i}{b},\bar{c}=\frac{r_j}{b}\right)\right.$$

$$\left.-\frac{2r_j}{\pi b}I\left(\bar{r}=\frac{r_i}{b},\bar{c}=\frac{r_j}{b}\right)\right]$$

$$C_{i1}^{(d)} = \frac{2\pi(1-\nu^2)b}{E}\mathrm{J}\left(\bar{r}=\frac{r_i}{b},\bar{c}=\frac{r_2}{b}\right)$$

$$C_{in}^{(d)} = 0$$

C.2 Upward Slope Triangular Annulus

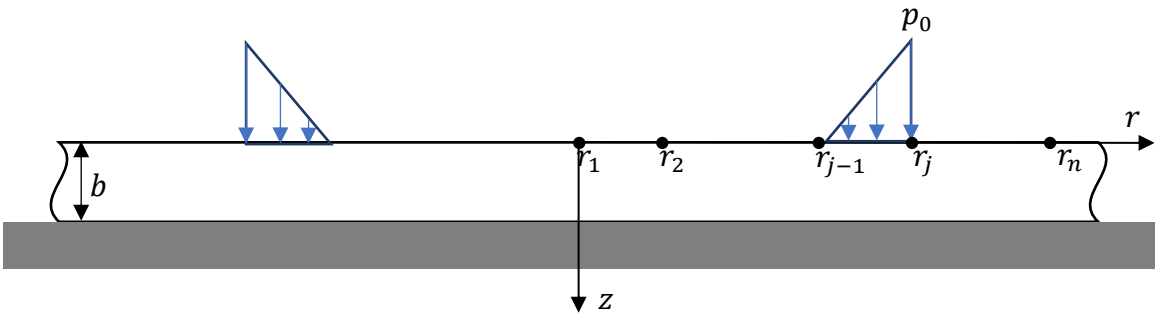

Figure C-4 Infinite, thin elastic layer loaded with an annulus of pressure with a triangular cross-section, with a positive slope

The upward sloping portion of a tent function pressure distribution shown in Figure C-4 can also be represented a superposition of three simpler pressure distributions, again one uniform and two triangular.

$$p_1(r) = p_0 \quad 0 \le r \le r_j$$

$$p_2(r) = -\frac{p_0}{r_j - r_{j-1}}\left(r_j - r\right) = \frac{p_0}{\frac{r_{j-1}}{r_j} - 1}\left(1 - \frac{r}{r_j}\right) \quad 0 \le r \le r_j$$

$$p_3(r) = -\frac{p_0}{r_j - r_{j-1}}\left(r_{j-1} - r\right) = \frac{p_0}{\frac{r_j}{r_{j-1}} - 1}\left(1 - \frac{r}{r_{j-1}}\right) \quad 0 \le r \le r_{j-1}$$

which yield a total surface deflection:

$$\mathrm{w} = \frac{4(1-\nu^2)r_j}{E}\ p_0\, I\left(\bar{r} = \frac{r}{b}, \bar{c} = \frac{r_j}{b}\right) + \frac{2\pi(1-\nu^2)b}{E}\frac{p_0}{\frac{r_{j-1}}{r_j} - 1} J\left(\bar{r} = \frac{r}{b}, \bar{c} = \frac{r_j}{b}\right) + \frac{2\pi(1-\nu^2)b}{E}\frac{p_0}{\frac{r_j}{r_{j-1}} - 1} J\left(\bar{r} = \frac{r}{b}, \bar{c} = \frac{r_{j+1}}{b}\right)$$

Using this formula, a compliance matrix can be constructed to represent the deflection at each node i on the surface due to a unit pressure at each node j. This "upward sloping compliance matrix" has entries given by

$$C_{i1}^{(u)} = 0$$

$$C_{i2}^{(u)} = \frac{2\pi(1-\nu^2)b}{E}\left[\frac{2r_j}{\pi b}\ I\left(\bar{r} = \frac{r_i}{b}, \bar{c} = \frac{r_2}{b}\right) - J\left(\bar{r} = \frac{r_i}{b}, \bar{c} = \frac{r_2}{b}\right)\right]$$

$$C_{ij}^{(u)} = \frac{2\pi(1-\nu^2)b}{E}\left[\frac{2r_j}{\pi b}\ I\left(\bar{r} = \frac{r_i}{b}, \bar{c} = \frac{r_j}{b}\right) + \frac{1}{\frac{r_{j-1}}{r_j} - 1} J\left(\bar{r} = \frac{r_i}{b}, \bar{c} = \frac{r_j}{b}\right) + \frac{1}{\frac{r_j}{r_{j-1}} - 1} J\left(\bar{r} = \frac{r_i}{b}, \bar{c} = \frac{r_{j-1}}{b}\right)\right]$$

C.3 Compliance Matrix

The total compliance of the thin slab is given by the sum of $C^{(d)}$ and $C^{(u)}$.

$$C_{i1} = \frac{2\pi(1-\nu^2)b}{E}\mathrm{J}(\bar{r}_i, \bar{c}_2)$$

$$C_{i2} = \frac{2\pi(1-\nu^2)b}{E}\left[\frac{1}{1-\varphi_2}\mathrm{J}(\bar{r}_i, \bar{c}_3) + \left(\frac{\varphi_2}{\varphi_2 - 1} - 1\right)\mathrm{J}(\bar{r}_i, \bar{c}_2)\right]$$

$$C_{ij} = \frac{2\pi(1-\nu^2)b}{E}\left[\frac{1}{1-\varphi_j}J(\bar{r}_i, \bar{c}_{j+1}) + \left(\frac{\varphi_j}{\varphi_j - 1} - \frac{1}{\varphi_{j-1} - 1}\right)\mathrm{J}(\bar{r}_i, \bar{c}_j) + \frac{\varphi_{j-1}}{1-\varphi_{j-1}}\mathrm{J}(\bar{r}_i, \bar{c}_{j-1})\right]$$

$$C_{in} = \frac{2\pi(1-\nu^2)b}{E}\left[\frac{2r_n}{\pi b}\, I(\bar{r}_i, \bar{c}_n) + \frac{1}{1-\varphi_{n-1}}J(\bar{r}_i, \bar{c}_n) + \frac{\varphi_{n-1}}{1-\varphi_{n-1}}\mathrm{J}(\bar{r}_i, \bar{c}_{n-1})\right]$$

Where

$$\bar{r}_i = \frac{r_i}{b} \qquad \bar{c}_j = \frac{r_j}{b} \qquad \varphi_k = \frac{r_k}{r_{k+1}}$$

Since this nodal pressure distribution is identical to a linear shape function for a finite element, it guarantees C^0 continuity of the entire pressure distribution. This is more realistic than the uniform pressure steps used in [16]. This also does not require creating a separate series of radii c_j for the pressure distribution extent, as is necessary for the uniform pressure distributions.

Appendix D

Surface Normal Approximation

In the current formulation, the curvature of the elastic surface is assumed to be negligible. This assumption justifies treating the direction cosine in the z-direction of the surface normal at every point as equal to unity. This assumption can be justified *a posteriori* by calculating the resultant direction cosines of the deformed surface and examining their error from unity. Figure D-1 shows the error from unity for the surface normal of every node in the finite element discretization of the elastic surface at several timesteps. These errors are on the order of 0.1%, or one part per 1000, which is negligible.

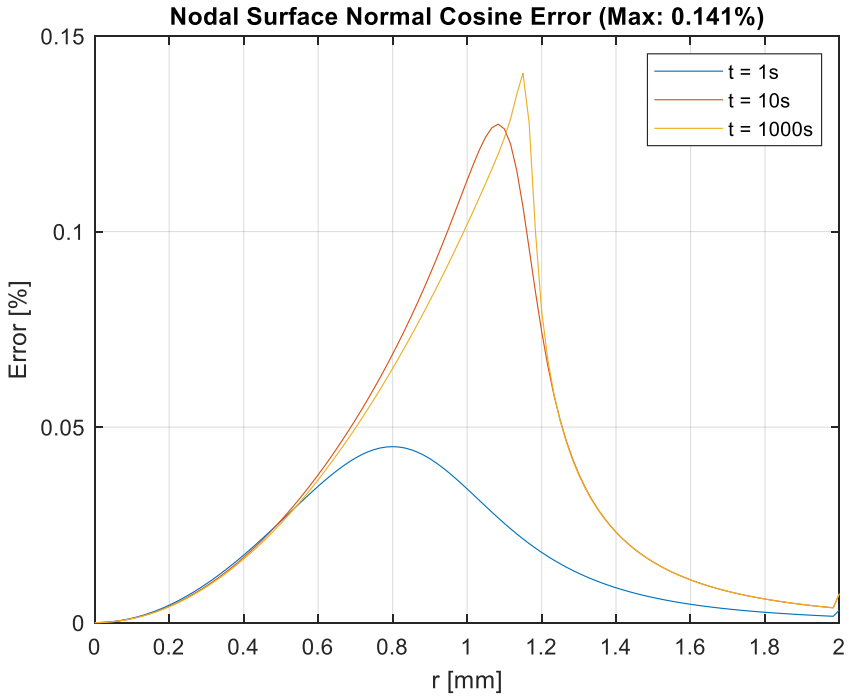

Figure D-1 Surface normal cosine error at selected timesteps for a 6mm elastic layer load with 0.13N

References

[1] Boedo, S., 2015, “Transient Dynamics of the Conformal Elastohydrodynamic Squeeze Film Problem,” J. Tribol., **137**(4), p. 041506.

[2] Fein, R. S., 1966, “Research Report 3: Are Synovial Joints Squeeze-Film Lubricated?,” Proc. Inst. Mech. Eng. Conf. Proc., **181**(10), pp. 125–128.

[3] Norman, R., 1971, “The Lubrication of Porous Elastic Solids, With Reference To the Functioning of Animal Joints.,” Durham University.

[4] Higginson, G. R., and Norman, R., 1974, “A Model Investigation of Squeeze-Film Lubrication in Animal Joints,” Phys. Med. Biol., **19**(6), pp. 785–792.

[5] Gaman, I. D. C., Higginson, G. R., and Norman, R., 1974, “Fluid Entrapment by a Soft Surface Layer,” Wear, **28**(3), pp. 345–352.

[6] Mattei, L., Di Puccio, F., Piccigallo, B., and Ciulli, E., 2011, “Lubrication and Wear Modelling of Artificial Hip Joints: A Review,” Tribol. Int., **44**(5), pp. 532–549.

[7] Buckholz, R. H., 1984, “On the Role of a Compliant Surface in Long Squeeze Film Bearings,” J. Appl. Mech., **51**(4), pp. 885–891.

[8] Booker, J. F., and Boedo, S., 2018, “Nodal Unsteady Inverse Elastohydrodynamic Lubrication: Axisymmetric Normal Approach,” J. Tribol., **140**(4), p. 041501.

[9] Booker, J. F., and Huebner, K. H., 1972, “Application of Finite Element Methods to Lubrication: An Engineering Approach,” J. Tribol., **94**(4), pp. 313–323.

[10] Booker, J. F., and Shu, C. F., 1984, “Finite Element Analysis of Transient Elastohydrodynamic Lubrication,” *Developments in Numerical and Experimental Methods Applied to Tribology*, Elsevier, pp. 157–163.

[11] Chen, Q.-D., and Li, W.-L., 2018, “Analysis of Soft-Elastohydrodynamic Lubrication Line Contacts on Finite Thickness,” J. Tribol., **140**(4), p. 041502.

[12] Jaffar, M. J., 2006, “Prediction of the Film Thickness for the Normal Approach of a Rigid Sphere towards a Thin Soft Layer,” Tribol. Lett., **22**(3), pp. 247–251.

[13] Jaffar, M. J., 2008, “On the Frictionless Axi-Symmetric Contact of a Thick Elastic Layer and the Associated Squeeze Film Problem,” J. Eng. Tribol., **222**(1), pp. 61–68.

[14] Castelli, V., Rightmire, G. K., and Fuller, D. D., 1967, “On the Analytical and Experimental Investigation of a Hydrostatic, Axisymmetric Compliant-Surface Thrust Bearing,” J. Lubr. Technol., **89**(4), pp. 510–519.

[15] Booker, J. F., 2005, “Unsteady EHL: An Inverse Hydrodynamic Formulation,” *Tribology and Interface Engineering Series*, pp. 65–74.

[16] Conway, H. D., Vogel, S. M., Farnham, K. A., and So, S., 1966, “Normal and Shearing Contact Stresses in Indented Strips and Slabs,” Int. J. Eng. Sci., **4**(4), pp. 343–359.

[17] Grubin, A. N., 1949, “Fundamentals of the Hydrodynamic Theory of Lubrication of Heavily Loaded Cylindrical Surfaces,” Investig. Contact Mach. Componets, **2**, pp. 115–166.

[18] Johnson, K. L., 1985, *Contact Mechanics*, Cambridge University Press.

[19] Sneddon, I. N., 1948, “Boussinesq’s Problem for a Rigid Cone,” Math. Proc. Cambridge Philos. Soc., **44**(4), pp. 492–507.

[20] Sneddon, I. N., 1965, “The Relation between Load and Penetration in the Axisymmetric Boussinesq Problem for a Punch of Arbitrary Profile,” Int. J. Eng. Sci., **3**(1), pp. 47–57.

[21] Boedo, S., and Booker, J. F., 2004, “Classical Bearing Misalignment and Edge Loading: A Numerical Study of Limiting Cases,” J. Tribol., **126**(3), pp. 535–541.

[22] Shampine, L. F., and Reichelt, M. W., 1997, “The MATLAB ODE Suite,” SIAM J. Sci. Comput., **18**(1), pp. 1–22.

[23] Dowson, D., and Taylor, C. M., 1967, “Elastohydrostatic Lubrication of Circular Plate Thrust Bearings,” J. Lubr. Technol., **89**(3), pp. 237–242.

[24] Castelli, V., and Rightmire, G. K., 1967, “Discussion: ‘Elastohydrostatic Lubrication of Circular Plate Thrust Bearings’ (Dowson, D., and Taylor, C. M., 1967, ASME J. Lubr. Technol., 89, Pp. 237–242),” J. Lubr. Technol., **89**(3), pp. 242–244.

[25] Booker, J. F., and Boedo, S., 2018, “Closure to ‘Discussion of “Nodal Unsteady Inverse Elastohydrodynamic Lubrication: Axisymmetric Normal Approach”’ (Booker, J. F., and Boedo, S., 2018, ASME J. Tribol., 140(4), p. 041501),” J. Tribol., **140**(6), p. 066001.

[26] Bair, S., and Habchi, W., 2021, “Your EHD Rig May Not Be As Elastohydrodynamic As You Think,” J. Tribol., **143**(8), p. 081601.

[27] Dowson, D., and Jones, D. A., 1967, “Lubricant Entrapment between Approaching Elastic Solids,” Nature, **214**(5091), pp. 947–948.

[28] Rosenheinrich, W., and Jena, E. A. H., 2019, “Tables of Some Indefinite Integral of Bessel Functions of Integer Order,” Ernst-Abbe-Hochschule Jena, Univ. Appl. Sci. Dep. basic Sci. Ger. (disponible en ligne)(version 05.11. 2017).

[29] Newman, J. N., 1984, “Approximations for the Bessel and Struve Functions,” Math. Comput., **43**(168), pp. 551–556.

[30] Theodoulidis, T. P., 2012, *Struve Functions*, 1.4.0.0, Theo2 (2022). Struve functions (https://www.mathworks.com/matlabcentral/fileexchange/37302-struve-functions), MATLAB Central File Exchange. Retrieved August 4, 2022.